THESIS FOR THE DEGREE OF DOCTOR OF PHILOSOPHY

# Evolution of microstructure and nanoscale chemistry of Zircaloy-2-type alloys during nuclear reactor operation

JOHAN ERIKSSON

Department of Physics

CHALMERS UNIVERSITY OF TECHNOLOGY

Gothenburg, Sweden 2022

Evolution of microstructure and nanoscale chemistry of
Zircaloy-2-type alloys during nuclear reactor operation
JOHAN ERIKSSON
ISBN 978-91-7905-734-3



Doktorsavhandlingar vid Chalmers tekniska högskola
Ny serie nr 5200
ISSN 0346-718X

Department of Physics
Chalmers University of Technology
SE-412 96 Gothenburg
Sweden
Telephone + 46 (0)31-772 1000

Cover:
Left/lower centre: atom probe tomography (APT) reconstruction of a γ-hydride and an α-Zr specimen, corresponding hitmaps, and schematic atomic arrangements in the two structures.
Upper centre: APT reconstruction of a disc-shaped Fe–Ni cluster viewed in two directions with a relative rotation of 90°.
Upper right: APT reconstruction of a layer of Fe–Cr and Fe–Ni clusters viewed in the approximate ⟨c⟩-direction.
Lower right: APT reconstruction of a region with Sn clusters and a presumed ⟨c⟩-component loop.
All reconstructions are from Zircaloy-2-type alloys exposed to boiling water reactor operation.

Chalmers Reproservice
Gothenburg, Sweden 2022

Evolution of microstructure and nanoscale chemistry of
Zircaloy-2-type alloys during nuclear reactor operation
Johan Eriksson
Department of Physics
Chalmers University of Technology

## Abstract

Zirconium alloys are used as fuel cladding tubes in nuclear reactors. During reactor operation, these alloys are degraded by corrosion, hydrogen pickup (HPU), and radiation-induced growth, processes influenced by the alloying elements. The alloy Zircaloy-2, which contains Sn, Fe, Cr, Ni, and O as alloying elements, is commonly used in boiling water reactors (BWRs). This thesis deals with atom probe tomography (APT) investigations of Zircaloy-2 and a similar model alloy, Alloy 2, before and after up to nine years of BWR operation. Alloy 2 contains more Fe and Cr and exhibits lower corrosion and HPU.

Less than 10 wt ppm each of Fe, Cr, and Ni was observed in the matrix of as-produced Zircaloy-2 and Alloy 2 of commercial heat treatment, a consequence of very low solubility and formation of second phase particles (SPPs). After reactor exposure, these elements were found in nanoscale clusters that were located at radiation-induced ⟨a⟩-type dislocation loops. The amount of Fe, Cr, and Ni in clusters increased with increasing fluence. There were two main types of clusters, spheroidal Fe–Cr clusters and disc-shaped Fe–Ni clusters. On average there were no large differences in clusters before and after acceleration in degradation, only small increases in cluster number density, cluster size, and cluster Cr content. ⟨c⟩-component loops decorated with Sn, Fe, and Ni were observed after but not before acceleration in degradation. Sn formed a network-like structure. No differences in cluster and matrix chemistry between Zircaloy-2 and Alloy 2 were observed after reactor exposure, indicating that the improved properties of Alloy 2 are related to additional Fe and Cr being located in SPPs.

It was possible to analyse the materials using voltage-pulsed APT. Voltage pulsing was needed to reliably determine Fe–Ni cluster composition and shape. Fe–Cr clusters were observed also using laser-pulsed APT. Focused-ion-beam (FIB) preparation of APT specimens at room temperature resulted in phase transformation from α-Zr to γ-hydride, whereas cryo-FIB preparation did not. The average number of ions detected before specimen fracture was higher for γ-hydride specimens. There were no significant differences in clustering of Fe, Cr, and Ni between α-Zr and γ-hydride specimens.

**Keywords:** Zirconium alloys, Zircaloy-2, Radiation effects, Dislocation loops, Clustering, Nuclear fuel cladding, Boiling water reactor, Atom probe tomography

# Preface

The research presented in this thesis was carried out at the Division of Microstructure Physics at the Department of Physics, Chalmers University of Technology, Gothenburg, Sweden, during the time period March 2018–October 2022, under the supervision of Associate Professor Mattias Thuvander, Professor Hans-Olof Andrén, and Dr Mohammad Sattari. The work was performed as part of the international MUZIC-3 consortium and was funded by Westinghouse Electric Sweden AB, Vattenfall AB, OKG AB, and the Electric Power Research Institute (EPRI).

Parts of the work presented in this doctoral thesis have previously been published in a licentiate thesis by the same author. Papers I and II present results that have been obtained by evaluating APT data from experiments performed by Gustav Sundell during his PhD project. The work presented in Papers IV–VI was performed in collaboration with David Mayweg.

## List of appended papers

I. *An atom probe tomography study of the chemistry of radiation-induced dislocation loops in Zircaloy-2 exposed to boiling water reactor operation*
J. Eriksson, G. Sundell, P. Tejland, H.-O. Andrén, M. Thuvander
Journal of Nuclear Materials 550, 152923 (2021).

II. *Nanoscale chemistry of Zircaloy-2 exposed to three and nine annual cycles of boiling water reactor operation — an atom probe tomography study*
J. Eriksson, G. Sundell, P. Tejland, H.-O. Andrén, M. Thuvander
Journal of Nuclear Materials 561, 153537 (2022).

III. *Microstructure development of Zircaloy-2 cladding of type LK3/L during service in the Leibstadt BWR: A review*
J. Eriksson, H.-O. Andrén, M. Limbäck, M. Thuvander, S. Abolhassani
In manuscript.

IV. *Solute Concentrations in the Matrix of Zirconium Alloys Studied by Atom Probe Tomography*
J. Eriksson, D. Mayweg, G. Sundell, H.-O. Andrén, M. Thuvander
Accepted for publication in ASTM STP1645, 2022.

V. *An atom probe tomography investigation of the nanoscale chemistry of two Zircaloy-2-type alloys with different iron and chromium content exposed to boiling water reactor operation*
J. Eriksson, D. Mayweg, H.-O. Andrén, M. Thuvander
In manuscript.

VI. *Focused Ion Beam induced transformation from α-Zr to γ-hydride does not change Fe, Ni, Cr-clusters in irradiated Zircaloy-2*
D. Mayweg, J. Eriksson, A.J. Breen, M. Thuvander
Submitted to Journal of Nuclear Materials.

## My contributions to the appended papers

I. I performed the data analysis and wrote the paper, with input from co-authors.

II. I performed the data analysis and wrote the paper, with input from co-authors.

III. I wrote the paper together with co-authors.

IV. I performed part of the experimental work, performed most of the data analysis, and wrote the paper together with co-authors.

V. I performed part of the experimental work, performed part of the data analysis, and wrote the paper together with co-authors.

VI. I performed part of the experimental work, assisted in interpretation of the results, and assisted in writing the paper.

# Table of Contents


**1. Introduction** ..... 1
1.1 Background ..... 1
1.2 Aim ..... 2
**2. Nuclear reactors** ..... 5
**3. Zr alloy nuclear fuel claddings** ..... 9
3.1 Types of alloys ..... 9
3.2 Crystallography ..... 10
3.3 Chemistry ..... 14
3.4 Manufacture and texture ..... 15
**4. Irradiation effects on Zr alloys** ..... 17
4.1 Point defects and dislocation loops ..... 17
4.2 Irradiation growth and irradiation creep ..... 22
4.3 SPP dissolution and alloying element redistribution ..... 23
4.4 Pellet–cladding interaction ..... 24
**5. Corrosion of Zr alloys** ..... 25
5.1 General corrosion phenomena in autoclave and in reactor ..... 25
5.2 Effects of SPPs, alloying elements, and impurities ..... 28
**6. H pickup and hydride phases in Zr alloys** ..... 31
**7. Experimental techniques** ..... 35
7.1 Atom probe tomography ..... 35
7.1.1 Overview ..... 35
7.1.2 Specimen reconstruction and data evaluation ..... 39
7.1.3 Limitations and artefacts ..... 44
7.1.4 Atom probe tomography of Zr alloys ..... 47
7.2 Specimen preparation ..... 50
7.2.1 Electropolishing ..... 50
7.2.2 Focused ion beam–scanning electron microscopy ..... 51
**8. Materials studied** ..... 53
8.1 Papers I, II, and III ..... 54
8.2 Papers IV, V, and VI ..... 56
**9. Summary of results and discussion** ..... 61
9.1 Matrix chemistry in the unirradiated metal ..... 61
9.2 Irradiation effects ..... 64
9.2.1 General observations ..... 64
9.2.2 Clustering of Fe, Cr, and Ni ..... 65

9.2.3 Distribution of Sn ..... 70
9.2.4 ⟨c⟩-component loops ..... 72
9.3 Effects of higher Fe and Cr content ..... 73
9.4 In-reactor degradation ..... 76
9.4.1 Corrosion and H pickup ..... 76
9.4.2 Growth ..... 77
9.5 Introduction of H during APT specimen preparation ..... 78
**10. Conclusions and outlook** ..... 81
10.1 Conclusions ..... 81
10.2 Outlook ..... 82
**Acknowledgements** ..... 85
**References** ..... 87

# 1. Introduction

The applications of the materials in focus of this thesis are within the nuclear industry. In this chapter, the reason for performing the research presented in this thesis and the aim of this research are explained.

## 1.1 Background

Nuclear power is one of the major methods of producing electricity in the world. In 2021, about 10 % of the world's electricity production was generated by nuclear power [1]. In studies comparing the main sources of electricity production, nuclear power is, per unit electric energy generated, among the sources with lowest greenhouse gas emissions, lowest land use, lowest impact on ecosystems, and lowest impact on human health [2]. If an increased demand for electricity by a growing human population is to be met with low greenhouse gas emissions and reasonably low impacts on biodiversity and human health, nuclear power thus has the capability of making a significant contribution. A more efficient use of the nuclear fuel would allow for more electricity to be generated from the existing uranium reserves and would lead to a lower amount of highly radioactive waste being produced in nuclear reactors. In the vast majority of current reactor designs, the performance of zirconium alloys is one of the factors that limit more efficient fuel utilisation, thereby motivating research aiming at improving the properties of Zr alloys. Improved Zr alloys that are more resistant to degrading mechanisms might, furthermore, enable safer operation of nuclear power plants.

According to the International Atomic Energy Agency (IAEA), in the end of 2021, worldwide, there were 437 operational nuclear power reactors and 56 under construction [3]. In almost all of these nuclear reactors, Zr alloys are used as cladding tubes for the nuclear fuel or as structural core components.

In the harsh environment inside the core of a nuclear reactor in operation, a combination of radiation effects, corrosion, and hydrogen pickup (HPU) contributes to degradation of the cladding. Notable phenomena are irradiation growth, which refers to dimensional changes of the material while the volume remains constant [4], and hydrogen embrittlement. Although a lot of research to understand the degrading mechanisms and their interrelation has been undertaken during the approximately 70 years that Zr alloys have been in use in nuclear reactors, their detailed nature still is unclear. As the performance of characterisation techniques has improved over the years, it is now possible to study the degradation of Zr alloys in more detail than previously.

## 1.2 Aim

The alloying elements of Zr alloys affect irradiation growth [4], corrosion [5], and HPU [6] during reactor operation. It is thus of interest to study the relation between radiation-induced defects and alloying elements.

The aim of this work is to get information that can be used to understand how the in-reactor degradation of Zr alloys occurs and evolves over time; more specifically, to study the effect of alloying elements in Zircaloy-2-type alloys on this matter. To obtain the desired information, investigations of the nanoscale chemistry of Zircaloy-2-type alloys before and during various stages of nuclear reactor operation have been performed. Atom probe tomography (APT) has been the main technique used in this work. Parts of the work presented in this doctoral thesis have previously been presented in a licentiate thesis by the same author [7].

From previous work it is known that the matrix content of solute elements in Zr alloys is very low [8–15], but precise concentrations of these elements in as-produced commercial alloys have not been established. To compare the materials before and after reactor operation, more studies in the as-produced state are thus needed. Furthermore, it is not clear how large quantities of solutes that can be retained in the matrix via heat treatment at high temperature followed by fast cooling.

It is known that the alloying elements are redistributed after reactor operation [16–24]. Fe, Cr, and Ni are known to be located in nanometre-sized clusters at radiation-induced defects [18,19,21,22]. In previous APT work, clusters of essentially only Fe and Cr have been observed [18], whereas in previous transmission electron microscopy (TEM) work clusters also containing Ni have been observed [21,22]. There is thus a discrepancy between the observations made using APT and the observations made using TEM. The APT work on in-reactor-exposed Zr alloys previously performed at Chalmers University was performed on the alloy Zircaloy-2 that had been exposed for three (3C) or nine annual cycles (9C) in the boiling water reactor (BWR) at Kernkraftverk Leibstadt (KKL) in Switzerland [18,19,23]. The material was investigated after these two operating times, as they correspond to before and after an acceleration (sometimes referred to as breakaway) in growth, corrosion, and HPU. The previous work [18,19,23] did not contain any detailed cluster anaylsis comparing the two operating times.

In comparison with commercial Zircaloy-2, a model alloy, called Alloy 2, containing more Fe and more Cr, has exhibited significantly lower HPU and slightly lower corrosion during reactor operation [25]. The role of the increased Fe and Cr content leading to the improved properties of Alloy 2 are not known. Therefore, comparing these two alloys before and after reactor operation is of interest.

In order to obtain more information on the matrix content of solutes in as-produced Zr alloys, on the possibility of supersaturating the Zr alloy matrix with solutes, on the role of Ni in the degradation, on the difference in nanoscale chemistry before and after accelerated degradation, and on the roles of Fe and Cr in improving the HPU and the

corrosion of Zircaloy-2-type alloys, the research performed in this thesis has the following objectives:

- To measure the content of solutes in the matrix of as-produced, as well as in-reactor-exposed, Zircaloy-2 and Alloy 2 of the commercial heat treatment LK3.

- To study the influence of annealing at 770 °C followed by various cooling rates on the matrix content of Zircaloy-2.

- To study the distribution of Ni and its presence in clusters.

- To compare the 3C and 9C materials from KKL, including a quantitative comparison of clusters.

- To investigate the difference in nanoscale chemistry in the metal of Zircaloy-2 and Alloy 2 exposed to two different neutron fluences during BWR operation.

Additionally, in the experimental work of this thesis, more hydrogen than expected from the hydrogen content of the material was observed in the APT analyses. To better understand the origins of the measured hydrogen signal, the influences of specimen preparation method and analysis conditions on this matter were studied.

## 2. Nuclear reactors

A variety of nuclear reactor designs exists, and there are multiple ways of classifying reactor types. Common ways are to classify according to the type of nuclear reaction occurring, according to the cooling medium, or according to the moderator material. Most nuclear reactors are thermal fission reactors, utilising thermal neutrons, i.e. neutrons of approximate energy 0.025 eV, to induce fission in the nuclear fuel [26]. Of the thermal reactors, light-water reactors (LWRs) constitute the most common subclass [27]. In LWRs, water is used for neutron moderation and cooling of the fuel. The name light-water reactor is used to distinguish LWRs from heavy-water reactors, which instead use heavy water for neutron moderation and cooling.

The nuclear fuel in LWRs consists of cylindrical $UO_2$ pellets, typically slightly less than 1 cm in diameter and a little larger in height [28]. These pellets are placed in cladding tubes made of Zr alloys, having a height of approximately 4 m, a diameter around 1 cm, and a wall thickness in the approximate range 0.6–0.8 mm [29]. The top and bottom of the tubes are sealed by welded end plugs, and He gas under pressure (ranging from approximately 1–35 bar depending on design) is used to maintain a gap between the tube inside and the fuel pellets [28]. The stack of pellets is held in position by a spring or a clip from the topmost pellet to the top plug. The space between the stack of pellets and the top plug is called the plenum region and is the volume in which gases released in the fission process are contained (unless the integrity of the fuel rod is broken). A number of cladding tubes are grouped together to form a fuel assembly, and several hundreds of fuel assemblies are grouped together to form the core of the reactor. The core is located inside a reactor pressure vessel. The water used as cooling medium and moderator flows through the core. Thus, the Zr cladding tubes, which are in direct contact with the water, function as a barrier between the fuel and the water.

Compared with natural U, the U in the fuel pellets in LWRs is isotopically enriched in $^{235}U$. The isotopic percentage of $^{235}U$ in fresh fuel is 3–5 %, the rest, except for trace amounts of $^{234}U$, being $^{238}U$. In a fast neutron flux, $^{238}U$ can, via neutron capture succeeded by $\beta^-$-decays, be transmuted to $^{239}Pu$ [30]. Thermal neutrons can induce fission of $^{235}U$ and $^{239}Pu$ [30]. In each fission event, one of these nuclides is split into two smaller nuclides, called fission fragments, and a few fast neutrons, on average approximately 2.4 for $^{235}U$ and 2.9 for $^{239}Pu$ [26]. The fast neutrons are moderated, i.e. slowed down, by the water in the reactor to reach thermal energies. When thermal, the neutrons can induce fission in other $^{235}U$ and $^{239}Pu$ nuclei. In a nuclear reactor, a critical chain reaction is sustained, i.e. the neutrons released in one fission event give on average rise to exactly one new fission event. The energy released is large, about 200 MeV per fission event, and is imparted as kinetic energy of the fission fragments. When the fission fragments slow down, the temperature inside the fuel pellet increases. Heat is conducted through the pellet and through the Zr alloy cladding (which is exposed to approximately 400 °C on the inside and about 300 °C on the outside) to increase the thermal energy of the coolant water. This thermal energy is converted to electricity via turbines and generators.

There are two types of LWRs, pressurised water reactors (PWRs) and BWRs. In PWRs there are two water circuits, the primary and the secondary. The water of the primary circuit is heated while passing through the core in the reactor pressure vessel, is cooled in steam generators, and is pumped back into the reactor pressure vessel. At all times during normal operation, the pressure of the primary circuit is kept high enough to keep its water liquid. The water of the secondary circuit is transformed to steam in the steam generators, passes through the turbines, is condensed in the condensers, and is pumped back into the steam generators. In BWRs the water that passes through the core is heated and starts boiling inside the reactor pressure vessel. The steam thus generated goes to the turbines, is condensed in the condensers, and is pumped back into to the reactor pressure vessel. The typical operating pressure in a PWR core is around 15 MPa, and the temperature of the outgoing water from the core is around 320 °C [31]. The pressure of a BWR core is around 7 MPa, and the temperature of the steam is usually 286 °C [31]. A schematic of a PWR and a BWR is shown in Figure 2.1.

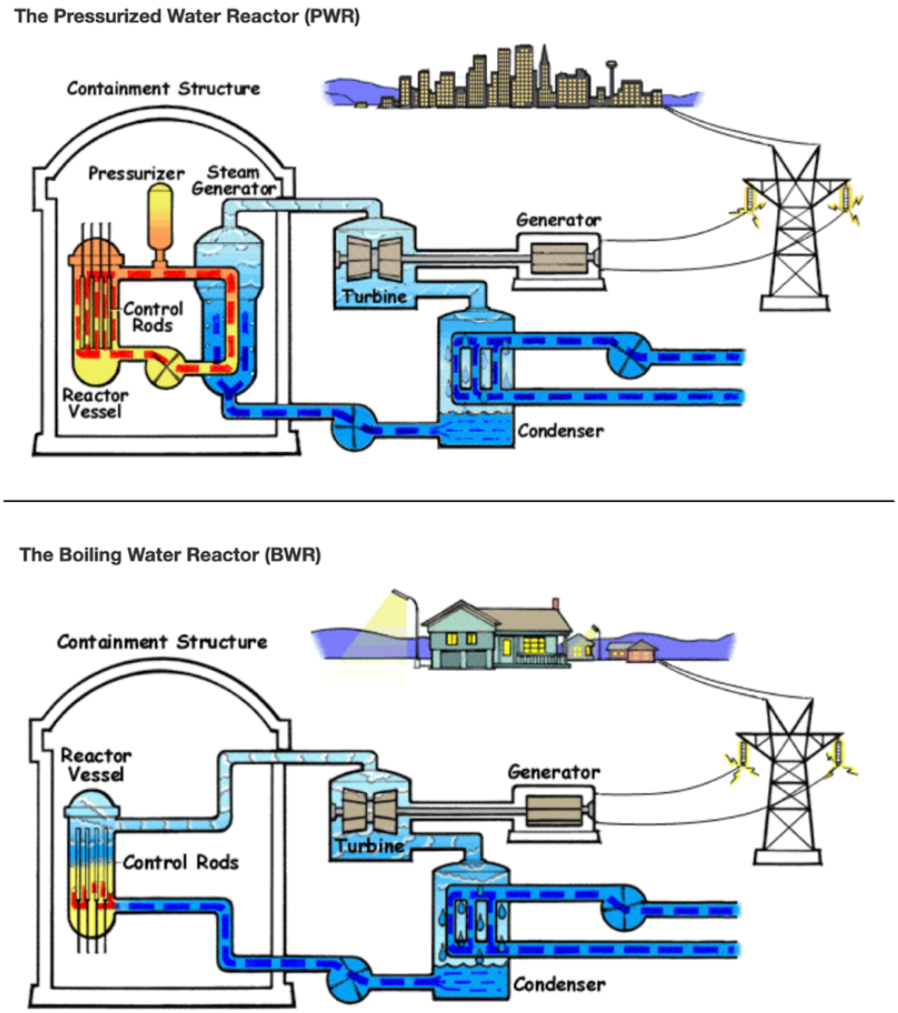


*Figure 2.1: Schematic of a PWR and a BWR. From* [32] *and* [33].

The design of the core differs between PWRs and BWRs. In both types of reactors, the fuel assemblies are arrays of fuel rods held together with so-called fuel rod spacer grids to keep the rods in correct position. The PWR fuel assemblies are generally quadratic with 14 × 14 to 18 × 18 rods in each array for non-Russian reactor designs and hexagonal with up to more than 300 fuel rods in each array for Russian reactor designs, so-called VVERs (or WWERs). Control rods containing neutron-absorbing material that stops the nuclear chain reaction can be inserted at positions in the fuel assemblies where the fuel rods have been replaced by control rod guide tubes. The number of fuel rods in PWR assemblies is inherent to the reactor design and cannot be changed. In BWR fuel assemblies, the arrays are quadratic with, most commonly, 10 × 10 or 11 × 11 rods in each array. For reasons of flow stability, each fuel assembly is surrounded by a channel box made of Zr alloy. Fuel assemblies are grouped together in units of four, and, in each group, control blades containing neutron-absorbing material can be inserted between the channel boxes. The number of fuel rods in BWR assemblies is not inherent to the reactor design and varies between different assembly designs. A larger number of fuel rods in the assembly gives a higher power density, and modern fuel assemblies therefore have a higher number of fuel rods than older designs. The total number of fuel rods is in the approximate range 40 000–60 000 in a PWR core and 50 000–90 000 in a BWR core [28]. Fuel assemblies for BWRs and PWRs (of non-Russian design) are shown in Figure 2.2.

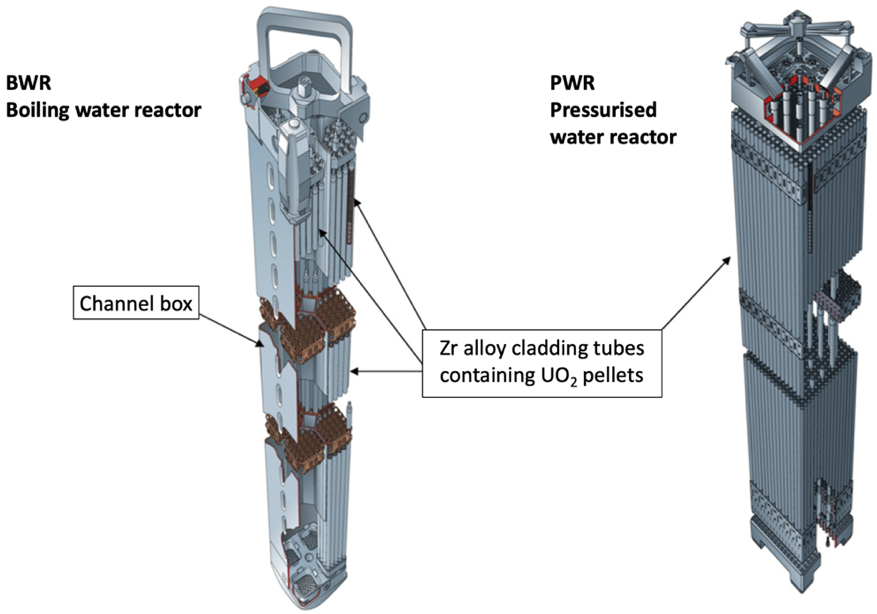


*Figure 2.2: Schematic of fuel assemblies for BWRs and PWRs. Adapted from* [34]. *Republished with permission from Elsevier.*

# 3. Zr alloy nuclear fuel claddings

A number of different Zr alloys are used for nuclear fuel claddings. In this chapter some of the most common are described along with some of the basics of crystallography, chemistry (with emphasis on the Zircaloys), and manufacture and texture of Zr alloys. The main reference for this chapter is [29]. Additional references are stated in the text.

## 3.1 Types of alloys

Zr alloys have been used as nuclear fuel cladding since the 1950s, their low absorption cross section for thermal neutrons being their main advantage [35]. Various types of Zr alloys have been developed over the years. In PWRs of non-Russian design, Zircaloy-4 has historically been the most common, but nowadays Nb-containing Zr alloys are generally used. In VVERs, Nb-containing Zr alloys have been used throughout most of their history. This is also the case for RBMKs (graphite-moderated, light-water-cooled reactors of Russian design) and CANDU reactors (heavy-water reactors of Canadian design). However, CANDU reactors also use Zircaloy-2 and Zircaloy-4 for some components. Examples of Nb-containing alloys are ZIRLO® [1], Optimized ZIRLO™ [1], M5® [1] (all three used in PWRs), E110, E125, E635 (all three used in reactors of Russian design), and Zr-2.5Nb (used in CANDU reactors). In BWRs, Zircaloy-2 has been and still is the most common Zr alloy. HiFi™ [1] and GNF-Ziron are two newly developed BWR claddings that have a slightly higher Fe content than Zircaloy-2 [36]. The higher Fe content results in lower HPU compared with Zircaloy-2 [36]. For channel boxes in BWRs, Nb-containing Zr alloys are often used in modern fuel assemblies [36]. Table 3.1 shows the composition of some of the most common Zr alloys and the model alloy studied in this work, Alloy 2.

[1] ZIRLO®, Optimized ZIRLO™, HiFi™ are trademarks or registered trademarks of Westinghouse Electric Company LLC, its affiliates and/or its subsidiaries in the United States of America and may be registered in other countries throughout the world. All rights reserved. Unauthorised use is strictly prohibited. M5® is a registered trademark of Framatome and/or its affiliates. Other names may be trademarks of their respective owners.

*Table 3.1: Content of alloying elements (wt%) in some of the most common Zr alloys and Alloy 2. O is usually also present as an alloying element, not always within a specified range but typically below 0.2 wt%.*

| Alloy | Sn | Fe | Cr | Ni | Nb |
|---|---|---|---|---|---|
| **Zircaloy-2**[1] | 1.20–1.70 | 0.07–0.20 | 0.05–0.15 | 0.03–0.08 | - |
| **Zircaloy-4**[1] | 1.20–1.70 | 0.18–0.24 | 0.07–0.13 | - | - |
| **ZIRLO**[2] | 0.9–1.2 | 0.1 | - | - | 0.9–1.13 |
| **Optimized ZIRLO**[3] | 0.6–0.79 | 0.1 | - | - | 0.8–1.2 |
| **M5**[2] | - | 0.015–0.06 | - | - | 0.8–1.2 |
| **E110**[2] | - | 0.006–0.012 | - | - | 0.95–1.05 |
| **E125**[4] | - | - | - | - | 2.20–2.60 |
| **E635**[2] | 1.10–1.30 | 0.30–0.40 | - | - | 0.95–1.05 |
| **Zr-2.5Nb**[1] | - | - | - | - | 2.50–2.80 |
| **HiFi**[5] | 1.20–1.70 | 0.25–0.50 | 0.05–0.15 | 0.03–0.08 | - |
| **GNF-Ziron**[6] | 1.46 | 0.26 | 0.10 | 0.05 | - |
| **Alloy 2** | 1.31 | 0.36 | 0.18 | 0.06 | - |

[1]Values from [37].
[2]Values from [38].
[3]Values from [39].
[4]Values from [40].
[5]Values from [25].
[6]Values from [36].

## 3.2 Crystallography

Solid Zr exists in two phases, a hexagonal close-packed (HCP) α-phase below and a body-centred cubic (BCC) β-phase above 865 °C [29]. In thermal nuclear reactors, where the operating temperature is in the range 280–330 °C, Zr is in the α-phase. However, during accident conditions, the temperature can be so high that a phase transformation to the β-phase occurs.

A primitive unit cell for the hexagonal lattice can be constructed by using two $a$-axes ($a_1$ and $a_2$) and a $c$-axis. The angle between the $a$-axes is 120°, and they lie in a plane that is perpendicular to the $c$-axis. Often, a non-primitive unit cell is used to more clearly reveal the hexagonal structure. Then, a third $a$-axis ($a_3$) being ±120° from $a_1$ and $a_2$ is usually employed. A primitive and a non-primitive hexagonal unit cell are shown in Figure 3.1. For α-Zr the lattice parameters are $c = 0.515$ nm and $a = 0.323$ nm, and the $c/a$-ratio is 1.59, which is somewhat lower than the ideal $c/a$-ratio of $2\sqrt{2/3}$ ($\approx 1.63$) for an HCP lattice [41]. There are two atoms in the primitive unit cell with coordinates 000 and $\frac{2}{3}\frac{1}{3}\frac{1}{2}$ ($a_1 a_2 c$) [41]. In HCP lattices, there are two octahedral and four tetrahedral interstitial sites per primitive unit cell (both of the octahedral and two of the tetrahedral sites are fully contained within the cell, and eight tetrahedral sites are shared with three other cells each) [41]. However, the configuration of interstitial atoms is often such that

two atoms are associated with one lattice site. According to modelling using empirical potentials, taking the possible association of two atoms with one lattice site into account, there are eight interstitial configurations, tetrahedral (T), octahedral (O), basal tetrahedral (BT), basal octahedral (BO), crowdion (C), basal crowdion (BC), split (dumbbell) (S), and basal split (dumbbell) (BS) in HCP lattices [42]. In addition to these configurations, there are according to density-functional theory (DFT) modelling four more configurations that could be stable [43]. These are C′ and BC′, which can be formed by breaking the symmetry of C and BC, respectively, and PS and P2S, which can be formed by breaking the symmetry of S. Figure 3.2 shows the conventional interstitial configurations obtained using empirical potentials, and Figure 3.3 shows the additional configurations obtained using DFT modelling.

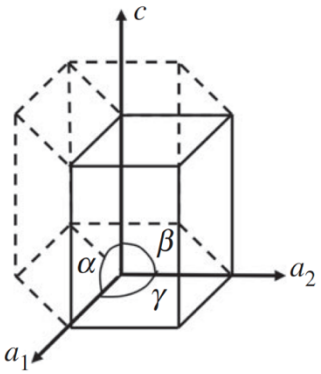


*Figure 3.1: Primitive unit cell (solid lines) and non-primitive unit cell (dashed lines) of the hexagonal lattice. $\alpha = \beta = 90°$. $\gamma = 120°$. Republished with permission from The Royal Society (U.K.),* [44].

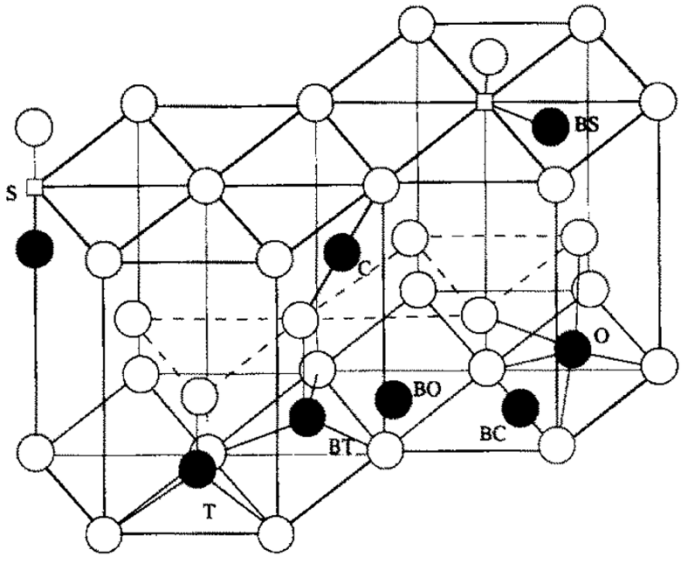


*Figure 3.2: Interstitial sites in the HCP lattice. Republished with permission from Elsevier,* [45].

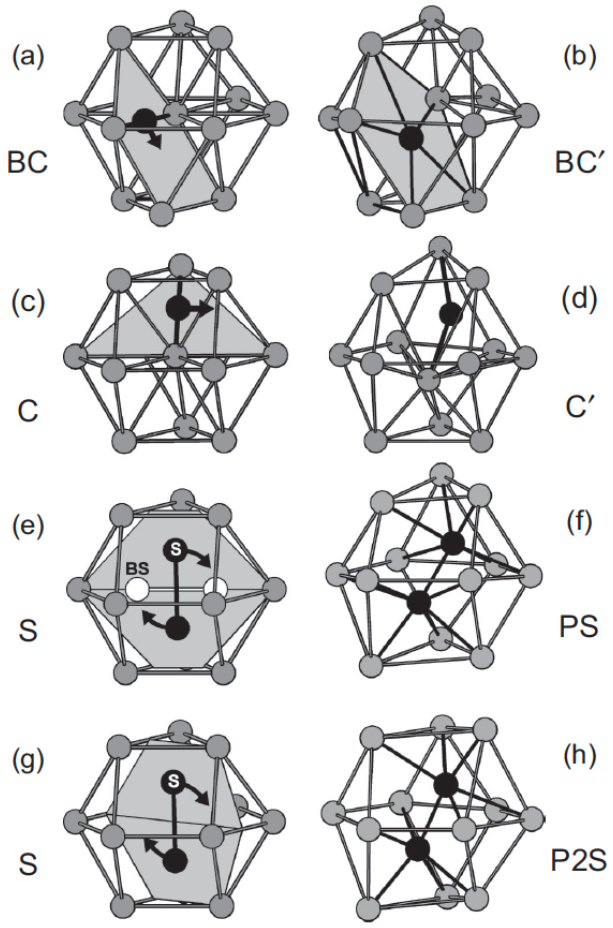


*Figure 3.3: Low-energy interstitial sites formed by breaking the symmetry of the conventional interstitial sites in the HCP lattice. Republished with permission from the American Physical Society,* [43].

Often, the hexagonal lattice system is described using the Miller–Bravais notation, a notation with four indices, $(hkil)$, where $i = -(h + k)$ [46]. The third index, $i$, is thus redundant but used for convenience due to the symmetry of the lattice. Indices within parentheses, $(hkil)$, denote families of planes, indices within braces, $\{hkil\}$, denote all planes equivalent to the families of planes $(hkil)$, indices within square brackets, $[hkil]$, denote directions, and indices within angle brackets, $\langle hkil \rangle$, denote all directions equivalent to the directions $[hkil]$. In contrast to cubic lattices, directions in the hexagonal lattice are not always normal to the planes with the same indices. A number of atomic planes in the hexagonal lattice can be of interest when discussing radiation-induced defects. Figure 3.4 shows the basal, the first-order pyramidal ($\{01\bar{1}1\}$), and the first-order ($\{10\bar{1}0\}$) and second-order ($\{11\bar{2}0\}$) prismatic planes together with the $\langle c \rangle$-direction ($[0002]$) and the $\langle a \rangle$-directions ($\langle 11\bar{2}0 \rangle$) of the lattice. For HCP lattices with a $c/a$-ratio lower than $\sqrt{3}$ ($\approx 1.73$), e.g. Zr, the interplanar spacing is smallest for the $(0002)$ planes, and for HCP lattices with a $c/a$-ratio higher than $\sqrt{3}$, the interplanar spacing is smallest for the $\{10\bar{1}0\}$ planes [47]. The stacking order of the $(0002)$ planes

is *ABAB*…, and the stacking order of the $\{10\bar{1}0\}$ planes is *ABCDA*…, with the distance between A and B and between C and D equal to $a\sqrt{3}/6$ and the distance between B and C and between D and A equal to twice this distance [48]. The pairs A–B and C–D are sometimes referred to as corrugated (first-order) prismatic planes, and the distance between these corrugated planes $\left(= a\sqrt{3}/2\right)$ is usually what is meant by the interplanar spacing of the $\{10\bar{1}0\}$ planes. Figure 3.5 shows the stacking of the $\{10\bar{1}0\}$ planes.

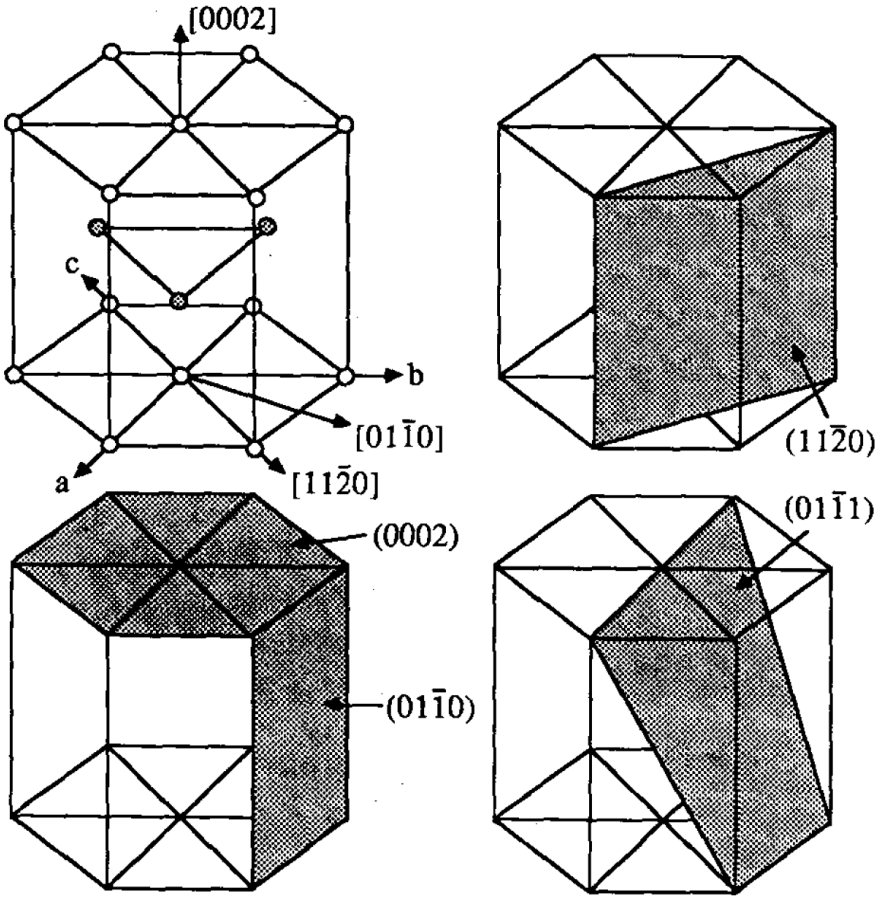


*Figure 3.4: Directions and planes in the hexagonal lattice. a, b, and c in the top left unit cell correspond to three of the ⟨a⟩-directions (and thus correspond to the three a-axes $a_1$, $a_2$, $a_3$).* $[0002]$ *indicates the* $\langle c \rangle$*-direction.* $(11\bar{2}0)$ *is a second-order prismatic plane,* $(01\bar{1}0)$ *is a first-order prismatic plane,* $(0002)$ *is the basal plane, and* $(01\bar{1}1)$ *is a first-order pyramidal plane. Republished with permission from IEEE,* [49].

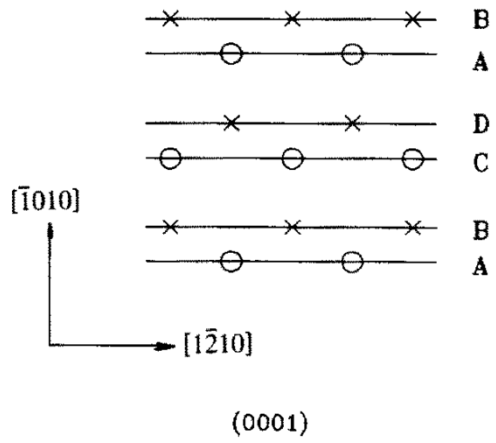


*Figure 3.5: Stacking of prismatic planes in the HCP lattice. The circles correspond to the white and the crosses to the grey atoms in Figure 3.4. The pairs A–B and C–D are referred to as corrugated (first-order) prismatic planes. Republished with permission from Elsevier,* [48].

## 3.3 Chemistry

The alloys in focus of this study are Zircaloy-2 and the very similar Alloy 2. The detailed composition range of Zircaloy-2 is shown in Table 3.2, together with the reason for adding each of the alloying elements. Alloy 2 (composition shown in Tables 3.1 and 8.3) has about twice as high Fe content as the maximum of Zircaloy-2 and Cr content slightly above the maximum of Zircaloy-2. As Alloy 2 otherwise fulfils the Zircaloy-2 standard, it can be called a Zircaloy-2-type alloy. For comparison, the composition range of Zircaloy-4 is shown in the table. Zircaloy-4 contains no Ni. The reason for this is that HPU is decreased without the presence of Ni. On the other hand, Ni improves the corrosion resistance. Due to the different environments in BWR and PWR cores, Zircaloy-2 is preferred in BWRs and Zircaloy-4 PWRs. In addition to the elements specified in Table 3.2, there are impurity levels of various elements present in the Zr alloys. Common impurities in Zircaloy-2 are C, N, Si, and Al [50,51].

*Table 3.2: Composition of Zircaloy-2 and Zircaloy-4 (wt%) and the role of each alloying element. Values from ASTM Standard B350/B350M* [37].

| Element | Zircaloy-2 | Zircaloy-4 | Role of alloying element |
|---|---|---|---|
| **Sn** | 1.20–1.70 | 1.20–1.70 | Increases yield strength and corrosion resistance |
| **Fe** | 0.07–0.20 | 0.18–0.24 | Increases corrosion resistance |
| **Cr** | 0.05–0.15 | 0.07–0.13 | Increases corrosion resistance |
| **Ni** | 0.03–0.08 | - | Increases corrosion resistance |
| **Fe + Cr + Ni** | 0.18–0.38 | - | |
| **Fe + Cr** | - | 0.28–0.37 | |
| **O** | To be specified on order | To be specified on order | Increases yield strength |

The solubilities of Fe, Cr, and Ni are low in Zr. In the Zircaloys, second phase particles (SPPs) of the types $Zr_2(Fe,Ni)$ and $Zr(Fe,Cr)_2$ are formed. The $Zr_2(Fe,Ni)$ SPPs (in Zircaloy-2) have been observed to be fewer in number and generally larger than the $Zr(Fe,Cr)_2$ SPPs [22,52–55]. Also Si can be found in the SPPs [51]. O and Sn are α-stabilisers and do not form SPPs. Fe, Cr, and Ni are interstitial diffusers, and their diffusivity is about three times faster in the ⟨c⟩-direction than in the ⟨a⟩-directions of the Zr lattice. The diffusivities of Fe and Ni are higher than the diffusivity of Cr, and at temperatures of reactor operation the difference is several orders of magnitude [56]. Also O is an interstitial diffuser, and its diffusivity at temperatures of reactor operation is a few orders of magnitude lower than the diffusivity of Cr. Sn, as well as Nb, is a substitutional diffuser with slower and more isotropic diffusion [56].

### 3.4 Manufacture and texture

In Zr alloy manufacture, the starting material is usually ore containing both Zr and Hf. Due to the high thermal neutron capture cross section of Hf, a separation of the two elements is performed. The Zr is purified further before being mixed with the alloying elements and melted to form ingots. The thermal treatments and mechanical processing performed after this step vary between different alloys and different applications but usually comprise high-temperature forging or rolling in the β-phase (at 1000–1050 °C), extrusion (for tubes) in the β-phase, water-quenching from the β-phase, intermediate-temperature forging and rolling (for sheets) or extrusion (for tubes) in the upper α-phase, and a number of low-temperature rollings or pilgerings with intermediate annealings. During treatment in the β-phase, the SPPs are dissolved, the material is homogenised, and large grains are formed. Upon quenching, a basketweave structure of α-grains forms with SPPs at the grain boundaries. The succeeding processing steps lead to a more homogeneous distribution of SPPs. The annealings between the low-temperature processing steps are performed to increase the ductility of the final product. A fully recrystallised (RXA) product with equiaxed grains and SPPs both inside the grains and at the grain boundaries can be obtained. If the temperature of the final annealing step is decreased, a stress-relieved (SRA) product with elongated grains and improved mechanical properties can be obtained. It is also possible to get a partly recrystallised (PRXA) structure.

The crystallographic orientation of the grains in the final fuel cladding tubes is strongly anisotropic. The ⟨c⟩-direction of the matrix is preferentially oriented approximately 30° from the radial direction of the tube, and one of the directions $\langle 10\bar{1}0\rangle$ and $\langle 11\bar{2}0\rangle$ is in or close to the axial direction [57]. Figure 3.6 shows the typical texture of Zr alloy cladding tubes.

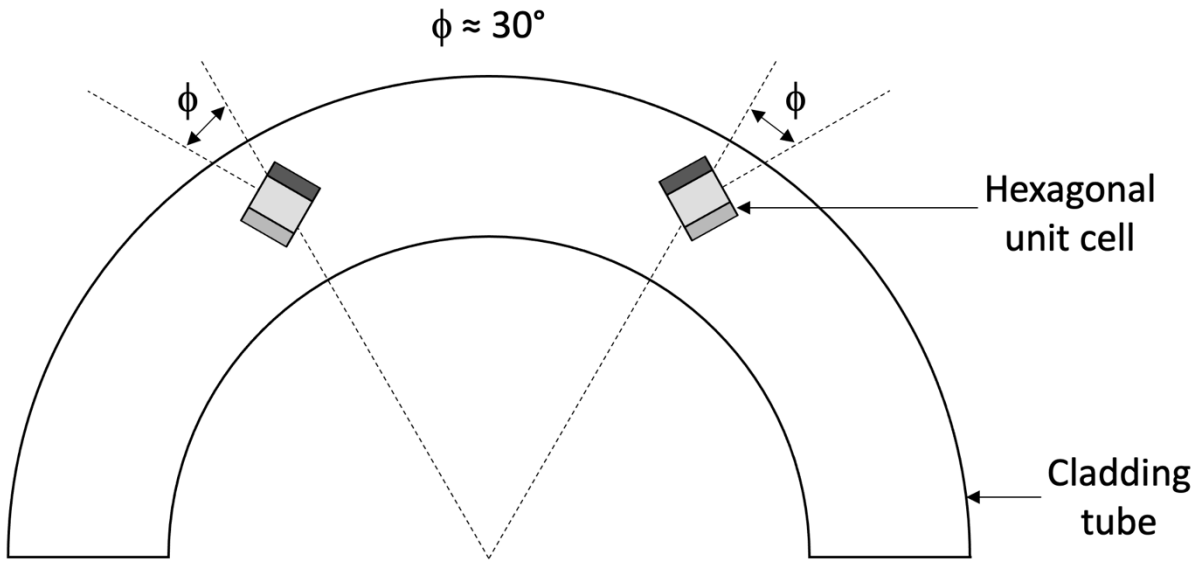


*Figure 3.6: Schematic of the typical cladding tube texture. The hexagonal unit cells are oriented approximately 30° from the radial direction.*

# 4. Irradiation effects on Zr alloys

The radiation during reactor operation degrades the Zr alloys. In this chapter, the creation of point defects and dislocation loops, irradiation growth and irradiation creep, radiation-induced SPP dissolution, and pellet–cladding interaction are described.

## 4.1 Point defects and dislocation loops

The main references for this section are [29,58]. Additional references are stated in the text.

In nuclear reactors, radiation damage in the Zr alloys is primarily caused by fast neutrons knocking out atoms from their lattice positions. For this interaction to occur, a minimum neutron energy is needed. This energy is different for different crystallographic orientations. A standard value of 40 eV is, however, commonly used as the energy needed to displace a Zr atom from its lattice position. This energy is very much smaller than the energy of the fast neutrons from the fission process (> 1 MeV) but much larger than the energy of the thermalised neutrons (0.025 eV).

The first atom to be hit by the neutron and to be knocked out of its position is called the primary knock-on atom (PKA). After being knocked out, the PKA can displace other atoms, which in turn can displace other atoms, thus creating a collision cascade. The process of knocking out an atom from its lattice position creates a self-interstitial atom (SIA) and a vacancy, a so-called Frenkel pair. Most, but not all, Frenkel pairs recombine within the time frame of several picoseconds, and the resulting configuration of a cascade is considered to be a core of vacancies surrounded by interstitials [59]. Diffusion of the SIAs and vacancies that do not recombine affects the microstructural evolution of the material. In Zr and Zr alloys, the diffusion of SIAs has been proposed to be anisotropic with preferential diffusion in the basal plane, whereas the diffusion of vacancies has been proposed to be more isotropic [60,61]. This difference between SIAs and vacancies is termed diffusion anisotropy difference (DAD), and modelling using reaction kinetics and molecular dynamics (MD) indicates that this could explain parts of the microstructural evolution of Zr alloys [60,61]. However, more recent modelling using DFT, the kinetic Monte Carlo method, and rate theory indicates that, at temperatures relevant to reactor operation, vacancies instead diffuse more anisotropically than SIAs, both species diffusing preferentially in the basal plane [62]. If the more recent modelling is correct and the DAD model is invalid, some of the phenomena that could have been explained by DAD could instead be explained by formation and anisotropic diffusion of small SIA clusters [62,63].

Due to the high neutron flux and the continuous creation and recombination of Frenkel pairs during reactor operation, each individual Zr atom is displaced multiple times. Often, the average number of displacements per atom (dpa) is used to describe the radiation effect on materials. The neutron spectrum varies significantly for different types of reactors and for different positions in the core. Therefore, individual dpa values

have to be calculated for each position in each reactor. To get an approximate value, conversion factors from fast neutron fluence (of neutron energy $E > 1$ MeV) to dpa for Zr materials in PWRs and BWRs of 1.5–1.6 dpa/($10^{25}$ n $m^{-2}$) can be used [64].

The SIAs and vacancies that do not recombine can be eliminated at defect sinks, e.g. grain boundaries and surfaces, or they can form clusters that can accumulate to form e.g. small planar defects, either a piece of an extra atomic plane or a piece of a missing atomic plane. In the first case a stacking fault due to interstitials is formed, and in the second case a stacking fault due to vacancies is formed. Along the edge of such stacking faults a dislocation loop always exists. Figure 4.1 schematically shows a dislocation loop formed by condensation of vacancies and a dislocation loop formed by condensation of interstitials. Dislocation loops in Zr and Zr alloys are commonly referred to as ⟨a⟩-loops and ⟨c⟩-component loops according to the direction of their Burgers vector, **b**. The Burgers vector of a dislocation can be defined via comparing a closed circuit around a dislocation in a distorted lattice with a circuit taking the same number of steps in the same directions in an undistorted lattice where no dislocation is present. Since the lattice around the dislocation is distorted, the same circuit in the lattice without a dislocation will not be closed without an additional step. The length and direction of this step give the Burgers vector of the dislocation, as schematically shown in Figure 4.2. Unfaulting (i.e. removal of the stacking fault) of dislocation loops can occur, leading to what is termed perfect dislocation loops [47]. For this to happen, the stacking fault energy, which increases with increasing loop size, needs to be so high that the perfect loop is energetically favourable. Loops that are associated with a stacking fault are referred to as faulted loops.

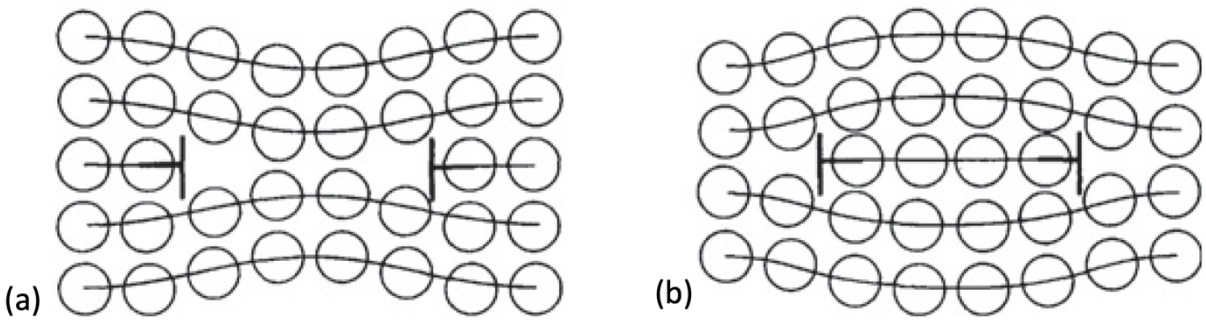


*Figure 4.1: Schematic of dislocation loops formed by condensation of (a) vacancies and (b) interstitials at an atomic plane. Republished with permission from Elsevier,* [47].

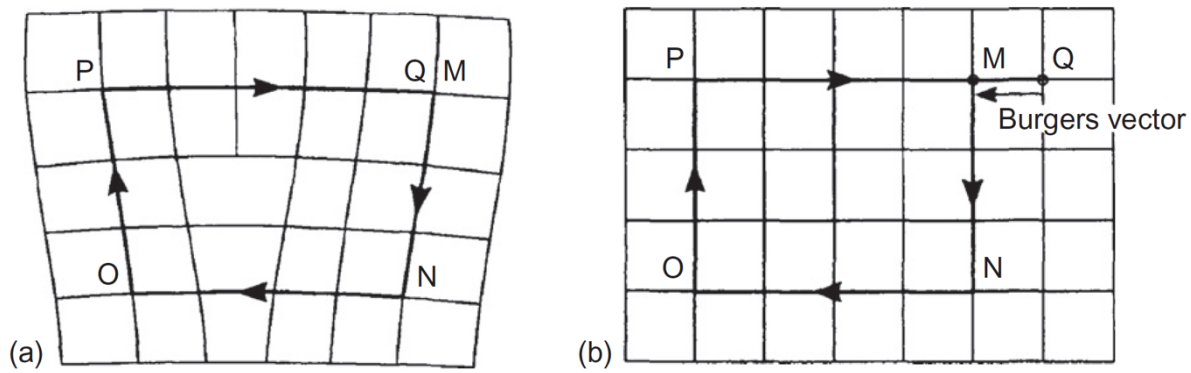


*Figure 4.2: Schematic of a Burgers circuit starting in M and ending in Q, in (a) a distorted lattice due to a dislocation and (b) a perfect lattice. The additional step needed in (b) to get back to M from Q is the Burgers vector of the dislocation. Republished with permission from Elsevier,* [47].

Vacancy ⟨a⟩-loops are considered to be formed by condensation of vacancies on two adjacent layers in the *ABCDA*… stacking of the $\{10\bar{1}0\}$ planes, as condensation of vacancies on only one plane would lead to a much higher stacking fault energy [48]. According to modelling based on empirical potentials and DFT, unfaulting of vacancy ⟨a⟩-loops is energetically favourable somewhere in the approximate loop diameter range 3–5 nm [65]. Figure 4.3 shows a schematic of unfaulting of loops on first-order prismatic planes.

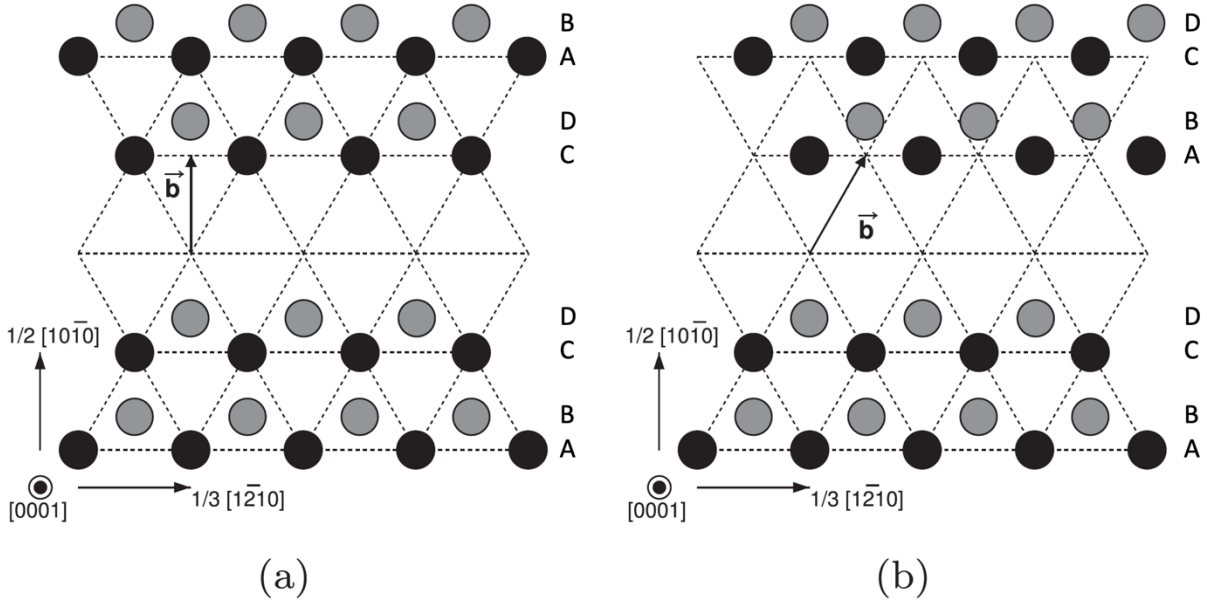


*Figure 4.3: Schematic of unfaulting mechanism for corrugated first-order prismatic planes. The stacking fault in (a) is removed by a shear, resulting in the unfaulted stacking in (b). The Burgers vector,* ***b****, in each case is indicated by an arrow. Adapted from* [65]. *Republished with permission from Elsevier.*

After unfaulting, each ⟨a⟩-loop has its Burgers vector in one of the ⟨a⟩-directions, and for the ⟨a⟩-loops observed in neutron-irradiated Zr and Zr alloys $\mathbf{b} = 1/3\langle 11\bar{2}0\rangle$ [66]. Both interstitial and vacancy ⟨a⟩-loops have been observed to coexist in various ratios depending on irradiation conditions and with large grain-to-grain variations, and both types have been reported to be perfect loops [67]. The habit plane of ⟨a⟩-loops is close to, but usually not exactly on, one of the first-order prismatic planes; they have been observed to be distributed between the first- and second-order prismatic planes but with a tilt to the ⟨c⟩-direction, meaning that they seem to inhabit various pyramidal planes [67–69]. ⟨a⟩-loops are formed already after irradiation to low neutron fluence, and they align in layers that are parallel to the basal planes of the matrix [67]. The size of ⟨a⟩-loops varies with irradiation temperature and is smaller in Zr alloys than in Zr without alloying additions [69]. After BWR exposure, ⟨a⟩-loops in Zircaloy-2 have been observed to have a diameter of approximately 5 nm [21]. A TEM micrograph showing ⟨a⟩-loops aligned in layers perpendicular to the ⟨c⟩-direction is shown in Figure 4.4, which also shows a schematic illustrating how ⟨a⟩-loops are aligned on planes that are close to $\{10\bar{1}0\}$ and how they are imaged in TEM.

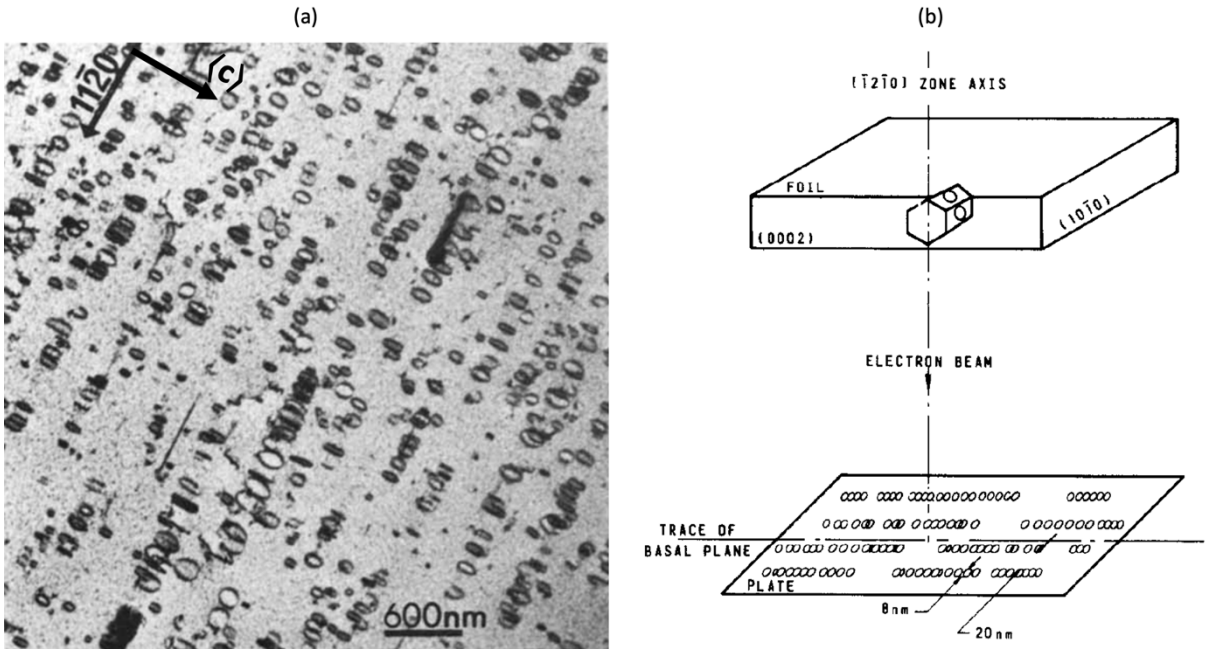


*Figure 4.4: (a) TEM micrograph of ⟨a⟩-loops aligned in layers perpendicular to the ⟨c⟩-direction in neutron-irradiated pure Zr. The approximate* $[11\bar{2}0]$ *direction (one of the ⟨a⟩-directions) and the approximate ⟨c⟩-direction are indicated by the arrows. The negative beam direction was approximately* $[1\bar{1}00]$*. Adapted from* [67]*. Republished with permission from Elsevier. (b) Schematic showing the alignment of ⟨a⟩-loops on planes close to* $\{10\bar{1}0\}$ *in a Zr alloy and how the loops are imaged in the TEM. Republished with permission from Elsevier,* [70]*. The schematic in (b) is not drawn from the micrograph in (a), and therefore the loop size, the distance between loops, and the beam direction in (b) do not correspond to those in (a).*

⟨c⟩-component loops have Burgers vector with a component in the ⟨c⟩-direction (with or without additional components in the ⟨a⟩-directions), and for the ⟨c⟩-component loops observed in neutron-irradiated Zr and Zr alloys $\mathbf{b} = 1/6\langle 20\bar{2}3\rangle$ [66,71]. Only vacancy-type ⟨c⟩-component loops have been observed, and they have been reported to be faulted and inhabit the basal plane [66,71]. ⟨c⟩-component loops have been observed only after irradiation to relatively high neutron fluence, in Zircaloy-2 after approximately $3 \times 10^{25}$ n $m^{-2}$. Often, ⟨c⟩-component loops can be observed close to dissolving SPPs. The size of ⟨c⟩-component loops observed with TEM is approximately 100–1000 nm [21,66]. The exact mechanisms of formation of ⟨c⟩-component loops are not understood. Alignment of ⟨a⟩-loops has been suggested to be involved in the formation of ⟨c⟩-component loops, and an anticorrelation of ⟨a⟩-loop and ⟨c⟩-component loop line density has been observed with TEM [21]. The atomistic mechanisms of ⟨c⟩-component loop formation have been modelled in a number of studies, and from the results it seems that ⟨a⟩-loops [72,73] or stacking fault pyramids [74] are involved in the formation. A schematic showing an ⟨a⟩-loop and a ⟨c⟩-component loop in relation to the hexagonal lattice is shown in Figure 4.5, and an APT reconstruction showing segregation of Fe to a presumed ⟨c⟩-component loop surrounded by clusters of Fe and Cr at expected positions of ⟨a⟩-loops is shown in Figure 4.6.

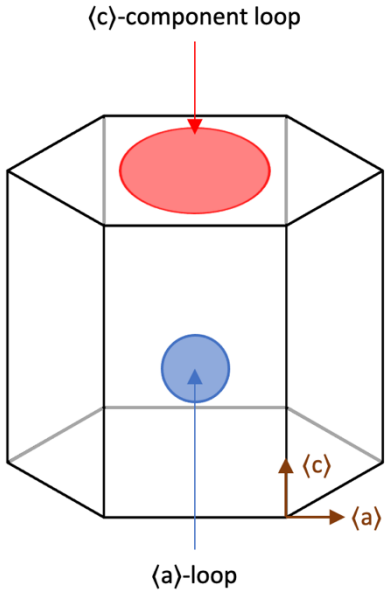


*Figure 4.5: Schematic of the orientation of ⟨a⟩-loops and ⟨c⟩-component loops in relation to the hexagonal lattice. The ⟨a⟩-loop in the schematic is located on a first-order prismatic plane, and the ⟨c⟩-component loop is located on the basal plane.*

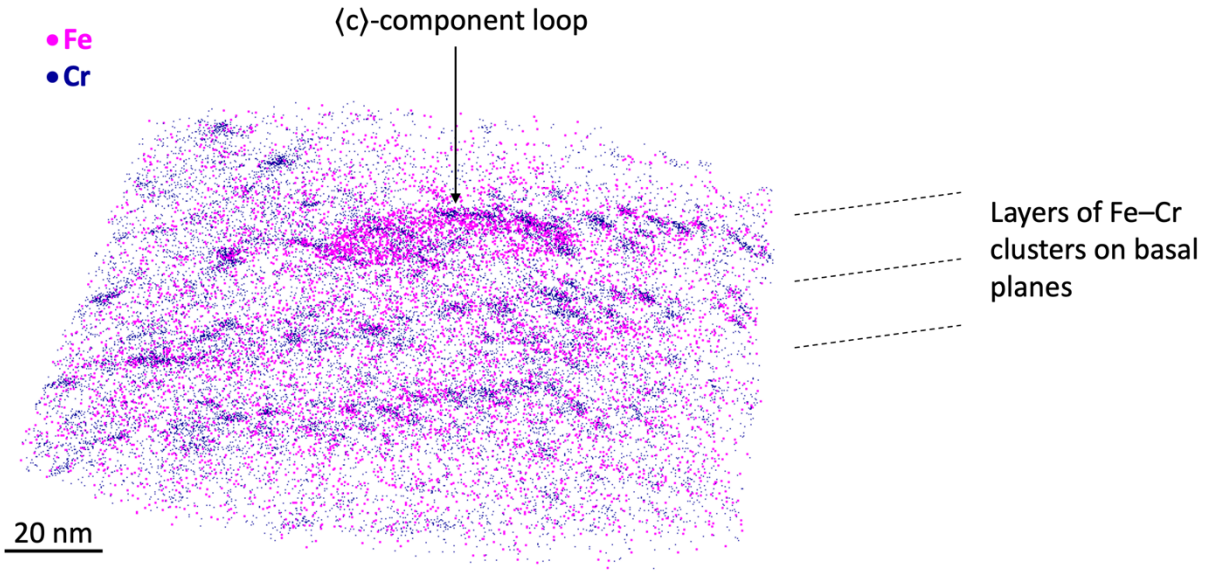


*Figure 4.6: APT reconstruction of Zircaloy-2 exposed to BWR operation, showing a presumed ⟨c⟩-component loop decorated with Fe and surrounded by clusters of Fe and Cr that probably are located at ⟨a⟩-loops.*

## 4.2 Irradiation growth and irradiation creep

Zr alloys exposed to neutron irradiation undergo irradiation growth, which means that dimensional changes of unstressed material occur while the volume is unchanged [58]. The matrix expands in the ⟨a⟩-directions and contracts in the ⟨c⟩-direction [58]. Since the texture of nuclear fuel cladding tubes is such that one of the $\langle 10\bar{1}0\rangle$ or $\langle 11\bar{2}0\rangle$ directions is in or close to the axial direction and the ⟨c⟩-direction approximately 30° from the radial direction [57], the tube expands in the axial direction and contracts in the radial direction. Irradiation temperature, neutron fluence, amount of cold-work, texture, and material composition have all been observed to affect the growth of Zr alloys [4]. RXA material initially has a high growth rate for a short dose range, followed by a slow growth rate over a long dose range until a breakaway growth phenomenon occurs, meaning that the growth rate increases drastically [4]. Breakaway growth has been reported to coincide with the appearance of ⟨c⟩-component loops [75]. SRA material has a high growth rate from the onset of irradiation, comparable to that of breakaway growth in RXA material [4]. This is most probably due to the existence of ⟨c⟩-component loops in the as-produced SRA material [4]. The influence of alloying and impurity elements is not clear. Nb has been observed to delay the onset of ⟨c⟩-component loop formation, thereby delaying the onset of breakaway growth [4]. Increased Fe content seems to lead to decreased growth for some alloys [4,23,76]. Impurity levels of C should be kept below the solubility limit to minimise growth [4]. Also H picked up during operation can lead to increased growth [4,76].

The DAD model for vacancies and interstitials is able to explain the correlation between breakaway growth and the appearance of ⟨c⟩-component loops [60]. Also the more recent modelling not relying on DAD is capable of explaining this correlation [63,77,78].

Irradiation creep is deformation under irradiation in the presence of an external stress [58]. The total strain in the material can be taken as the sum of the creep strain and the growth strain (with the creep strain being due to both irradiation creep and thermal creep) [58]. In Zr alloys the irradiation creep strain rate has been observed to vary with stress, irradiation temperature, neutron flux, amount of cold-work, dislocation density, content of alloying elements in solid solution, and grain size [4]. Creep seems under conditions of normal commercial reactor operation to be dominated by diffusion, but under some conditions, e.g. at low fluence and flux, dislocation slip can be the major contributor to creep [4]. The mechanisms behind growth and creep are connected, and it is thus generally not possible to separate growth from creep.

Irradiation growth and irradiation creep can lead to bowing of cladding tubes and channel boxes. This might lead to deteriorated flow conditions for the water in the core, problems with inserting control rods or control blades, and problems when handling fuel assemblies after operation [79]. Bowing occurs after the onset of breakaway growth [4]. As bowing is highly undesirable, reactors are operated in such a way that it is avoided.

### 4.3 SPP dissolution and alloying element redistribution

Under irradiation at temperatures of LWRs, $Zr(Fe,Cr)_2$ SPPs undergo transition from crystalline to amorphous. An amorphous rim forms at the periphery of the particles and progresses inward toward the centre [29]. On the contrary, amorphous $Zr_2(Fe,Ni)$ SPPs have not been observed after irradiation at temperatures of LWRs [29]. After in-reactor exposure, preferential dissolution of Fe from the $Zr(Fe,Cr)_2$ SPPs has been observed. This has been evidenced by a decrease in the Fe/Cr ratio in the SPPs already after exposure to low fluence [16,22,80]. At fluences where there is a marked decrease in the Fe/Cr ratio in $Zr(Fe,Cr)_2$ SPPs, observations of no change in Fe/Ni ratio in the $Zr_2(Fe,Ni)$ SPPs have been made, indicating simultaneous dissolution of Fe and Ni [22,80,81]. After exposure to high fluence, however, Fe has been observed to be preferentially dissolved also from the $Zr_2(Fe,Ni)$ SPPs [22,80,82]. A large fraction of the SPPs are dissolved during reactor operation, leading to a decrease in their number density [80]. Furthermore, the average SPP size has been observed to increase during reactor operation due to complete dissolution of small SPPs [80]. The $Zr_2(Fe,Ni)$ SPPs are larger and dissolve later in life than the $Zr(Fe,Cr)_2$ SPPs, meaning that there is, relatively, a higher number of Ni-containing SPPs after exposure.

The Fe, Cr, and Ni atoms that have been dissolved from the SPPs during reactor operation have been observed to cluster at positions of ⟨a⟩-loops and segregate to ⟨c⟩-component loops [18,21,22,83,84]. The observed clusters contain mainly Fe and Cr or

Fe and Ni, but usually not Cr together with Ni [18,21,83]. Observations of clusters of Sn in regions where clusters of Fe, Cr, and Ni are virtually absent and segregation of Sn to features interpreted to be ⟨c⟩-component loops have been made with APT [18]. With TEM, Sn enrichment has been observed between layers of clusters of Fe and Cr and clusters of Fe and Ni at ⟨a⟩-loop dislocations [21]. Also, segregation of Sn, Fe, and Cr to grain boundaries has been observed with APT [18,83,84], and with TEM Sn, Fe, and Ni have been observed at grain boundaries [85]. Overall, there are large grain-to-grain variations in the chemistry of irradiated Zircaloys [18,24,83–86].

## 4.4 Pellet–cladding interaction

The main reference for this section is [87]. Additional references are stated in the text.

Pellet–cladding interaction (PCI) is interaction between the inside of the Zr alloy cladding and the fuel pellets. Sometimes the term pellet–cladding mechanical interaction (PCMI) is used when mechanical interaction specifically is referred to. The generation of thermal energy and the release of gaseous fission products inside the pellets during reactor operation lead to swelling and a change in shape of the pellets to an hourglass-like structure. Cracking of the pellets accompanies this change in shape. The cladding experiences creep due to the radiation and the pressure from the coolant water, and contact between the cladding and the pellets results. This means that the initial gap between the pellets and the cladding is closed. Usually, contact between cladding and pellet occurs after about a year of operation in PWRs and after about two years in BWRs.

PCI can lead to cladding failure, especially in combination with stress corrosion cracking induced by corrosive fission products, of which iodine is considered to be the most prominent, and caesium and cadmium are considered to be possible contributors. Since the swelling of the fuel increases with increasing maximum power and the rate at which the power is changed, reactors are operated in such a way that PCI is avoided. Cladding failure due to PCI has not been much of a problem in PWRs but has historically been so in BWRs. To mitigate this problem, modern BWR claddings (since the 1980s) are manufactured with a Zr liner (making up about 10 % of the total wall thickness [88]) on the inside of the tubes. The liner is softer than the outer part of the cladding and has a different chemical composition. It is thus more resistant to cracking initiated by PCI. The bonding between the liner and the outer part of the cladding is metallurgic [88]. Low concentrations of alloying additions, e.g. Sn and Fe, are generally used in modern liners to increase the corrosion resistance in case the cladding is penetrated so that water can reach the inside of the tubes [36]. If a pure Zr liner is used, the risk of severe secondary degradation that leads to relatively large amounts of radioactive substances being released to the coolant is increased [36].

# 5. Corrosion of Zr alloys

Corrosion degrades the Zr alloys during reactor operation. In this chapter, corrosion in autoclave and in reactor is described, and the effects of SPPs, alloying elements, and impurities are emphasised. The main reference for this chapter is [89]. Additional references are stated in the text.

## 5.1 General corrosion phenomena in autoclave and in reactor

Corrosion of the fuel cladding is highly affected by the environment in the reactor. Minimising the corrosion and the HPU resulting from corrosion is the reason for utilising different types of Zr alloys in different types of reactors. On the outside of the oxide, a layer of crud, i.e. deposition of corrosion products from materials (e.g. stainless steel and Ni-base alloys) in the surroundings, is formed. If the oxide or crud layer gets too thick, the temperature of the cladding will increase, leading to an increase in the corrosion rate, leading to a further increase in oxide thickness. Such a positive feedback can result in both deteriorated mechanical properties and through-wall corrosion of the cladding tubes. The lower the corrosion rate, the higher the burnup of the fuel that is possible to achieve while still keeping a sufficient margin to cladding failure due to corrosion.

The oxide formed in the corrosion process is $ZrO_2$, zirconia. It exists (in addition to a high-pressure orthorhombic phase) in the three polymorphic forms monoclinic, tetragonal, and cubic [90], whereof the two first are relevant for conditions of reactor operation. The overall reaction for formation of $ZrO_2$ in water is

$$Zr\ (s) + 2H_2O\ (l) \rightarrow ZrO_2\ (s) + 2H_2\ (g).$$

Since the diffusion of O is faster than the diffusion of Zr through zirconia, the oxide is inward growing, meaning that the formation of zirconia takes place at the metal/oxide interface. The transport path of O is nowadays considered to be via grain boundaries in the oxide [91], in contrast to a previously assumed vacancy-mediated mechanism [29]. As the Pilling–Bedworth ratio, the ratio of the volume of the oxide to the volume of the metal, is 1.56 for Zr, there is a volume expansion during growth of the oxide. Usually, the oxide growth is measured as oxide thickness or as weight gain.

Based on autoclave corrosion, the corrosion can be described according to the following. In the initial stage of oxidation, the oxide thickness, $d$, is considered to be proportional to the oxidation time, $t$, raised to the power of $n$,

$$d \propto t^n,$$

where $n$ typically is around 1/3 [92].

At this stage of oxidation, the oxide is black (because of localised surface plasmon resonances in SPPs in the oxide [93]), protective, and consisting of small equiaxed grains. Columnar grains form and start to grow with their long axis perpendicular to the metal/oxide interface. Eventually, a transition occurs when the columnar grains become unstable (at a height of approximately 2 μm) due to compressive stresses, and small equiaxed grains start to grow at the metal/oxide interface. Below this layer, a new layer of columnar grains of zirconia starts to grow, and the corrosion process continues according to this cyclic behaviour, forming a structure with alternating layers of equiaxed and columnar grains [92,94]. The time between these cyclic transitions becomes increasingly shorter, and eventually a linear oxide growth rate can be observed. The three growth regimes are referred to as pre-transition (cubic), transition or transitory, and post-transition (linear). Although the pattern is cyclic in the transitory regime, the corrosion kinetics after the first transition is sometimes approximated by a linear relationship between oxide growth and corrosion time. (The cyclic pattern was not recognised in early corrosion models [95].) The corrosion rate of different alloys is related to the length of the transition cycles, with shorter cycles for faster-corroding alloys. Longer cycles are related to a thicker and denser innermost oxide layer, termed barrier oxide layer, that offers a more difficult transport path for oxygen ions toward the metal/oxide interface. A higher fraction of columnar grains in the barrier layer is beneficial for the corrosion properties. The thickness of the barrier layer has been observed not to be the same as the thickness of the pre-transition oxide or the average thickness of the oxide of the transitory cycles. The oxide outside the barrier layer is associated with more cracks and porosities. The growth regimes (based on autoclave corrosion) are schematically shown in Figure 5.1.

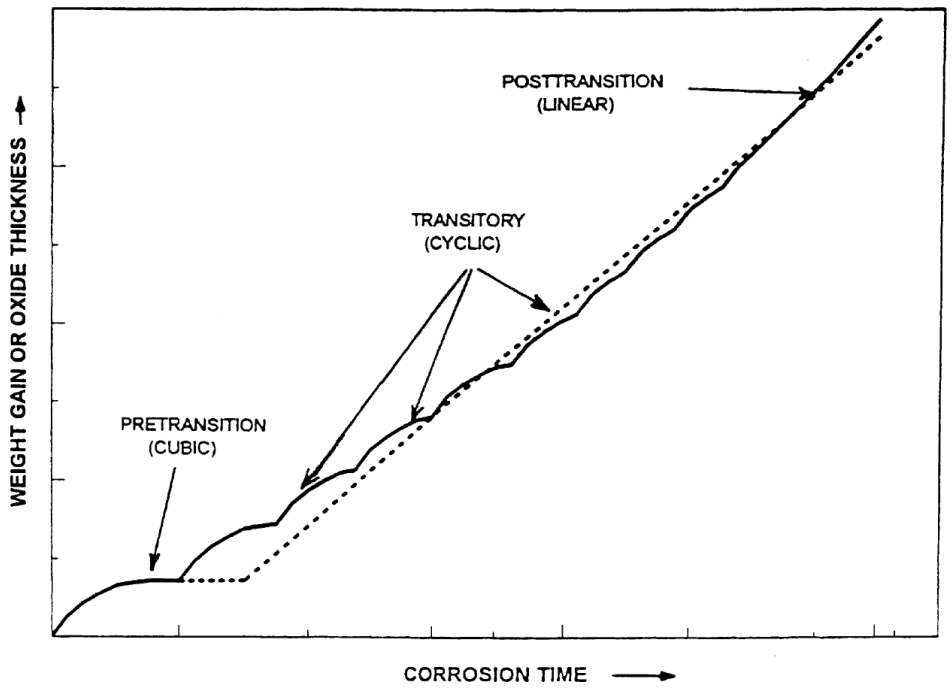


*Figure 5.1: The three growth regimes during autoclave corrosion of Zircaloy-type alloys. The dashed lines indicate earlier models that did not recognise the transitory regime. Republished with permission from Elsevier,* [95].

In autoclave-corroded Zircaloys, a substoichiometric oxide layer of a few tens of nm with a composition close to ZrO forms at the metal/oxide interface and is followed by an O diffusion profile into the metal, extending up to some hundreds of nm, starting with saturated metal with about 30 at.% O and ending with the O concentration of the metal matrix [96–98]. The metal/oxide interface is undulated and has in Zircaloy-2 after autoclave corrosion been reported to have a periodicity of approximately 1 μm with an amplitude of 100 nm [97]. Lateral cracks in the oxide have been observed to appear with a periodicity corresponding to the thickness of the layers of cyclic transition between equiaxed and columnar grains [94]. A proposed mechanism for the formation of this type of lateral cracks is that tensile stresses that form in the oxide above metal wave crests of the undulating metal/oxide interface and above SPPs due to the volume expansion during oxide growth lead to cracking at these locations [99]. The existence of lateral cracks in the oxide has been suggested to increase corrosion by facilitating inward transport of oxygen ions through the oxide [94,99]. An additional observation is that the growth of the oxide leads to the formation of subgrains in the metal close to the metal/oxide interface [100]. Figure 5.2 shows the metal/oxide interface and subgrains in the metal of autoclave-corroded Zircaloy-2.

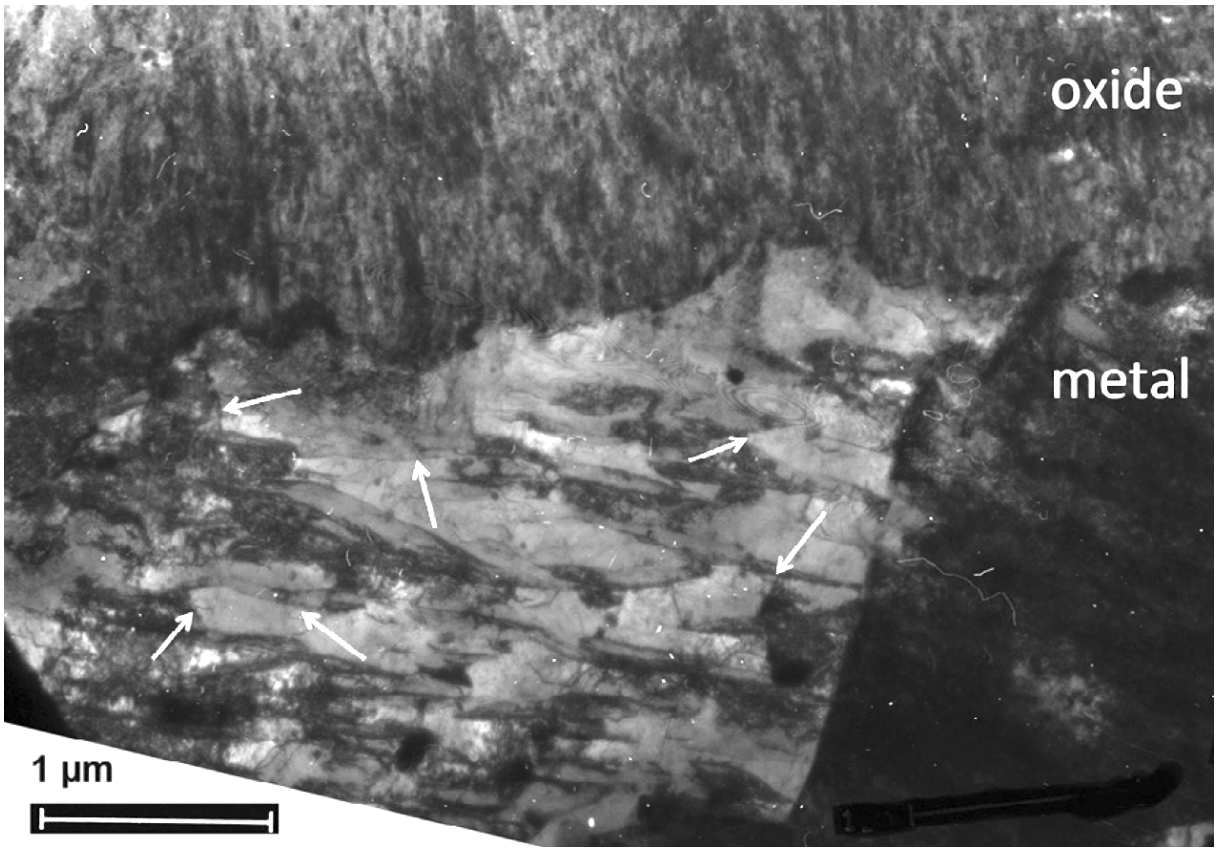


*Figure 5.2: TEM micrograph of the metal/oxide interface in autoclave-corroded Zircaloy-2. Arrows indicate subgrain boundaries in the metal. Republished with permission from Elsevier,* [100].

In reactor, the corrosion rate is usually enhanced compared with in autoclave. This has for Zircaloy-2 been linked to the observation of a more heterogeneous oxide microstructure with weaker texture and more cracks compared with autoclave-corroded samples [24,101]. The number of cracks has been observed to increase with increasing exposure, and at the metal/oxide interface the cracks in the oxide have been observed to be located at or close to hydride phases in the metal [24,102,103]. Also after in-reactor exposure, the cyclic pattern of cracks in the oxide has been observed [94]. The enhanced diffusion resulting from interaction between fast neutrons and the oxide seems not to affect the corrosion rate, but dissolution of alloying elements from SPPs due to radiation seems to have a large impact on corrosion [92].

If the environment is oxidising, as in BWRs, a phenomenon called shadow corrosion can occur when Zr alloys are in direct contact with or close to other metals and alloys. A difference in corrosion potential between Zr and the other material can lead to galvanic corrosion, resulting in increased oxide thickness at the affected Zr surface. Shadow corrosion has generally not led to fuel performance problems [89], but there is at least one example where enhanced shadow corrosion at spacer grids has done so [104]. Enhanced spacer shadow corrosion can occur when a cladding material with a small SPP size is used in a reactor with a low Fe/(Zn + Ni) ratio in the coolant [36]. (Zn is injected in some BWRs to reduce dose levels to the personnel by inhibiting release of radioactive corrosion products, mainly $^{60}$Co [105]) To avoid the problem of enhanced spacer shadow corrosion, the SPP size has been optimised [36].

## 5.2 Effects of SPPs, alloying elements, and impurities

The influence of SPPs and alloying elements on corrosion is not well understood. Some of the observations reported in the literature are summarised in this section.

In BWRs, nodular corrosion, i.e. corrosion localised to spots on the cladding tubes, has been a problem. It occurs in oxidising environments when the SPP size is large. By decreasing the average SPP size, the issue with nodular corrosion in BWRs has been resolved. In PWRs, where nodular corrosion has not been a problem, the SPP size has not been decreased, since smaller SPP size leads to an increase in uniform corrosion rate. Due to the dissolution of SPPs, a too small SPP size is a problem also in BWRs. If the burnup of the fuel is to be increased, the increased neutron fluence exposure of the cladding will lead to more SPP dissolution, requiring a large SPP size to get good uniform corrosion properties during the whole operating life of the cladding. An optimisation of the SPP size is thus necessary to get both a low uniform corrosion rate and a low risk of nodular corrosion.

In autoclave corrosion, SPPs are known to be incorporated in unoxidised state into the oxide, both in unirradiated Zircaloy-4 and in Zircaloy-4 pre-irradiated with ions [106]. After being incorporated into the oxide, amorphisation of $Zr(Fe,Cr)_2$ SPPs and preferential dissolution of Fe have been observed in the absence of irradiation. This effect of oxidation on SPP dissolution is similar to the effect of irradiation. In autoclave-

tested Zircaloy-2, observations of enrichment of Fe and Ni at subgrain boundaries have been made close to the metal/oxide interface, in both the metal and the oxide [107], and after in-reactor exposure Fe and Ni have been observed at features that appear to be oxide grain boundaries [85].

In BWRs, Zircaloy-2-type alloys are the alloys that have the best corrosion performance. In PWRs, however, Nb-containing alloys have lower corrosion rate than the Zircaloys [108,109].

Sn, which is added mainly to improve the mechanical properties of Zr alloys, is in BWRs beneficial also for the corrosion resistance. Especially the nodular corrosion is decreased by the presence of Sn. In PWRs, however, decreased Sn content has been shown to improve the corrosion performance, and therefore newly developed alloys for PWRs often contain less Sn than the older alloys [108]. It is known that Sn is a stabiliser of tetragonal zirconia [110], and clusters and precipitates of Sn have been observed in the oxide of autoclave-corroded Zircaloy-2 [111].

Of the impurities in Zr alloys, N is the element that has the most detrimental effects on corrosion, both in autoclave and in rector. Si has been observed to decrease the corrosion in reactor, whereas it in autoclave decreases the corrosion rate in concentrations below 120 (wt) ppm and increases the corrosion rate in concentrations above 120 ppm. C has been observed to increase corrosion in autoclave in the concentration range 100–300 ppm, to increase corrosion in PWR, and not to affect corrosion in BWR. Al has in autoclave been observed not to affect corrosion in concentrations up to 80 ppm and to increase corrosion in concentrations between 80 and 400 ppm.

# 6. H pickup and hydride phases in Zr alloys

HPU is a lifetime-limiting process in Zr alloys. As in the case of corrosion, the HPU varies significantly between different reactor types and different alloys. This chapter describes the origin of the H picked up, the influence of alloying elements on HPU, the solubility of H in Zr, and the Zr hydride phases.

In the overall corrosion reaction described in Section 5.1, the $H_2$ gas formed in the splitting of the water molecules can be formed via positive H ions, $H^+$, and H radicals, $H^\bullet$ [89]. In addition to this, radiolytic dissociation of water molecules occurs, also producing $H^+$ and $H^\bullet$ [26]. It has been proposed that, when not recombining to form $H_2$, the $H^\bullet$ species formed at the oxide/water interface can be transported through the oxide via hydroxylated grain boundaries and reach the metal [112]. The $H_2$ gas dissolved in the reactor coolant is thus not the hydrogen picked up by the Zr alloys. The hydrogen pickup fraction (HPUF) is used to quantify the HPU and is the amount of H picked up by the metal to the amount of H generated in the corrosion process.

HPU in binary Zr alloys has been studied out of reactor in [6]. From these results it seems that, compared with pure Zr, Sn has no impact on HPU, Fe and Cr decrease HPU, and Ni increases HPU. This can be seen in the commercial alloys, where the HPU in Zircaloy-2 is higher than in Ni-free alloys [89]. In BWRs, accelerated HPU in Zircaloy-2 is observed after relatively long exposure time. This acceleration in HPU and HPUF is believed to be related to the dissolution of $Zr_2$(Fe,Ni) SPPs and is followed by breakaway corrosion [81,89]. In Nb-containing Zr alloys, the HPU is relatively low [109,113]. The relatively lower HPUF of Nb-containing alloys compared with the Zircaloys has been suggested to be due to the presence of $Nb^{5+}$ in the oxide, which might lead to proton reduction at the oxide/water interface instead of at the metal/oxide interface [109].

When incorporated in the metal matrix, H atoms can occupy the tetrahedral and octahedral interstitial sites in the Zr lattice. According to DFT calculations, tetrahedral sites are preferred, with about 6 % of the H atoms located at octahedral sites at temperatures of reactor operation [114]. When the solubility limit is exceeded, hydride precipitation occurs [115]. The terminal solid solubility for precipitation differs from that for dissolution, and they are often denoted TSSP and TSSD, respectively. Results of measurements performed on Zircaloy-2 using differential scanning calorimetry [116], which correlate well with results obtained by other techniques [115], have yielded the following equations for TSSP and TSSD (for both unirradiated and irradiated material):

$$C_{TSSD} = 1.43 \times 10^5 e^{(-36\,686/(RT))}, \qquad (6.1)$$
$$C_{TSSP} = 3.27 \times 10^4 e^{(-25\,042/(RT))}, \qquad (6.2)$$

where $C$ is the H concentration in (wt) ppm, $e$ is Euler's number, $R = 8.314$ $Jmol^{-1}K^{-1}$ is the ideal gas constant, and $T$ is the temperature in K. This gives approximate terminal solid solubilities of 91 and 220 ppm at 600 K and of 0.059 and 1.4 ppm at 300 K for

TSSD and TSSP, respectively. The solubility of H is thus much higher at temperatures of reactor operation, and therefore there are more hydrides in the cladding tubes post service. Irradiation effects have been observed to lead to increased H solubility, both experimentally [117,118] and by modelling [114]. Modelling also indicates that Fe, Cr, and Ni increase the H solubility, that O, Sn, and Nb do not affect the H solubility, and that all alloying elements destabilise hydride phases, meaning that hydride phases probably are less likely to form where the alloying elements are present [119].

There are four known hydride phases in Zr with the following names and approximate stoichiometries: ζ — $ZrH_{0.5}$, γ — ZrH, δ — $ZrH_{1.5\text{-}1.7}$, ε — $ZrH_2$ [115]. δ and ε are stable phases, ζ is metastable, and γ is probably a metastable phase that is stable only under certain conditions [115]. The crystallography of the hydride phases differs from the crystallography of the Zr matrix. However, the atomic positions of Zr are not very different in the hydride phases compared with α-Zr [114,120,121]. The crystal structures of the phases are trigonal for ζ (which is fully coherent with α-Zr with a twice as large lattice parameter in the ⟨c⟩-direction [122]), face-centred tetragonal (FCT) for γ, face-centred cubic (FCC) for δ, and FCT for ε [115]. The {111} planes for the FCC and FCT phases correspond to the (0002) planes of the hexagonal α-Zr phase. Both γ- and δ-hydrides have been observed to exist as plate-like structures in the Zr matrix. The habit plane, which corresponds to the broad side of the plate, has for both γ and δ been observed to be parallel to $\{10\bar{1}0\}$ and $\{10\bar{1}7\}$ [115]. For δ a number of other habit planes also have been observed [115]. The growth direction of hydrides in the absence of external stresses is $\langle 11\bar{2}0\rangle$, and in the presence of external stresses, the growth direction is perpendicular to tensile stresses and parallel with compressive stresses [115]. Intergranular hydrides with their habit plane parallel with grain boundaries often form [115]. A Zr–H phase diagram is shown in Figure 6.1, the lattice parameters for the hydride phases and α-Zr are shown in Table 6.1, and unit cells for γ-, δ-, and ε-hydrides are shown in Figure 6.2.

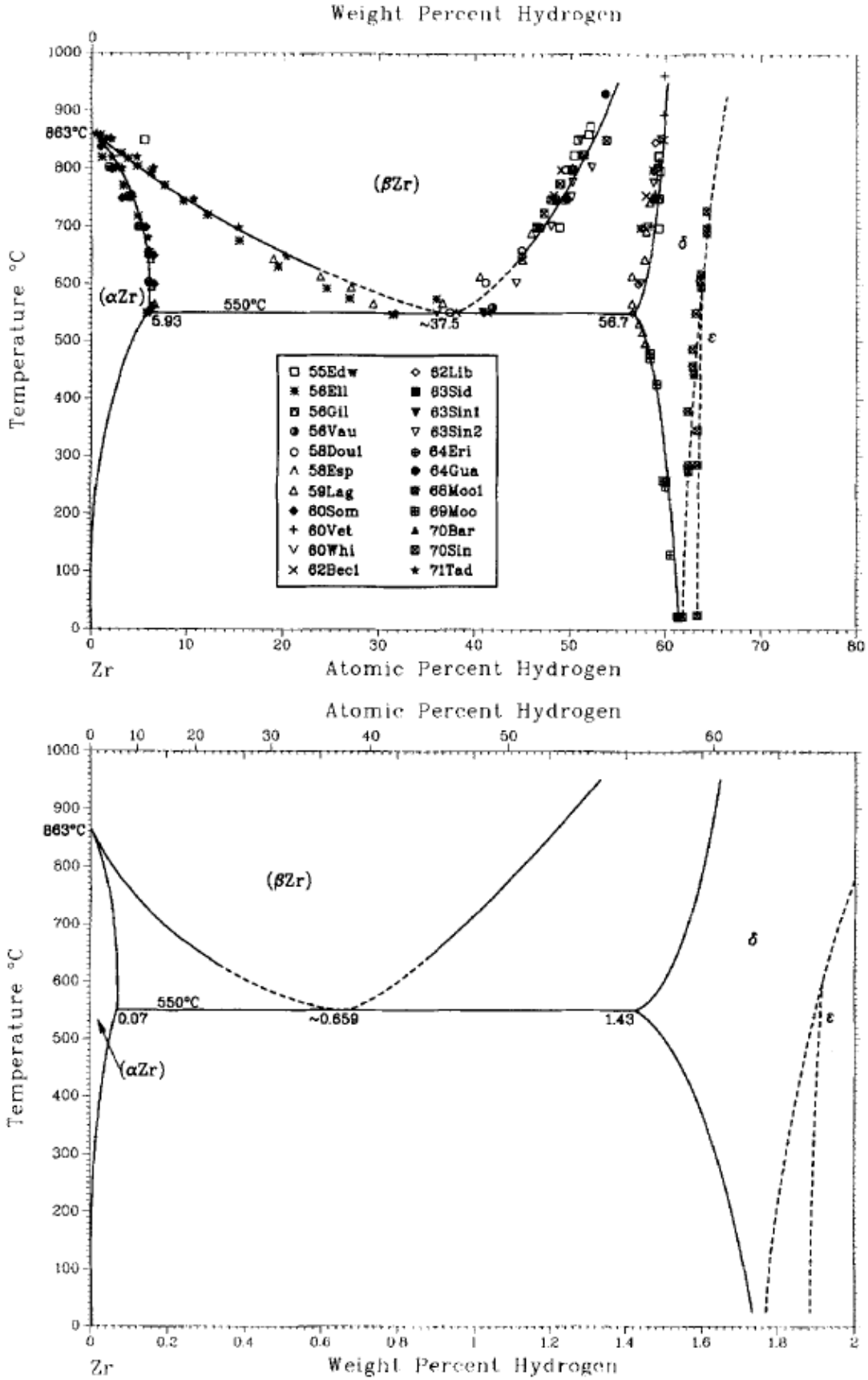


Figure 6.1: A Zr–H phase diagram. Top: with experimental data. Bottom: without experimental data. Republished with permission from Springer Nature, [123].

*Table 6.1: Lattice parameters of α-Zr and the hydride phases in Zr.*

| Phase | Crystal structure | *a* (nm) | *c* (nm) |
|---|---|---|---|
| **α-Zr**[1] | Hexagonal | 0.323 | 0.515 |
| ζ[2] | Trigonal | 0.33 | 1.029 |
| γ[3] | FCT | 4.586 | 4.948 |
| δ[4] | FCC | 4.771 | - |
| ε[5] | FCT | 4.975 | 4.447 |

[1]Values from [124].
[2]Values from [122].
[3]Values from [125].
[4]Value from [126].
[5]Values from [127].

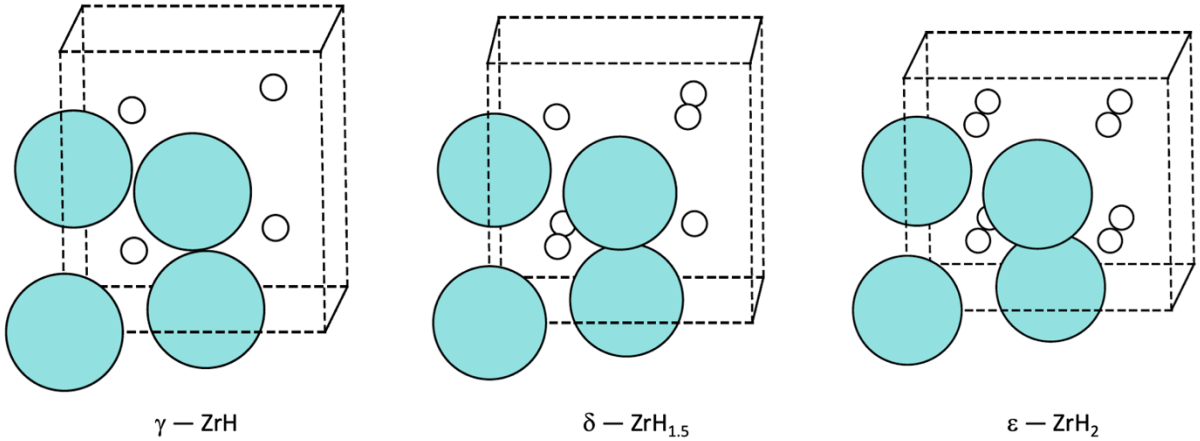


*Figure 6.2: Unit cells for γ-, δ-, and ε-hydrides. Adapted from* [120]. *Republished with permission from Springer Nature.*

Since the diffusivity of H in α-Zr is high, the hydrides may be located far from where the H entered the metal [89]. The location and orientation of hydrides are highly dependent on the stresses in the metal [29]. The crystallographic texture of the cladding tubes determines the stress orientation, thus affecting the hydride orientation [29]. Tangential orientation of hydrides is beneficial for the mechanical properties of the cladding, whereas radial orientation leads to embrittlement and increased risk of delayed hydride cracking (DHC) [115]. Post service, when the cladding tubes are moved from wet storage to dry storage, the temperature in the cladding initially increases and subsequently decreases again. Many of the hydride phases are then initially dissolved followed by reprecipitation at the lower temperature. The hydride phases are thereby reoriented. This might lead to an increased risk of cladding failure if a larger amount of radial hydrides is precipitated. The phases that cause most cladding failures and, therefore, have been studied most are δ and γ [115]. Also during sample preparation, e.g. for microscopy studies, the atomic configuration of H might be rearranged and hydride phases formed or dissolved [67,80,128,129].

# 7. Experimental techniques

The main experimental technique used in the work of this thesis is APT. This chapter describes the basic principles of this technique and methods of data evaluation along with normal procedures of specimen preparation. The main references for this chapter are [130–132]. Additional references are stated in the text. TEM has been used to some extent in the work presented in Paper VI. A description of TEM can be found in [133].

## 7.1 Atom probe tomography

This section is divided into four subsections. The first gives an overview of APT, the second describes the procedures for specimen reconstruction and data evaluation, the third describes some limitations and common artefacts associated with APT, and the fourth describes APT of Zr alloys.

### 7.1.1 Overview

APT is a destructive analysis technique that can give chemical information with spatial resolution at the near-atomic scale. The specimen to be studied is needle-shaped with a tip diameter of some tens of nanometres and is subjected to a direct-current (DC) positive voltage. Due to the small radius of the tip, the electric field at the surface is very high, several tens of V/nm. When subjected to a sufficiently high field, ionised atoms or molecules at the tip surface are emitted from the specimen, a process called field evaporation (although it rather is a transformation from solid state to plasma). As the evaporation probability depends on electric field strength and temperature, it is possible to achieve field evaporation by pulsing with either an additional electric field (voltage pulse mode) or a laser beam that heats the specimen (laser pulse mode). The evaporation field and the two pulsing modes are schematically shown in Figure 7.1. The penetration depth of the field is very small, and therefore only ions at the surface are evaporated. After being evaporated, the ions are accelerated by the electric field toward a position-sensitive and time-resolved detector, where a highly magnified image of the tip is created. The magnification is roughly $L/R$, where $L$ is the flight path length and $R$ the tip radius, and is typically in the order of $10^6$.

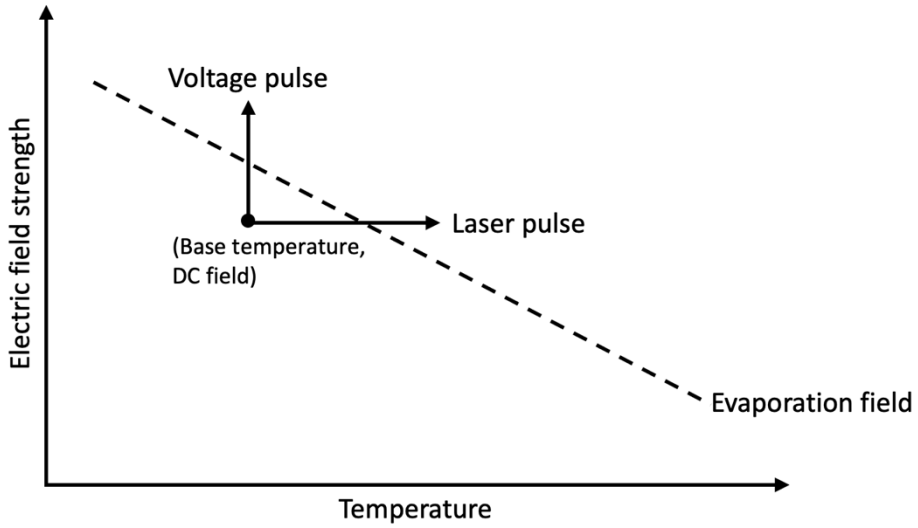


*Figure 7.1: Schematic of evaporation field and voltage pulsing and laser pulsing.*

The time of flight, $t$, for each ion depends on its mass-to-charge ratio, $m/z$, according to

$$m/z = 2eVt^2/L^2, \qquad (7.1)$$

where $e$ is the elementary charge, $V$ the combined voltage of the DC electric field and the pulse, and $L$ the flight path length. This equation can be derived by setting the kinetic energy, $mL^2/(2t^2)$, of the ion at the detector equal to its potential energy, $zeV$, at the specimen surface. From Equation (7.1) it is evident that the time of flight increases with increasing mass-to-charge ratio. The time of flight is measured as the time between the voltage or laser pulse and the event of the ion hitting the detector. From this time of flight, a mass spectrum, showing the mass-to-charge ratio (usually in the unit Da) on one axis and the number of hits on the other, can be created. In this way, chemical information about the specimen is obtained. Since the impact position and the order of events at the position-sensitive detector are stored, it is possible to make a three-dimensional (3D) reconstruction of the specimen. Combining this 3D reconstruction with the chemical information obtained makes it possible to use APT for both spatial and chemical analysis at length scales ranging from atomic interplanar spacings to micrometres.

APT measurements have to be performed under ultra-high vacuum (UHV), typically in the range of $10^{-8}$ Pa. Therefore, all APT instruments are equipped with a UHV system. During analysis, the specimen is usually held at a temperature in the range 20–100 K. Most commonly, a local electrode, i.e. an electrode positioned at a distance on the order of tens of micrometres from the specimen apex and having an aperture through which evaporated ions can pass, is utilised for accelerating the emitted ions toward the detector. The voltage used for the DC electric field is typically several kV, and it increases throughout the analysis as the specimen gets blunter. The pulse frequency is usually in the range 100–500 kHz for both voltage and laser pulsing. A voltage pulse usually extends a few ns in time and a laser pulse usually around 10 ps. Green lasers of wavelength 532 nm and pulse energies of 0.01–1 nJ or ultraviolet (UV) lasers of wavelength 355 nm and pulse energies about a factor 100 lower than those of green lasers are commonly used. (Due to a difference in focus between green lasers and UV lasers, the energy per unit area is not a factor 100 lower for UV lasers.) Instruments having a green laser are decreasing in number, and almost all modern instruments are equipped with a UV laser [134]. The most recent generation of instruments is equipped with what is termed a deep-UV laser of wavelength 266 nm and is capable of performing simultaneous voltage and laser pulsing [135]. If voltage or laser pulsing is most appropriate and what values of the analysis parameters to use depend on the material to be studied and what information is desired.

The flight path to the detector after leaving the local electrode is straight in instruments that are not equipped with a reflectron and curved in instruments that are equipped with a reflectron. A reflectron is a time- and space-focusing device that gives all ions of equal mass-to-charge ratio (almost) equal flight times to the detector by increasing the flight path length for ions of higher energy. This is done by an electrostatic field that deflects the ions entering the reflectron toward the detector. Ions of higher energy travel longer into the reflectron and thus take a longer path to the detector, meaning that their time of flight is increased. Instruments with a reflectron have better mass resolution but slightly decreased spatial resolution compared with instruments without a reflectron. A schematic of local-electrode APT and flight paths with and without reflectron is shown in Figure 7.2.

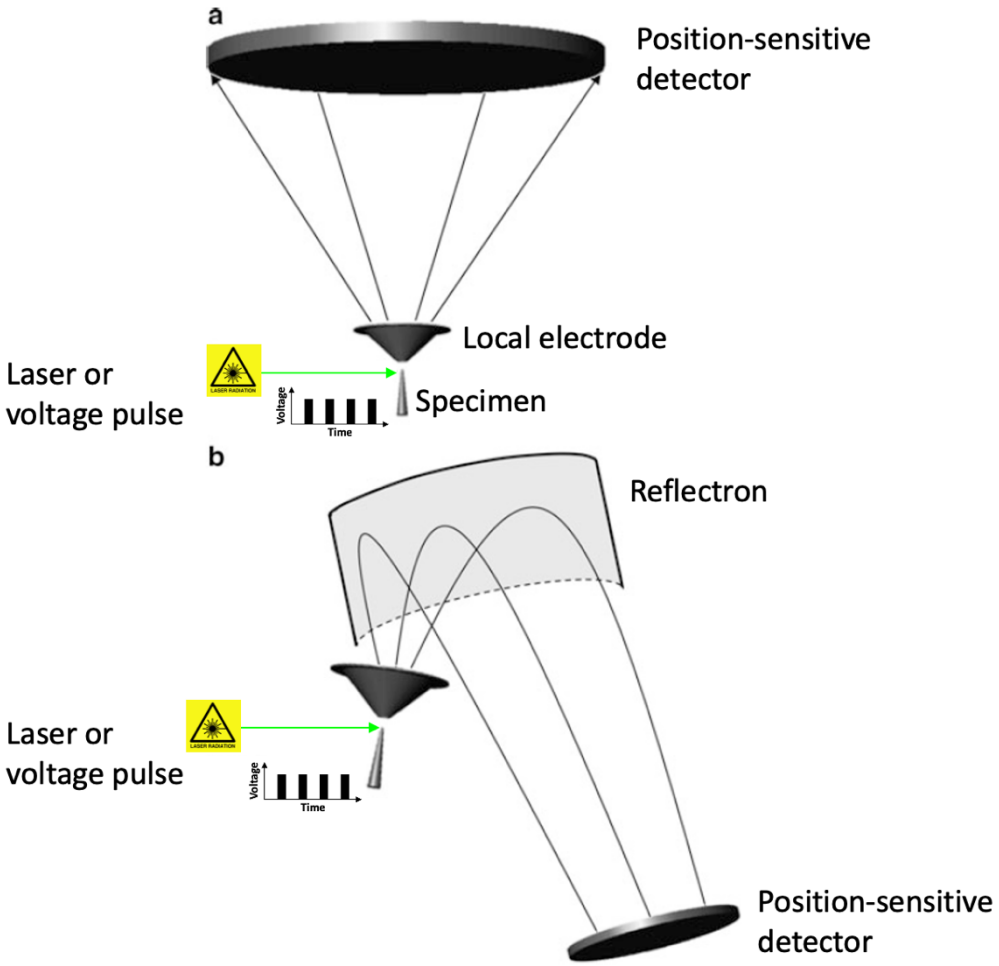


*Figure 7.2: Schematic of APT. (a) Without reflectron. (b) With reflectron. Adapted from* [131]. *Republished with permission from Springer Nature.*

Generally, the detector consists of micro-channel plates (MCPs) coupled to anodes that are in the form of delay lines. MCPs are arrays of tubes of an electron-multiplying material. Thus, when an ion hits the inside of an MCP tube, secondary electrons are generated and multiplied. The multiplied electrons generate electrical pulses in the delay lines, which are two-dimensional (2D) anodes, each consisting of one transmission line bent to a meander-like shape. The pulses travel in opposite directions along the same delay line and are collected at both ends of the line. There are two delay lines oriented perpendicularly to one another, allowing for determination of the impact position of the ion via the difference in time of arrival of the pulse at each end of each line. The time of flight can be estimated from the average of the times of arrival at the four line ends. Additionally, a third delay line, oriented ± 45° from the other two, is usually employed to separate events that are too close in time and space to be separated by the two perpendicular lines.

### 7.1.2 Specimen reconstruction and data evaluation

There are a number of ways to reconstruct the specimen from the experimental raw data. Most of the reconstruction protocols commonly used are based on the Bas protocol [136]. The specimen apex is assumed to be hemispherical, and the evaporation is assumed to be uniform across the projected tip area. Reconstruction is done in the lateral directions for successive layers of evaporated species in the axial tip direction. Four parameters are used, the detection efficiency ($\eta$), the evaporation field ($F_e$), the field factor ($k_f$), and the image compression factor ($\xi$). The electric field, $F$, is related to the radius of curvature, $R$, of the specimen tip, the field factor, and the combined voltage, $V$, of the DC electric field and the pulse according to

$$F = V/(k_f R). \qquad (7.2)$$

During measurement $V$ is adjusted to get a constant detection rate, and $F \approx F_e$.

The image compression factor for straight-flight-path instruments can be expressed as

$$\xi = \theta_{crys}/\theta_{obs}, \qquad (7.3)$$

where $\theta_{crys}$ is the crystallographic angle and $\theta_{obs}$ the observed angle. $\theta_{obs}$ is related to the distance, $D$, between observed crystallographic poles on the ion density map (also referred to as detector hitmap or field evaporation image) obtained during analysis and the flight path length, $L$, according to

$$\theta_{obs} = arctan(D/L). \qquad (7.4)$$

Normally, the image compression factor has a value between 1 and 2, where 1 corresponds to a radial projection and 2 to a stereographic projection.

When the (approximately) hemispherical surface of the tip cuts parallel lattice planes, these take the shape of concentric rings on the surface. The crystallographic poles (which correspond to the crystallographic directions [137]) are the centres of these rings. The local chemical environment of edge atoms at the poles is such that some atoms just before being field evaporated are displaced from the original lattice site, whereas other atoms evaporate at a higher field than the neighbouring atoms [138]. Similar effects occur at the zone lines connecting the poles. Poles and zone lines can appear as regions with variations in density on the detector hitmap. A schematic of angles and distances used in the reconstruction and a hitmap with crystallographic poles and zone lines for a local-electrode atom probe with straight flight path is shown in

Figure 7.3. For instruments having a reflectron, a virtual flight path length, shorter than the real flight path length, can be used to perform the same calculations as for instruments without reflectron.

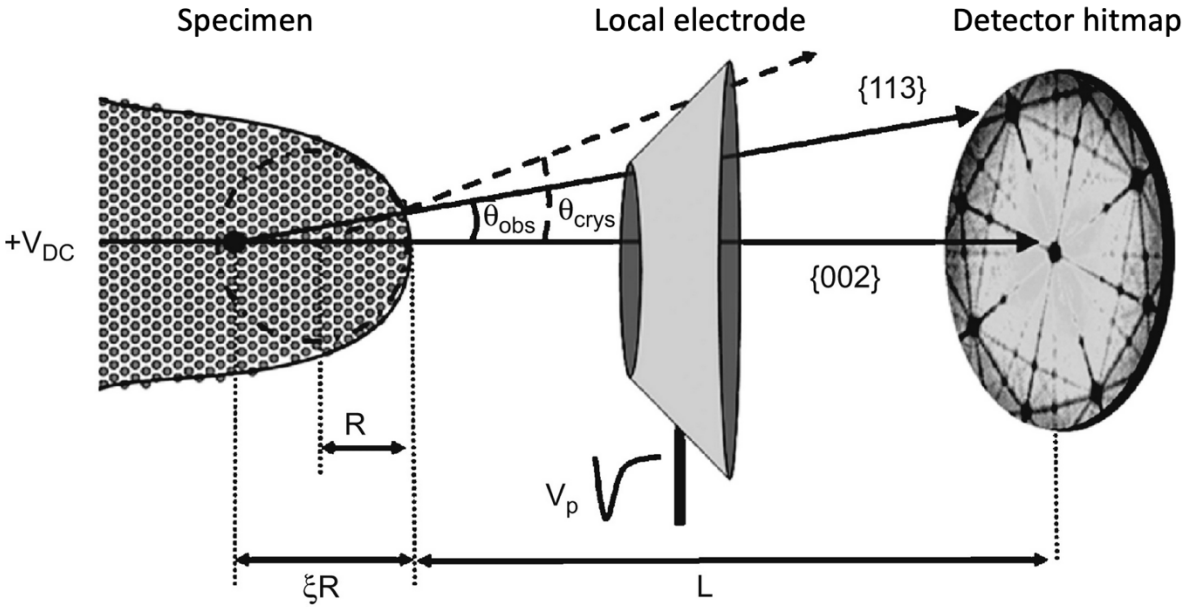


*Figure 7.3: Schematic of angles and distances used in APT reconstruction and a detector hitmap with crystallographic poles and zone lines visible. Adapted from* [139]*. Republished with permission from Elsevier.*

It is usually difficult to calibrate the reconstruction. If crystallographic information is obtained in the analysis, that information might be used for determining appropriate values of $k_f$ and $\xi$. If the poles are visible on the hitmap, they might be identified using the symmetry that appears on the map and, if multiple poles are visible, the distance between them. Also, if there are features within the sample that have a known crystallographic orientation, these can be used for identification of the poles (or for identification of the crystallography if no poles are visible). At the poles, atomic planes are sometimes visible in the reconstruction. Using the atomic spacing of the different sets of planes and the angles between the planes of a known crystal structure, it is possible to iteratively change the values of $k_f$ and $\xi$ to get an appropriate reconstruction. If only one pole with visible atomic planes is observed and identified, it is often possible to get a reconstruction that is appropriate regarding spacing of those planes but that does

not necessarily give an appropriate representation of other crystallographic directions. However, crystallographic information is only occasionally obtained in APT analysis, and calibrations of the reconstruction according to the above are therefore often not possible to perform. To more easily obtain the crystallography of the specimen, it is sometimes possible to study the crystallographic orientations of the grains of the sample prior to lift-out, e.g. by electron backscatter diffraction (EBSD). Moreover, complementary microscopy techniques such as field ion microscopy (FIM), TEM, transmission Kikuchi diffraction (TKD), and EBSD can in some cases be used to obtain information on crystallography or other features in the prepared specimen in order to calibrate the reconstruction or to enable interpretation of results. Alternatively, the specimen can after analysis be viewed using scanning electron microscopy (SEM) or TEM to measure $R$ and thereby obtain a reasonable value of $k_f$ (assuming the evaporation field is known).

When the reconstruction has been performed there are various means to evaluate the data, the choice of which to use depends on what features are present in the specimen and what information about these features that is desired. Often, quantitative information about clusters of solute species is wanted. Multiple ways of obtaining this information exist. The definition of a cluster is not straightforward and can be done more or less arbitrarily. In the definition, clusters might not be distinguished from small precipitates, and from APT data it is in many cases not possible to tell the difference between the two. Various algorithms are used for cluster characterisation, one of the most common being the maximum separation method (MSM) [140,141] (which is very similar to the density-based scanning algorithm (DBSCAN) [142]). In the MSM algorithm, the distance between detected species is used to define clusters. A minimum number, $N_{min}$, of solute species with a separation distance between individual species not exceeding $d_{max}$ form a cluster. Other species within an envelope distance, $L_e$, from the solute species of the cluster can be included in the cluster. A halo of these other species might then form around the cluster. This halo is eroded away by applying an erosion step, removing species that are not the solute atoms of the cluster and that are located within an erosion distance, $d_e$, from species that are located outside of the cluster and are not of the same kind as the solute atoms of the cluster. The order of neighbours (i.e. first-nearest neighbours, second-nearest neighbours, and so forth) for which $d_{max}$ is applied has to be specified. A schematic of MSM is shown in Figure 7.4.

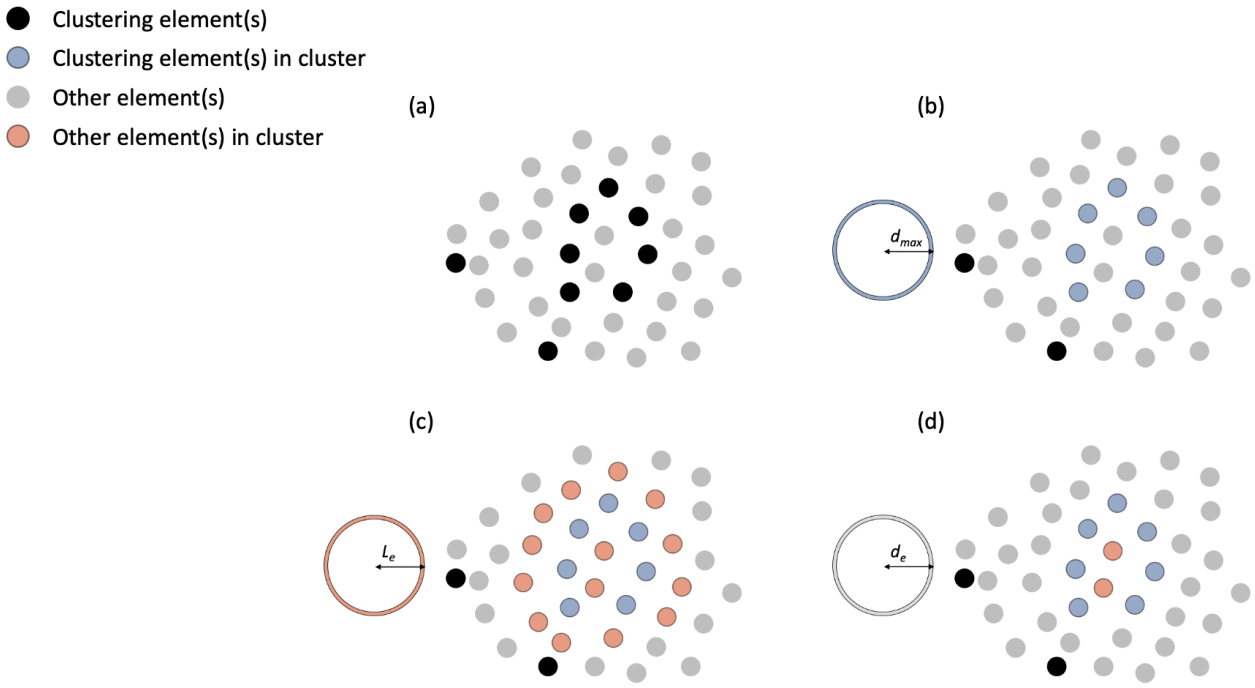


*Figure 7.4: Schematic of cluster definition using the MSM. (a) Ions of clustering element(s) identified. (b) Ions of the clustering element(s) within $d_{max}$ belong to the cluster. (c) Other ions within $L_e$ are incorporated in the cluster. (d) Other ions within $d_e$ from other ions than the clustering ions are eroded away from the cluster, thus defining a final cluster.*

The values of the abovelisted parameters in the MSM algorithm are determined by the person performing the cluster analysis. A comparison with randomised distributions of the same composition and positions as the data to be evaluated can aid in the decision-making. Nearest-neighbour distributions, cluster size distributions, and cluster count distributions are frequently used for this purpose. The nearest-neighbour distribution shows the distance from species of interest to other species (which can be chosen to be of the same type as or of other types than the species of interest). When the average distance between the species of interest is shorter for the experimental data than for the randomised data, clustering is indicated. Clustering often, but not always, gives a bimodal distribution of the experimental data, with one mode for the clusters and one for the matrix. Nearest-neighbour distributions can be determined for various orders of nearest neighbours. The cluster size distribution can be used to determine an appropriate value of $N_{min}$ for a given value of $d_{max}$. It shows the number of clusters as a function of $N_{min}$. The cluster count distribution can be used to find an appropriate value of $d_{max}$ for a given value of $N_{min}$. It shows the number of clusters as a function of $d_{max}$. Clustering is indicated if the number of clusters for small values of $d_{max}$ is higher for the experimental data than for the randomised data. Iteration might be needed to find appropriate values of $d_{max}$ and $N_{min}$ from cluster count distributions and cluster size distributions. Figure 7.5 shows a nearest-neighbour distribution and a cluster count distribution for Fe and Cr in Zircaloy-2 exposed to BWR operation. Both distributions indicate clustering.

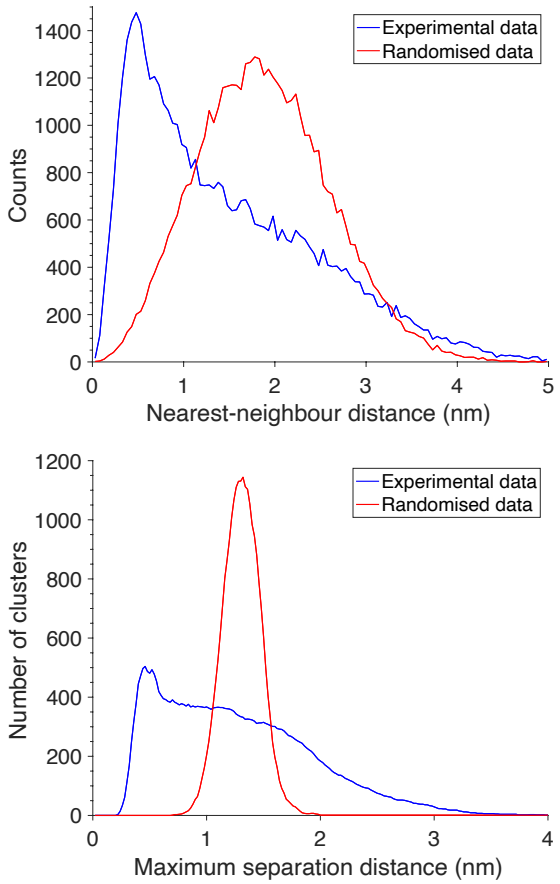


*Figure 7.5: Nearest-neighbour distribution (top) and cluster count distribution (bottom) for Fe and Cr in Zircaloy-2 exposed to BWR operation. Both distributions show that there is a non-random arrangement of Fe and Cr, thus indicating clustering.*

Another way of characterising clusters is by isoconcentration surfaces, which are the surfaces given by a specific concentration of one or more elements. (These surfaces are dependent on the voxel (volume pixel) size and the delocalisation (a 3D Gaussian smoothening of the ion to account for the uncertainty in ion position) used in the reconstruction.) From isoconcentration surfaces, proximity histograms, abbreviatedly called proxigrams, showing concentration as a function of distance from the surfaces, can be computed [143]. Isoconcentration surfaces and proxigrams can also be used for characterisation of other features than clusters, e.g. grain boundaries and phase boundaries.

Information that is often searched for in cluster analysis is number density, composition, and size. It might also be desirable to decide how the clusters are oriented with respect to the crystallography of the specimen. However, since crystallographic information is only occasionally obtained in APT analysis, it is often not possible to determine the cluster orientation in relation to the crystallography. Compared with laser pulsing, the

higher spatial resolution of voltage pulsing usually results in improved cluster detection [144] and more likely in better crystallographic information [145]. The increased spatial resolution of voltage-pulsed over that of laser-pulsed APT is more pronounced for instruments having a green laser than instruments having a UV laser [146].

### 7.1.3 Limitations and artefacts

In APT analysis, there are limitations that restrict what experiments can be performed and what information can be obtained. The physical processes of the technique and the assumptions made when doing the reconstruction can in some cases introduce artefacts that need to be understood in order to correctly interpret the results.

An important limitation of APT analysis is the risk of specimen fracture. Often, the analysis is terminated due to specimen fracture. The probability of fracture is very material dependent and is also affected by the analysis parameters. The specimen is subjected to a (Maxwell) stress, $\sigma$, proportional to the square of the electric field, $F$, according to

$$\sigma = \varepsilon_0 F^2/2, \qquad (7.4)$$

where $\varepsilon_0$ is the vacuum permittivity.

Voltage pulsing usually puts more stress on the specimen than laser pulsing, thereby increasing the risk of fracture. Therefore, laser pulsing has to be used for materials that do not withstand the stress imposed by voltage pulsing. These materials include poor electrical conductors and brittle materials.

Artefacts can be related to differences in evaporation field between different species. Preferential evaporation is one such artefact. It can occur for species having a lower evaporation field than the average evaporation field of the phase in question, meaning that they can evaporate between pulses if the field between pulses is too high. Similarly, preferential retention can occur when the field during pulsing is too low to evaporate species that require a higher-than-average evaporation field. Another artefact related to the difference in evaporation field between species is local magnification, which can occur for phases having a lower or higher evaporation field than the matrix. If the evaporation field of a particle embedded in the matrix is lower than the evaporation field of the matrix, the local magnification is lower, resulting in a smaller reconstructed size and a higher measured atomic concentration of the particle. If the evaporation field of a particle, instead, is higher than the evaporation field of the matrix, the local magnification is higher, resulting in a larger reconstructed size and a lower measured atomic concentration of the particle. Another artefact is related to surface migration of certain species, especially in laser pulse mode. When the specimen is heated by the pulse, some species migrate along the specimen surface and evaporate at a position

some distance away from their original position, often at crystallographic poles. Species with a higher evaporation field than the matrix are more likely to surface migrate due to their prolonged time at the specimen surface.

Since the mass-to-charge ratio is the chemical information obtained about the evaporated species, the isotopic composition of each element present in the sample has to be used for identification. Often there are spectral overlaps between some of the species in the sample, precluding certain assignment of spatial position for the individual ions and sometimes limiting the possibilities of accurate identification of elemental composition. Moreover, evaporation and detection of molecular ions commonly occur, making mass spectrum evaluation more complicated. Additionally, the peaks in the mass spectrum are not perfectly sharp but have a width. In voltage pulse mode this width is caused by the extension and non-uniform amplitude of the pulse in time giving some of the field-evaporated ions energies slightly lower than the maximum energy of the pulse (this is termed energy deficit), and in laser pulse mode it is caused by evaporation during cooling of the specimen after the pulse, giving so-called thermal tails to the peaks. The extension of the peaks along the mass-to-charge ratio axis often increases peak overlap and complicates mass spectrum evaluation further. The use of a reflectron can compensate the energy deficit in voltage mode, and the thermal effects in laser mode can be reduced by adjustment of analysis parameters. The difference in time between evaporation events cannot, however, be compensated by the reflectron.

Although APT analysis is sensitive to ions of all mass-to-charge ratios, and accordingly also to all elements of the periodic table, analysis of H content in the specimen can be difficult due to the presence of residual hydrogen gas in the vacuum chamber. The H atoms of the residual gas can bond to atoms at the specimen surface, forming molecules that evaporate at a lower field than the individual specimen atoms. Therefore, hydride peaks often appear in the mass spectrum, especially for specimens containing elements with high affinity for H. Peaks from H and $H_2$ also appear in the mass spectrum. These peaks can be attributed to field desorption during the pulses of some of the H atoms that bond to the specimen surface.

A further limitation of APT is the detection efficiency of the instrument. This limitation is usually not of major concern, since the detection efficiency is the same irrespective of mass-to-charge ratio. However, small clusters might not be observed due to all ions not being detected. In most of the instruments currently used, the detection efficiency is in the approximate range 57 %–80 % for instruments without and 37 %–50 % for instruments with reflectron. The reason for the lower values for instruments with reflectron is that there are grids in the reflectron that some of the ions hit, and the limited detection efficiency without reflectron is mainly due to that the area between the channels of the MCPs is inactive and no detection results when it is hit by ions.

If two or more ions hit the detector sufficiently close in time and/or space, there might be overlapping electronic signals that are registered as fewer events. This is referred to as pile-up, and there is thus a deadtime and a dead zone associated with each ion impact on the detector. A typical deadtime is around 3 ns, and the location of the dead zone

varies with the propagation of the electronic signals through the delay lines [147,148]. The delay line oriented ± 45° from the other two can in some cases be used to resolve overlapping signals. Due to pile-up, ions can end up undetected. Multiple ions hitting the detector (almost) simultaneously can have been evaporated as single ions at (approximately) the same time or originate from a molecular ion that has dissociated after evaporation. The former of the two processes commonly occurs for elements that have a high evaporation field and can thus lead to a smaller fraction of these elements being detected and their abundance being underestimated. Additionally, ions can escape detection due to formation of neutral species after field evaporation. Neutral species will not be accelerated by the electric field and will thus not be detected.

The detection limit, in terms of atomic fraction of a specific element, of APT is not straightforward to determine. Levels of a few tens of atomic ppm, sometimes even lower, can usually be detected [149]. There are multiple ways, using statistical methods, to estimate the detection limit when there is no peak at the expected position of a species in the mass spectrum. The Currie definition of detection limit [150] can be applied to APT [151]. According to the Currie definition, which assumes that the number of counts follows a normal distribution, a peak of height $2.71 + 4.65\sqrt{N_b}$, where $N_b$ is the number of background counts, would be detected 95 % of the time. There are also other methods based on the Poisson distribution that have been applied to APT to reduce the detection limit compared with the Currie method [152]. These methods (including the Currie method) are sensitive to the peak width (range of mass-to-charge ratio in the mass spectrum) assigned to the species of interest and are thus affected by the person performing the analysis.

Due to the large influence of measurement parameters, the possible influence on the material by specimen preparation, and the assumptions made during reconstruction, it is generally very difficult to accurately estimate the combined measurement uncertainty from an APT experiment. However, the counting statistics is frequently used to characterise the uncertainty in compositional measurements, using the standard deviation, $\sigma_i$, of the measured fraction (usually referred to as concentration or composition), $C_i$, of species $i$, given by

$$\sigma_i = \sqrt{\frac{C_i(1-C_i)}{N}}, \qquad (7.5)$$

where $N$ is the total number of background-corrected ranged species. Equation 7.5 relies on that the detection of ions can be considered a binomial process, that the volume probed is representative of the specimen as a whole, and that the atoms are randomly distributed. If local concentrations in subvolumes of the specimen are considered, also the detection efficiency, $\eta$, has to be considered in the expression for the standard deviation according to

$$\sigma_i = \sqrt{\frac{C_i(1-C_i)(1-\eta)}{N_s}}, \qquad (7.6)$$

where $N_s$ is the total number of background-corrected ranged species in the subvolume.

As the analysis conditions can affect the results to a large extent, suitable choice of analysis parameters is necessary to be able to calculate meaningful detectabilities or compositions. To get a low detectability and not to miss low concentrations of dilute species, it is necessary to keep the background low. The background arises due to several reasons. One is ionisation of residual gas atoms in the vacuum system of the instrument, one is electronic noise in the detector, and one is due to evaporation between pulses (which gives incorrect times of flight). This latter contribution to background affects all mass-to-charge ratios and is more prominent in voltage than laser mode, and the background is thus generally higher in voltage mode. It is, however, not always possible to make use of the lower background in laser mode to get a lower detectability or to accurately determine low concentrations. The reason for this is that the higher thermal diffusivity and lower evaporation field in laser mode in some cases can prevent detection of specific species. Preferential evaporation between pulses can lead to underestimation (of detectability or concentration) of some species. In voltage mode, a too high DC voltage in relation to the pulse needed for field evaporation or too high temperature can lead to this type of preferential evaporation [153].

### 7.1.4 Atom probe tomography of Zr alloys

There are a number of studies of Zr alloys, either in the as-produced state or exposed to various environments prior to analysis, in which APT at least partly has been used [13,18,19,23,39,50,51,83,84,86,96–98,107,110–112,154–192]. The studies reported in [180,190,191] are included in this thesis (Papers I, II, and IV, respectively), [18] is a publication of results from analyses of the same material as in Papers I, II, and III, and [50] is a publication of results from analyses of part of the materials in Papers IV and VI. In addition to APT studies, there are a number of older atom probe studies on Zr alloys performed using voltage-pulsed one-dimensional (1D) atom probe instruments, i.e. atom probes not capable of laser pulsing or tomography [8,9,193–199]. As Zr alloys are more prone to fracture when voltage pulse mode is used compared with laser pulse mode, and as an anodic oxide formed on the specimens during electropolishing preparation (increasing the risk of specimen fracture even more), [158,168,170], these 1D atom probe studies yielded relatively few ions. For the former reason, most APT studies have been performed using laser pulsing.

Of main interest to compare with the work in this thesis are studies performed on Zircaloy-type alloys, especially in the as-produced state and after reactor exposure. In [51,83,84,158,162,183,188,191], APT examinations of Zircaloy-type alloys in the as-produced state are presented and in [18,23,83,84,86,160,180,188,190,191] after reactor exposure, whereof [18,23,83,84,160,180,190,191] present results on materials exposed

in commercial BWRs and [86,188] on materials exposed in research reactors. The neutron flux in research reactors for materials testing is often higher, and the temperature is usually also different, compared with commercial reactors. These differences can make the microstructure and chemistry of the irradiated materials evolve somewhat differently.

Zr has high affinity for H, and Zr hydride species (ZrH, often $ZrH_2$, and sometimes $ZrH_3$) are typically detected in APT analyses. The detection of Zr hydride species can be due to the existence of dissolved or precipitated H in the specimen. This H can be incorporated into the specimen during exposure to autoclave corrosion or reactor operation, during cool-down after autoclave or reactor operation, or during specimen preparation. Also the hydrogen gas present in the vacuum system in the atom probe instrument can contribute to the detection of Zr hydride species if it adsorbs on the specimen and is co-evaporated with Zr. Especially the data evaluation of Nb-containing Zr alloys can be complicated by the presence of Zr hydrides and Nb hydrides, since the resulting spectral overlaps often are difficult to resolve.

Other overlaps that occur in Zr alloys are overlaps between $Cr^+$ and $ZrC^{2+}$, between $Fe^+$ and $ZrO^{2+}$, and between $Ni^+$ and $Sn^{2+}$. To avoid these overlaps, a high field is beneficial so that Cr, Fe, and Ni evaporate as $Cr^{2+}$, $Fe^{2+}$, and $Ni^{2+}$ [200]. As the field generally is higher in voltage mode than laser mode, voltage pulsing should be beneficial to overcome these overlaps. However, there are also overlaps between isotopes of Cr and Fe, Fe and Ni, and $Ni^{2+}$ and $Zr^{3+}$ that need to be accounted for. Due to transmutation of the elements in the Zr alloys during reactor operation, the isotopic abundances in reactor-exposed materials might not correspond to the natural isotopic abundances. However, as detailed calculations of the isotopic composition of the fuel cladding after rector operation are demanding, the natural isotopic abundances can be used as a reasonably good approximation when identifying peaks in the mass spectra [83,180,181,190]. Other uncertainties, such as peak overlaps (e.g. due to unknown amounts of hydride species) can affect the compositional analysis equally much or more. Figure 7.6 shows two mass spectra from APT analysis of in-BWR-exposed Zircaloy-2, one obtained using voltage pulsing and one obtained using laser pulsing.

Because of surface migration of Sn, the Sn distribution in the specimen might not always be properly reconstructed, and Sn is often detected at crystallographic poles [111]. However, APT observations of Sn-clustering in the oxide of autoclave-corroded [111] and in the metal of in-BWR-exposed [18] Zircaloy-2 have been made. This Sn-clustering should not be an effect of surface migration.

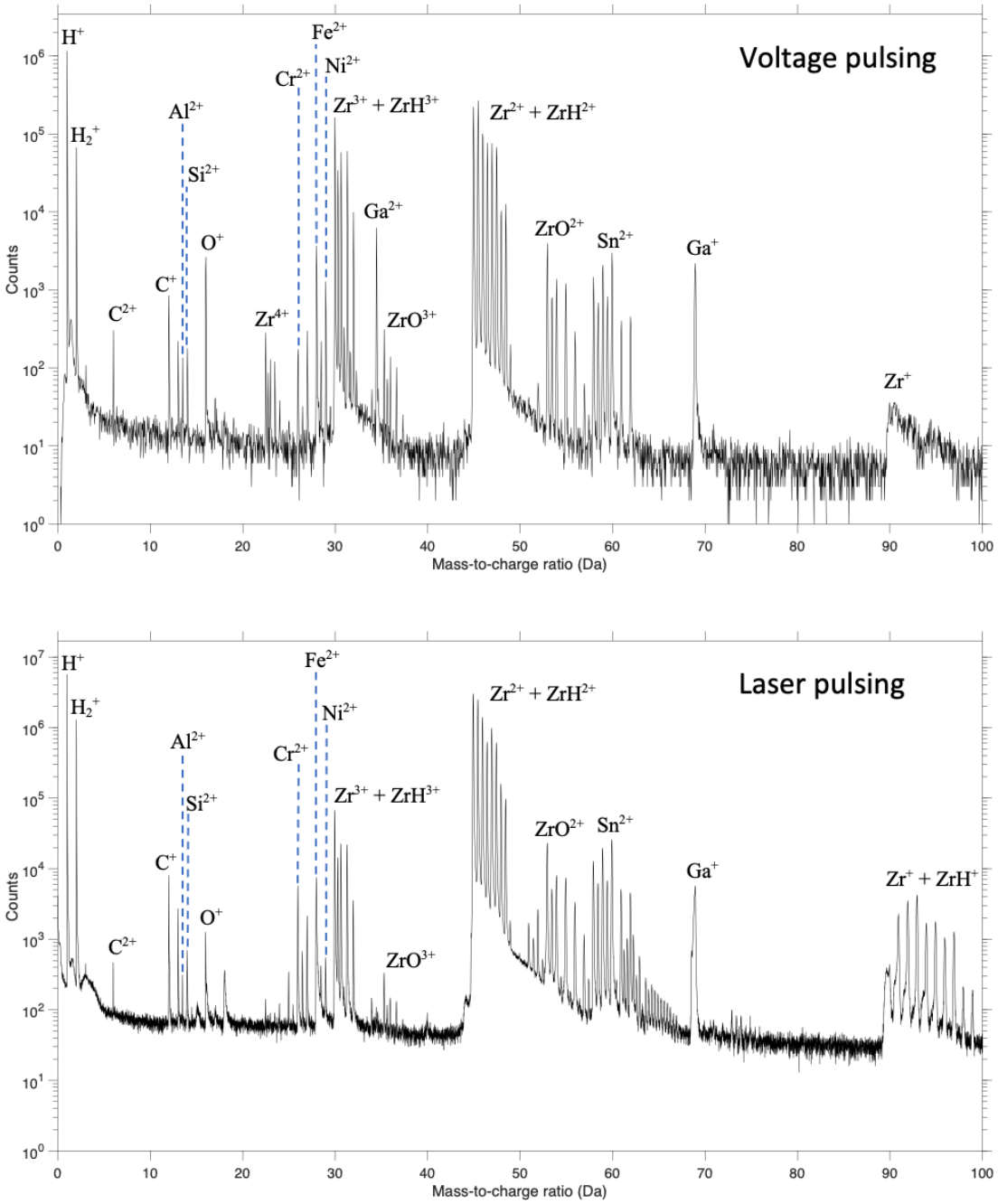


*Figure 7.6: Mass spectra of Zircaloy-2 exposed to BWR operation. The majority of the important peaks are labelled. The H and the Ga come from the specimen preparation process using focused ion beam–scanning electron microscopy (FIB–SEM). Different binning was used for the two histograms.*

## 7.2 Specimen preparation

The objective of specimen preparation is to create a needle that is sharp enough (radius below 100 nm) to enable field evaporation at a voltage that is lower, preferably much lower, than 15 kV. There are two conventional ways of preparing samples for APT, electropolishing and the lift-out technique using focused ion beam–scanning electron microscopy (FIB–SEM). Electropolishing is the traditional way of preparing APT specimens, and the FIB–SEM lift-out technique has been developed more recently and is currently the most common way to prepare APT specimens. Which specimen preparation technique that is most suitable to use is material dependent, and it also depends on the size of the sample and whether the analysis needs to be site specific.

### 7.2.1 Electropolishing

Electropolishing is performed in an electrochemical cell. A rod-shaped piece of the material to be analysed is placed vertically in the cell, which contains one lower region of inert liquid and one upper region of electrolyte. The specimen is connected via cables to a counter electrode that is likewise placed in the cell. When a voltage is applied, electropolishing occurs on the part of the specimen that is covered by the electrolyte. Eventually, a neck-shape forms on the specimen. Usually, the electrolyte is replaced by a weaker solution to perform the succeeding part of the electropolishing until the neck of the specimen breaks and two needles are formed. A schematic of an electropolishing setup is shown in Figure 7.7.

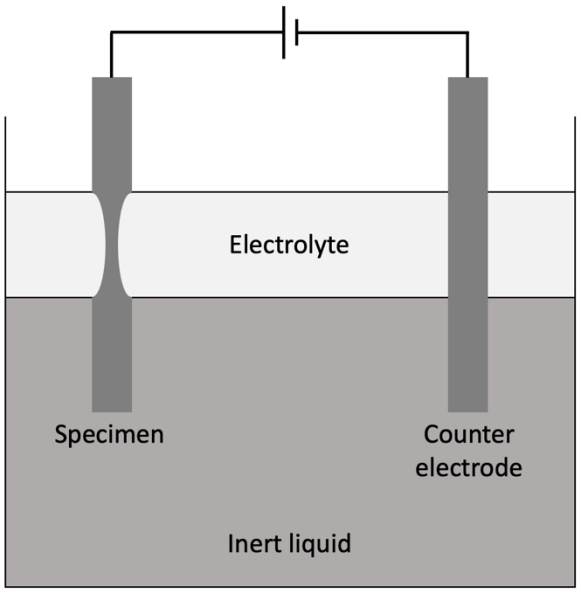


*Figure 7.7: Schematic of the electrochemical cell used for electropolishing.*

A prerequisite for electropolishing of a material is that it has good enough electrical conductivity. Also, it has to be possible to construct an electrochemical cell using that

material. In addition to the material requirements, a limitation of electropolishing is that it is difficult to control the process in such a way that specific features, e.g. grain boundaries, phase boundaries, and SPPs, are incorporated in the analysable part of the final needle. In the case of Zr alloys, electropolishing is possible, although the formation of anodic oxides can be a problem [50,193]. Electropolishing of neutron-irradiated Zr alloys (or other radioactive materials) is generally not preferable, as it will generate liquid radioactive waste.

### 7.2.2 Focused ion beam–scanning electron microscopy

FIB–SEM instruments combine a focused ion beam (FIB) unit with an SEM. In SEMs, samples are studied using electrons that are generated in an electron source and accelerated and focused through a column with electromagnetic lenses before interacting with the sample. The electron beam can be scanned over the sample surface. Depending on what is to be studied, various detectors can be used to collect signals from e.g. backscattered electrons (i.e. electrons of the electron beam that have interacted with the atoms of the sample and then taken a path out of the sample), secondary electrons (i.e. electrons emitted by the sample upon interaction with the electron beam), or X-rays (emitted from the atoms of the sample). SEMs are usually good tools for imaging conductive materials or non-conductive materials that have been coated with a conductive coating. FIBs work in a similar way, but the probing particles are ions instead of electrons. The ions can also be used for milling in the sample. Most commonly, liquid metal ions, especially Ga, are used, but in recent years FIBs having plasma ion sources, usually utilising Xe ions, have increased in number.

Usually, FIB–SEMs include a system for deposition of material on the sample surface. This deposition is done by introducing the material to be deposited in a precursor gas that adsorbs onto the surface while scanning the ion or electron beam over the surface. The precursor gas then splits up into a volatile compound that leaves the surface and a non-volatile compound that remains at the surface. C, Pt, W, and Au are materials that are common to deposit [201]. With a micromanipulator incorporated in the FIB–SEM it is possible to do lift-outs from the sample. Milling is done around the part to be lifted out before using the gas deposition system to solder the micromanipulator to the part and subsequently using milling to cut the part loose from the rest of the sample. There are various ways of doing lift-outs for APT specimens. One common way is to mill trenches at the two long sides of a rectangular site of interest at an angle of approximately 30° to the surface normal so that a wedge-shaped lift-out (i.e. a lift-out in the form of a triangular prism) is obtained [202]. The lift-out can then be divided into parts that are individually soldered to commercially available Si posts on a wafer containing many posts (e.g. $6 \times 6$ or $12 + 13$). Needles suitable for APT analysis are created by FIB milling (in an annular pattern) of the lifted-out material attached to the Si posts. Figure 7.8 shows the process of FIB–SEM preparation of APT specimens, and Figure 7.9 shows a sharpened tip.

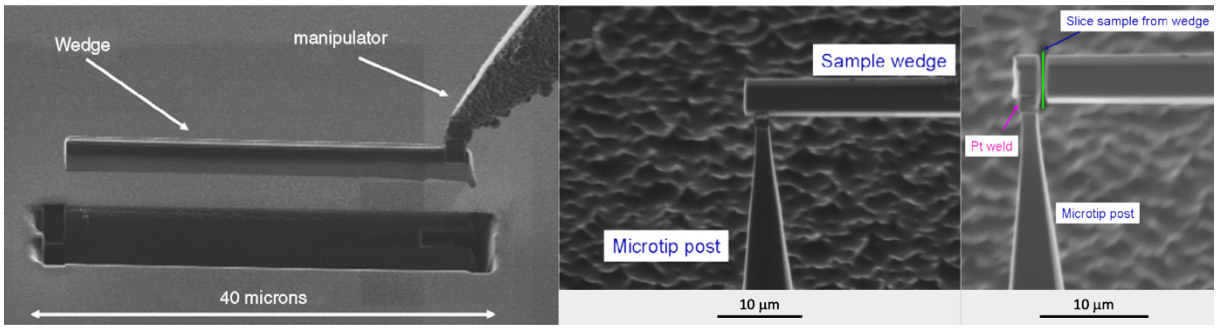


*Figure 7.8: FIB–SEM lift-out and attachment of a specimen to a microtip post. Adapted from* [202]. *Republished with permission from Elsevier.*

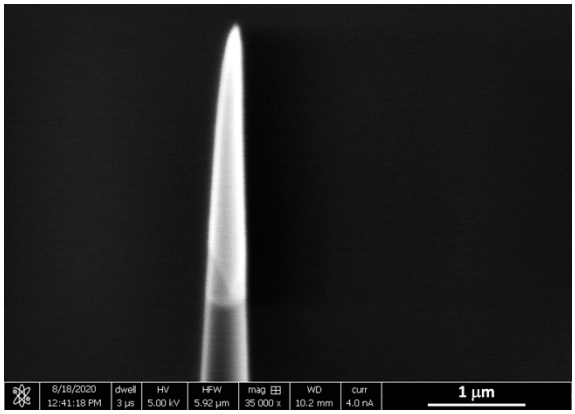


*Figure 7.9: A sharpened APT specimen.*

An advantage of FIB–SEM preparation is the possibility to do site-specific lift-outs to capture features of interest. It is usually also possible to prepare specimens from materials that are not suitable for electropolishing. An additional advantage is that the sample can be very small (which is preferred for radioactive samples). FIB–SEM operation might, on the other hand, require more training than electropolishing. Also, the equipment needed is more expensive. Most labs having APT instruments, however, usually have FIB–SEMs too.

FIB–SEM preparation has been observed to introduce hydrogen to Zircaloy-4 APT specimens [178]. FIB-introduced H can be dissolved in the matrix, be located in hydrides in parts of a specimen, or transform the entire APT specimen to a hydride. By performing the milling of the specimens at cryogenic temperature in the FIB–SEM, it is possible to create APT specimens not producing a higher H signal than expected from the H content of the material and the H resulting from the residual gas in the APT instrument.

# 8. Materials studied

This chapter presents the materials studied, which all are Zircaloy-2-type alloys. First, some general information about heat treatment and different variants of Zircaloy-2-type alloys is given. Then, the materials studied in the appended papers are described in more detail. Additionally, it is specified whether voltage or laser pulsing was used in the APT analysis of the respective material.

Depending on the amount of alloying elements within the specified range [37] and the heat treatment process during manufacture, various types of Zircaloy-2 can be produced. The average SPP size, and accordingly also the SPP number density, is determined by the heat treatment of the material. A normalised heat treatment parameter, $A$, is used to describe the heat treatment according to

$$A = \sum t_i e^{-Q/(RT_i)}, \qquad (8.1)$$

where $t_i$ is the time of the $i$-th heat treatment after quenching from the β-phase, $e$ is Euler's number, $Q$ is the activation energy (= 264 kJ/mol), $R$ is the ideal gas constant, and $T_i$ is the absolute temperature of the $i$-th heat treatment [203].

The size and number density of the SPPs are important for the corrosion and HPU properties of the material in reactor [204]. Two types of Zircaloy-2, one that has been and one that still is in use in BWRs, are the Westinghouse materials LK2 and LK3, respectively, where LK is the Swedish acronym for low corrosion (*låg korrosion*). In addition to small differences in content of alloying elements of the two materials, the heat treatment is different so that a smaller SPP size is obtained in LK2. LK3 was developed as successor to LK2 to mitigate the high corrosion rate and HPU resulting from the small SPP size [108]. LK3 has a lower uniform corrosion rate, a decreased risk of spacer shadow corrosion, and a delayed onset of accelerated growth [108,205]. Cladding tubes produced with an inner liner are usually designated by adding "/L" after the heat treatment designation, e.g. LK3/L for liner-containing cladding tubes of heat treatment LK3.

Most of the materials investigated in the work of this thesis were of the LK3 heat treatment. Material of LK2 heat treatment is only briefly mentioned in the review paper (Paper III) for comparison. Some work (parts of the work presented in Papers IV and VI) was performed on materials of non-commercial heat treatments.

Zircaloy-2 is generally the name for alloys within the composition range specified by ASTM [37] (given in Table 3.2). Materials of a slightly different composition can be classified as Zircaloy-2-type alloys. Such alloys comprise the commercial alloys HiFi and Ziron (which have higher Fe content than Zircaloy-2) and various model alloys, i.e. non-commercial alloys for testing purposes. Alloy 2, developed by Westinghouse, is a model alloy, and it is similar to HiFi, but its Cr content is outside the specified range of Zircaloy-2. The corrosion and, especially, the HPU of LK3-type Alloy 2 have been observed to be lower compared with LK3-type Zircaloy-2 [25].

## 8.1 Papers I, II, and III

The material analysed in Papers I and II is LK3/L Zircaloy-2 supplied by Westinghouse Electric Sweden AB (lot 82873). Its heat treatment parameter was $\log A = -14.2$, and its content of alloying elements and the impurity Si is given in Table 8.1. Prior to analysis, the material was used as cladding tubes in the commercial BWR at KKL as part of the Westinghouse fuel performance programme. Fuel rods of the same lot of material after operation for three to nine annual cycles (3C–9C) within this programme have been studied and characterised in previous work [18,20–24,52,80,85,101–103,205–220]. Some of these publications are reviewed in Paper III. The samples analysed in the work presented in Papers I and II were exposed for 3C (Paper II) and 9C (Papers I and II). Table 8.2 shows the rod identity and segment designation, rod average burnup, elevation, fast neutron fluence exposure, fast neutron dose, rod average oxide thickness, rod average H content, rod average HPUF, and rod growth of the samples. In the as-produced material, the SPP number density was $6.4 \times 10^{19}$ m$^{-3}$ [80]. After 3C no SPP number density is given in [80], but after 5C and 9C it is given as $2.2 \times 10^{19}$ m$^{-3}$ and $1.0 \times 10^{19}$ m$^{-3}$, respectively.

Sample preparation, including FIB lift-out, was performed in the hotlab of Studsvik Nuclear AB, and APT specimens were created at Chalmers University via FIB milling. Thus there were a limited number of specimens available for analysis, although it was possible to resharpen some of them to perform a second APT analysis after they had become too blunt to continue the first. All specimens were analysed using laser pulse mode, except for two specimens of the 9C sample that were analysed using voltage pulse mode.

*Table 8.1: Content of alloying elements and Si in wt% or wt ppm in the LK3/L Zircaloy-2 from KKL studied in Papers I and II.*

| **Material** | **Sn (%)** | **Fe (%)** | **Cr (%)** | **Ni (%)** | **O (%)** | **Si (ppm)** |
|---|---|---|---|---|---|---|
| **LK3/L Zircaloy-2** | 1.32 | 0.18 | 0.11 | 0.05 | 0.13 | 70 |

*Table 8.2: Rod identity and segment designation, rod average burnup, elevation, fast neutron fluence, fast neutron dose, rod average oxide thickness, rod average H content, rod average HPUF, and rod growth of the LK3/L Zircaloy-2 samples from KKL studied in Papers I and II.*

| | **3C** | **9C** |
|---|---|---|
| **Rod identity and segment designation** | AEB070-E4-N | AGB108-G6 |
| **Rod average burnup[1] (MWd/kgU)** | 34.7 | 78.7 |
| **Sample elevation from rod bottom (mm)** | 2030–2350 | 1218–1308 |
| **Sample fast neutron fluence ($E > 1$ MeV) (n m$^{-2}$)** | $7.4 \times 10^{25}$ | $16.5 \times 10^{25}$ |
| **Dose[2] (dpa)** | 11.9 | 26.5 |
| **Rod average oxide thickness[1] (μm)** | 5 ± 2 | 45 ± 7 |
| **Rod average H content[1] (wt ppm)** | 44 ± 2 | 664 ± 94 |
| **Rod average HPUF[1] (%)** | 12.8 | 30.0 |
| **Rod growth[1] (mm)** | 10.5 | 28.5 |

[1]Values from [80].
[2]Calculated from the fast neutron fluence ($E > 1$MeV) using the conversion factor for BWRs in [64].

## 8.2 Papers IV, V, and VI

In papers IV, V, and VI, three different lots of materials were studied. Two were of commercial heat treatment (Papers IV, V, and VI), and one was of non-commercial heat treatments (Papers IV and VI).

The materials of commercial heat treatment were LK3/L Zircaloy-2 and LK3/L Alloy 2 supplied by Westinghouse (lots 86788 and 86375, respectively). The heat treatment parameter of both materials was $\log A = -14.2$, and their content of alloying elements and the impurities C, Si, N, and Al are given in Table 8.3. For the particular lot studied, the Sn content in the Zircaloy-2 was higher than usual.

*Table 8.3: Content of alloying elements and the impurities C, Si, N, and Al in wt% or wt ppm in the LK3/L Zircaloy-2 and LK3/L Alloy 2 studied in Papers IV, V, and VI.*

| **Material** | **Sn (%)** | **Fe (%)** | **Cr (%)** | **Ni (%)** | **O (%)** | **C (ppm)** | **Si (ppm)** | **N (ppm)** | **Al (ppm)** |
|---|---|---|---|---|---|---|---|---|---|
| **LK3/L Zircaloy-2** | 1.49 | 0.18 | 0.13 | 0.061 | 0.12 | 143 | 91 | 40 | < 30 |
| **LK3/L Alloy 2** | 1.31 | 0.36 | 0.18 | 0.063 | 0.12 | 120 | 90 | 38 | < 30 |

Samples from cladding tubes before and after operation in the commercial BWR Oskarshamn 3 (O3) were studied. Additionally, some work was performed on the (unirradiated) Alloy 2 material after steam autoclave exposure at 415 °C for 30 days at AB Sandvik Materials Technology (now Alleima AB), but only the introduction of H during APT specimen preparation was studied (Paper VI). In-reactor-exposed samples were taken from sibling fuel rods. The irradiation time was 2082 days, corresponding to 11 cycles during approximately seven years. Samples of both alloys were taken from the fuelled region and from the plenum region of each rod, thus allowing for studying the materials at two different fluences. Table 8.4 shows the rod identity, rod average burnup, elevation, fast neutron fluence exposure, fast neutron dose, oxide thickness, rod average H content, and rod growth of the samples. In the calculation of the dose, the same conversion factor from fluence was used for the plenum samples and the samples from the fuelled region.

*Table 8.4: Rod identity, rod average burnup, elevation, fast neutron fluence, fast neutron dose, oxide thickness, rod average H content, and rod growth of the LK3/L Zircaloy-2 and Alloy 2 samples from O3 studied in Papers IV, V, and VI.*

| | **LK3/L Zircaloy-2** | **LK3/L Alloy 2** |
|---|---|---|
| **Rod identity** | 15-O3E9 | 15-O3F9 |
| **Rod average burnup[1] (MWd/kgU)** | 52 | 52 |
| **High-fluence sample elevation from rod bottom (mm)** | 2642–2645 | 2666–2669 |
| **Low-fluence sample elevation from rod bottom (mm)** | 3763–3766 | 3765–3768 |
| **High-fluence sample fast neutron fluence ($E > 1$ MeV) (n m$^{-2}$)** | $24 \times 10^{25}$ | $24 \times 10^{25}$ |
| **Low-fluence sample fast neutron fluence ($E > 1$ MeV) (n m$^{-2}$)** | $5.4 \times 10^{25}$ | $5.4 \times 10^{25}$ |
| **High-fluence sample dose (dpa)[2]** | 38 | 38 |
| **Low-fluence sample dose (dpa)[2]** | 8.6 | 8.6 |
| **Oxide thickness (μm)** | 12[3] | 11[4] |
| **Rod average H content (wt ppm)[5]** | 200 | 134 |
| **Rod growth (mm)** | 13.6 | 15.1 |

[1]Calculated.
[2]Calculated from the fast neutron fluence ($E > 1$MeV) using the conversion factor for BWRs in [64].
[3]Average of SEM measurements at four circumferential positions of a transversal cross section 2642 mm from rod bottom.
[4]Average of SEM measurements at four circumferential positions of a transversal cross section 2676 mm from rod bottom.
[5]Measured by hot-vacuum extraction (HVE).

Information on the oxide thickness measured by eddy current (EC) lift-off and on the H content of the rods is given in [25]. For Zircaloy-2 the oxide thickness in the studied region up to about 900 mm from the bottom of the rod (excluding spacer positions) was around 20 μm. The oxide thickness of the Alloy 2 rod reaches about three fourths of that value in the same region. In addition to the results presented in [25], the EC lift-off for Alloy 2 was measured along the rest of the rod up to about 2800 mm from the bottom of the rod, showing an increasing oxide thickness with the maximum value of just above 20 μm reached at the top of the measured region. According to SEM examinations, the oxide thickness (average value of four circumferential positions at one transversal cross section of each tube at elevations in the range 2600–2700 mm from rod bottom), the oxide thickness was 11 μm for Alloy 2 and 12 μm for Zircaloy-2. The values obtained by EC lift-off are thus higher than the values obtained by SEM. As EC lift-off is an indirect method of measuring the oxide thickness, the SEM measurements should be a better estimate of the actual oxide thickness. Figure 8.1 shows the oxide thickness from EC lift-off measurements for the lower parts of both rods, and Figure 8.2 shows the oxide thickness of the whole measured range of the Alloy 2 rod.

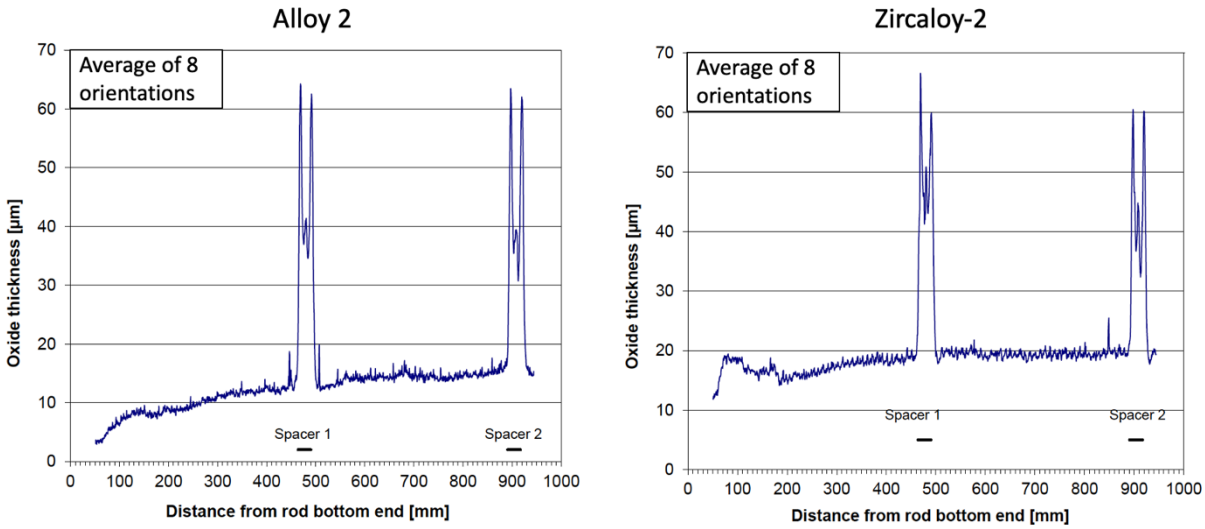


*Figure 8.1: Oxide thickness of the lower parts of the LK3/L Zircaloy-2 and Alloy 2 rods from O3 measured by EC lift-off. From* [25].

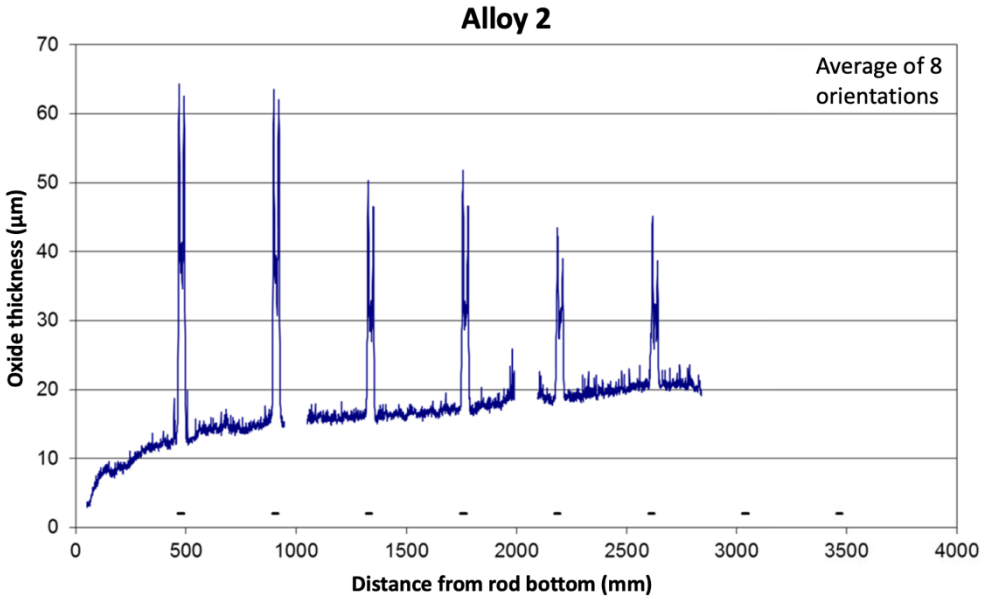


*Figure 8.2: Oxide thickness of the Alloy 2 rod from O3 measured by EC lift-off. From* [221].

Figure 8.3 shows the hydrogen content from hot vacuum extraction (HVE) as well as SEM measurements (of the area fraction of hydrides in transversal cross sections of the tubes). Using the HVE values, the H content of Alloy 2 was about 60–70 % of that of Zircaloy-2.

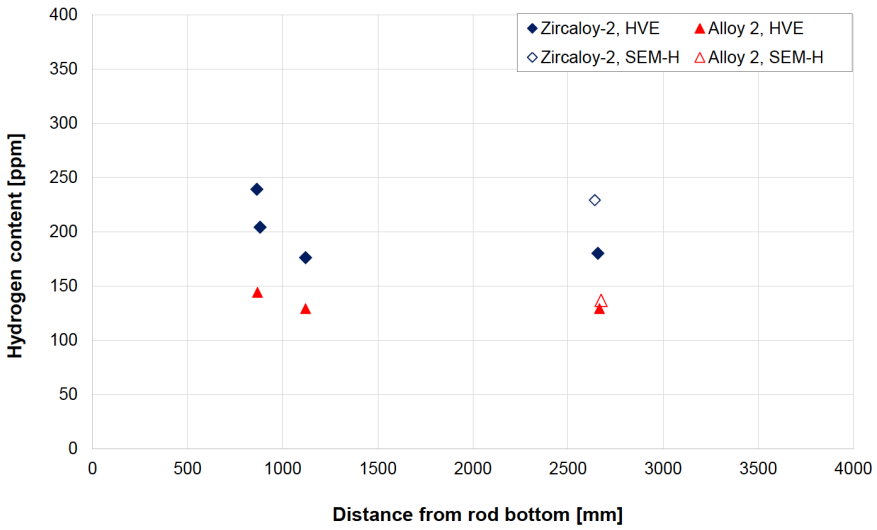


*Figure 8.3: Hydrogen content (wt ppm) at three positions of the LK3/L Zircaloy-2 and Alloy 2 rods from O3 measured by HVE and SEM. From* [25].

Preparation of the in-reactor-exposed samples was performed in the hotlab of Studsvik, and they were delivered to Chalmers University as small pieces, each approximately 3 mm in height and covering about one fourth of the transverse tube cross section. The pieces contain both the oxide and the inner liner, thus allowing for studies of more than just the metal. To facilitate FIB lift-outs from the metal/oxide interface (and nearby regions), one of the edges of each piece was ground so that an oxide thickness gradient was created. APT specimens were prepared from the pieces using FIB–SEM.

As-produced and autoclave-corroded samples were delivered as approximately 2 cm long pieces of cladding tubes. Lift-outs from the as-produced samples were performed approximately 40 µm from the outer surface of the tubes, as this distance, which corresponds to approximately 60 µm oxide thickness, is a distance that is relevant when considering potential accelerated corrosion.

APT analysis of the LK3/L Zircaloy-2 and Alloy 2 before and after operation in O3 was performed using both laser pulse mode and voltage pulse mode. Cryo-FIB was used for the final milling of some of the specimens (Paper VI). All the cryo-FIB-prepared tips were analysed using voltage pulsing. Specimens from the autoclave-corroded sample were analysed using laser pulsing.

The Zircaloy-2 of non-commercial heat treatments was a 2 mm thick plate that after β-quenching had been subjected to α-annealing at 770 °C for two different hold times, 5 min and 300 min, followed by cooling at three different rates. The means of cooling and approximate cooling rates were water quenching (WQ) (~300 °C/s), air cooling (AC) (~3 °C/s), and furnace cooling (FC) (~0.03 °C/s). There was thus a set of six materials of different heat treatments. They are referred to as 5WQ for five minutes hold time followed by water quenching, and so forth. The heat treatments were performed to vary the SPP size distribution and the content of solute elements (mainly Fe, Cr, and Ni) in the matrix. In previous work, the autoclave corrosion performance of these materials was studied, and the Fe content in solution in the matrix was estimated using thermoelectric power (TEP) measurements [14]. The content of alloying elements and the impurities C and Si in the materials is shown in Table 8.5. The Al content of the material is not specified, but should according to the ASTM standard be below 75 wt ppm [37] and is usually not exceeding half this value in commercial Zircaloy-2.

All combinations of annealing time and cooling rate were analysed using laser pulsing. The 300WQ material was additionally analysed using voltage pulsing.

*Table 8.5: Content of alloying elements and the impurities C and Si in wt% or wt ppm in the α-annealed Zircaloy-2 studied in Papers IV and VI.*

| **Material** | **Sn (%)** | **Fe (%)** | **Cr (%)** | **Ni (%)** | **O (%)** | **C (ppm)** | **Si (ppm)** |
|---|---|---|---|---|---|---|---|
| **α-annealed Zircaloy-2** | 1.36 | 0.17 | 0.11 | 0.07 | 0.13 | 132 | 90 |

# 9. Summary of results and discussion

The findings of the appended papers are summarised and discussed in this chapter. The focus of Papers I and II is the redistribution of Sn, Fe, Cr, and Ni in LK3/L Zircaloy-2 after BWR operation. Paper III presents a literature review of the microstructural evolution (including chemistry) during operation in the KKL reactor of the same lot of material as that studied in Papers I and II. Paper IV presents results of an investigation of the content of solute elements in the matrix of the LK3/L Zircaloy-2 and Alloy 2 and the α-annealed Zircaloy-2 described in Section 8.2. Paper V presents a comparison of the same lots as in Paper IV of LK3/L Zircaloy-2 and Alloy 2 after BWR exposure, with focus on clustering of Fe, Cr, and Ni. Paper VI deals with the introduction of H during APT specimen preparation of Zircaloy-2-type alloys, how this H introduction can be avoided, and how it affects the measurement of clustering of Fe, Cr, and Ni in irradiated material.

The same APT instrument, of type Imago LEAP 3000X HR, equipped with a green laser of wavelength 532 nm and having a detection efficiency of 0.37, was used for acquisition of all the data. When applicable, the detection efficiency has been accounted for in the results presented. The analysis parameters are described in the papers. Observations made regarding the difference between laser and voltage pulsing made in this work might not be the same for APT instruments equipped with other types of lasers.

## 9.1 Matrix chemistry in the unirradiated metal

As alloying elements are known to affect the in-reactor degradation of Zr alloys, and as the exact mechanisms of the degrading processes are still not known, it has since the introduction of Zr alloys in nuclear applications not been clear if the content of alloying elements in the matrix in the as-produced material has an impact on the degradation. Previous work using various methods, including synchrotron radiation microprobe X-ray fluorescence [11], TEP [12,14], and wavelength-dispersive X-ray spectroscopy (WDS) [15], has not yielded unambiguous results on the matrix concentrations of solute elements in Zr alloys. APT is a suitable technique for measurement of these concentrations, as it combines detectability of low levels of chemical elements with very high spatial resolution, easily avoiding any contributions from SPPs and grain boundaries. 1D atom probe has been employed in previous attempts to determine the matrix concentrations but suffered from frequent specimen fracture during analysis, resulting in limited statistical accuracy of the results [8,9]. The matrix concentration of Fe in ZIRLO has been measured to about 18 wt ppm using voltage-pulsed APT [13]. Due to the lack of unambiguous results for the matrix concentrations of solute elements in as-produced Zircaloy-2-type alloys of commercial heat treatment, an APT investigation with the aim of establishing these concentrations was performed. Additionally, to study the influence of heat treatment on matrix concentrations of solute elements and to relate these concentrations to the (autoclave) corrosion performance of

the materials according to previous work [14], an investigation of the α-annealed Zircaloy-2 was performed.

When analysing the matrix of Zr alloys, voltage pulsing (due to the higher field compared with laser pulsing) minimises the risk of Fe, Cr, and Ni evaporating as monovalent ions and thereby escaping detection (because of the overlaps with $ZrO^{2+}$, $ZrC^{2+}$, and $Sn^{2+}$). However, the, on average, lower specimen yield of voltage pulsing means that studies using voltage pulsing can be much more time consuming than studies using laser pulsing. In the study presented in Paper IV, voltage pulsing was used for the LK3/L Zircaloy-2 and Alloy 2, and laser pulsing was used for the α-annealed Zircaloy-2. The use of laser pulsing might have resulted in a slight underestimation of some species in the α-annealed materials. However, a comparison between the samples of different heat treatments was still possible. Additionally, voltage pulsing was used for one of the α-annealed Zircaloy-2 materials, 300WQ, to estimate the difference between the two pulsing modes.

The matrix concentrations of Fe, Cr, Ni, Al, Si, and C were measured in the as-produced LK3/L Zircaloy-2 and Alloy 2. The results did not indicate any differences between the two alloys. A few to several tens of wt ppm each of Al, Si, and C were detected in the matrix, whereas Fe, Cr, and Ni were below the detection limits. The Currie definition of detection limit [150] was used. Table 9.1 shows the detection limits of Fe, Cr, and Ni and the measured matrix concentrations of Al, Si, and C along with the total number of background-corrected ranged ions. It should be noted that the values measured for Si might (partly) be due to N or $CH_2$, because of unresolvable overlaps in the APT mass spectra.

According to the results in Table 9.1, the matrix concentrations of Fe, Cr, and Ni are below approximately 10 wt ppm. The slightly higher detection limits of Ni than those of Fe and Cr are due to higher background at the position of the Ni peak, and the slightly higher detection limits in Zircaloy-2 compared with Alloy 2 are due to the more limited statistics resulting from the lower number of ions detected. As the total concentrations of Fe, Cr, and Ni are higher in Alloy 2, there should not be more of these elements in the matrix of Zircaloy-2. The conclusion is thus that there appears to be no significant difference in matrix chemistry between Zircaloy-2 and Alloy 2.

*Table 9.1: Measured solute concentrations in the matrix of the as-produced LK3/L Zircaloy-2 and Alloy 2 in wt ppm. ±corresponds to two standard deviations of the counting statistics.*

| Material | Fe | Cr | Ni | Al | Si | C | Total number of background-corrected ranged ions |
|---|---|---|---|---|---|---|---|
| **LK3/L Zry-2** | < 12 | < 12 | < 16 | 18 ± 4 | 44 ± 5 | 113 ± 4 | 4.75 M |
| **LK3/L Alloy 2** | < 7 | < 7 | < 11 | 13 ± 2 | 31 ± 2 | 94 ± 2 | 15.6 M |

The matrix concentrations of Fe, Cr, Ni, and Al were measured for all combinations of annealing time and cooling rate of the α-annealed Zircaloy-2. The results of these measurements are presented in Table 9.2. As the statistics for the AC materials were rather poor due to a relatively low amount of ions detected, the results for the AC materials are not included in Table 9.2. Si and C were not analysed in the α-annealed Zircaloy-2, since the use of laser pulsing did not allow for a reliable determination of the concentrations of these elements.

*Table 9.2: Measured solute concentrations in the matrix of the α-annealed Zircaloy-2 in wt ppm. ± corresponds to two standard deviations of the counting statistics.*

| Material | Fe | Cr | Ni | Al | Total number of background-corrected ranged ions (M) |
|---|---|---|---|---|---|
| **300WQ voltage** | 37 ± 4 | 65 ± 5 | < 9 | 10 ± 2 | 12.5 |
| **300WQ laser** | 38 ± 3 | 37 ± 3 | < 5 | 13 ± 1 | 12.9 |
| **5WQ laser** | 23 ± 2 | 54 ± 2 | < 2 | 15 ± 1 | 33.5 |
| **300FC laser** | < 8[1] | < 8 | < 9 | 13 ± 4 | 2.2 |
| **5FC laser** | < 7[2] | < 7[2] | < 5[2] | 11 ± 1 | 21.6 |

[1]Estimated from the detection limit of Cr due to overlap with CO at 28 Da.
[2]Estimated from the run with highest concentration.

From the comparison of voltage pulsing and laser pulsing of the 300WQ material, it appears that mainly Cr could be slightly underestimated in the laser runs. Thus, the use of laser pulsing should not have resulted in concentrations very different from concentrations obtained using voltage pulsing.

According to the results in Table 9.2, the concentrations of Fe and Cr, which were randomly distributed in the matrix, are much lower for the slow cooling rate of FC than the fast cooling rate of WQ. This should be expected, as slower cooling from 770 °C, where the solubilities of these elements are higher, gives them more time to diffuse to SPPs. Also the results that were obtained for the intermediate cooling time of AC, being between those of WQ and FC, are in accordance with this observation. Ni was not detected in the materials, except for two runs of the 5FC material, in which 4–5 wt ppm was observed. This can be interpreted as that there are some concentration gradients or enrichment of Ni at microstructural features (grain boundaries or dislocations, although no clear such features were observed in the reconstructions). The diffusivities of Fe and Ni in α-Zr are much higher than that of Cr [56]. As reasoned in Paper IV, this difference in diffusivities should lead to the matrix content of Fe and Ni being the equilibrium content after both 5 and 300 minutes annealing time at 770 °C, but the equilibrium content of Cr should be reached only after 300 minutes annealing time. The slow cooling of FC should lead to virtually no Fe, Cr, or Ni in the matrix (in agreement with the experimental data), whereas the fast cooling of WQ should lead to gradients in the

Fe and Ni content in both 5WQ and 300WQ, gradients in the Cr content in 5WQ, and the equilibrium Cr content being retained in the matrix (except very close to SPPs) in 300WQ. The equilibrium content at 770 °C can thus be concluded to be around 65 wt ppm for Cr, above 37 wt ppm for Fe and below 9 wt ppm for Ni (using the voltage-pulsed data). The Al concentration in the matrix was observed to be in the range 10–20 wt. ppm irrespective of cooling rate. Due to the non-existence of an Al-rich phase in Zircaloy-2 (except for some possible enrichment in SPPs), the insensitivity of Al matrix content to cooling rate should be expected.

The measured matrix content of Fe using APT was not in good agreement with that estimated using TEP [14]. This discrepancy is probably due to the fact that the TEP estimation was based on the assumptions that only Fe contributed to the change in TEP value and that the Fe matrix content was 75 wt ppm in both WQ materials. According to the APT observations, the Cr matrix content varies more than that of Fe with respect to cooling rate, and the Fe matrix content of the WQ materials was less than 40 wt ppm.

In the previous study regarding autoclave corrosion of these materials, a similar oxidation behaviour of the materials of different heat treatments was observed [14]. There are no correlations between the corrosion behaviour and the matrix concentrations measured in this work. It thus seems that the initial matrix concentrations of Fe and Cr are not important for corrosion properties. The SPP size distribution seems to be more important [14].

## 9.2 Irradiation effects

This section summarises and discusses the APT observations made after reactor exposure of the studied materials. General observations are presented, followed by observations regarding clustering of Fe, Cr, and Ni, distribution of Sn, and ⟨c⟩-component loops. All appended papers contain, at least partly, results from in-reactor-exposed samples. The FIB–SEM lift-outs of the KKL materials were performed in the metal close to (up to a few μm from) the metal/oxide interface, and most of the lift-outs from the O3 materials were also made in the metal close to the metal/oxide interface, with a few lift-outs further away from the interface.

### 9.2.1 General observations

A striking observation when comparing the APT reconstructions is that there are large variations between and within individual specimens regarding the distribution of alloying elements. Some regions have high, whereas some regions have low, concentrations of alloying elements. Especially regions close to the oxide appear to have low content of alloying elements. Sn was, excluding SPPs, always the alloying element of highest observed concentration, with Fe mostly being the second most abundant alloying element. Some regions, notably close to SPPs, had higher Cr than Fe concentration. When voltage pulsing was used, more Ni than Cr was usually detected, and when laser pulsing was used, more Cr than Ni was always detected. It thus seems

that voltage pulsing is needed to reliably detect Ni, although some Ni was detected using laser pulsing.

In many of the specimens, grain boundaries were observed. Due to the high number density of these grain boundaries, they were most likely subgrain boundaries formed during growth of the oxide [100]. Enrichment of Sn and Fe, small amounts of Ni, and very small amounts of Cr was observed at the grain boundaries.

Fe, Cr, and Ni were in most specimens located in clusters that were located at expected positions of radiation-induced ⟨a⟩-loops, aligned in layers perpendicular to the ⟨c⟩-direction of the matrix. There was also segregation of Sn, Fe, and Ni to features interpreted to be ⟨c⟩-component loops. Additionally, Sn was in two cases observed to form clusters. Figure 9.1 shows three APT reconstructions obtained using laser pulsing of the KKL materials, two after 3C and one after 9C, displaying layers of clusters of Fe and Cr (Fe–Cr clusters), grain boundaries, a presumed ⟨c⟩-component loop, and differences in Fe and Cr content within and between individual grains.

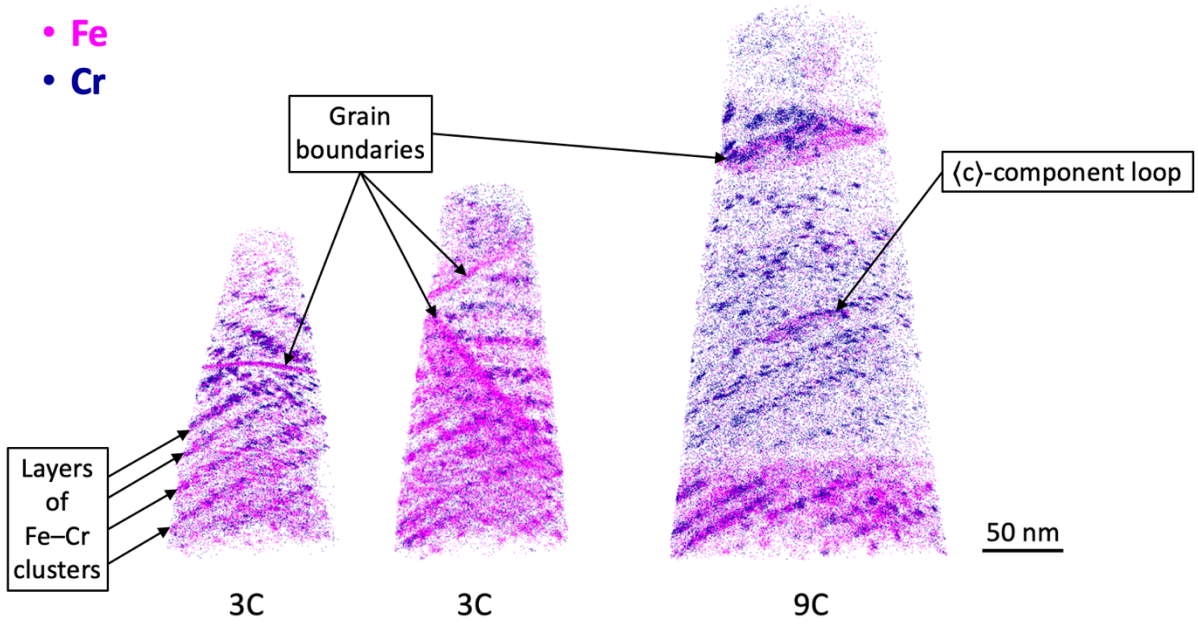


*Figure 9.1: Distribution of Fe and Cr in APT reconstructions obtained using laser pulsing of three specimens from the KKL materials.*

### 9.2.2 Clustering of Fe, Cr, and Ni

In comparison with unirradiated materials, there was a much larger amount of Fe, Cr, and Ni outside SPPs after reactor exposure. Most of the atoms of these elements were observed to be located in the clusters. The overall trend was that the average bulk (exclusive of SPPs) concentrations of Fe, Cr, and Ni increased with increasing fluence

(Papers II, IV, and V). However, the specimen-to-specimen variations were large, resulting in overlap between measured values from specimens of various fluence levels. An increase of these elements outside SPPs is expected, as the SPPs are dissolved to a larger extent after exposure to higher neutron fluence. For Sn, there was no average difference in bulk concentration with increasing exposure time (Paper II).

In all irradiated materials, Fe–Cr clusters were observed. They were typically spheroidal and around 5 nm in diameter, but there were also Fe–Cr clusters that were larger and of other shapes. The observation of these types of clusters in the 3C and 9C materials from KKL was made before the start of this project [18,19]. In the work presented in Paper II, a more detailed and quantitative analysis of these clusters was performed. Also, a comparison between 3C and 9C was made. On average, there was a slightly higher cluster number density, larger clusters, and higher cluster Cr content after 9C, as shown in Table 9.3. However, the grain-to-grain variations were larger than the differences between 3C and 9C. Sn was observed to on average be enriched in the clusters, but the variation between individual clusters was large. Almost no Ni was detected in the clusters. The clusters ranged from being almost pure Fe clusters to being almost pure Cr clusters, as shown in Figure 9.2. The largest clusters were mostly Cr rich and often of non-spheroidal shape. Large Cr-rich clusters were preferentially located close to grain boundaries or partially dissolved $Zr(Fe,Cr)_2$ SPPs.

*Table 9.3: Results of cluster analysis for the LK3/L Zircaloy-2 from KKL. ±indicates one sample standard deviation between the evaluated grains.*

| **Exposure time** | **$10^{23}$ clusters/m$^3$** | **Fe + Cr atoms/cluster** | **at.% Fe** | **at.% Cr** | **at.% Sn** | **at.% Zr** |
|---|---|---|---|---|---|---|
| **3C** | 4.4 ± 1.6 | 104 ± 44 | 16 ± 5 | 6.6 ± 5.5 | 1.5 ± 0.2 | 75 ± 3 |
| **9C** | 5.5 ± 3.4 | 225 ± 165 | 12 ± 7 | 9.2 ± 5.4 | 1.8 ± 0.9 | 77 ± 4 |

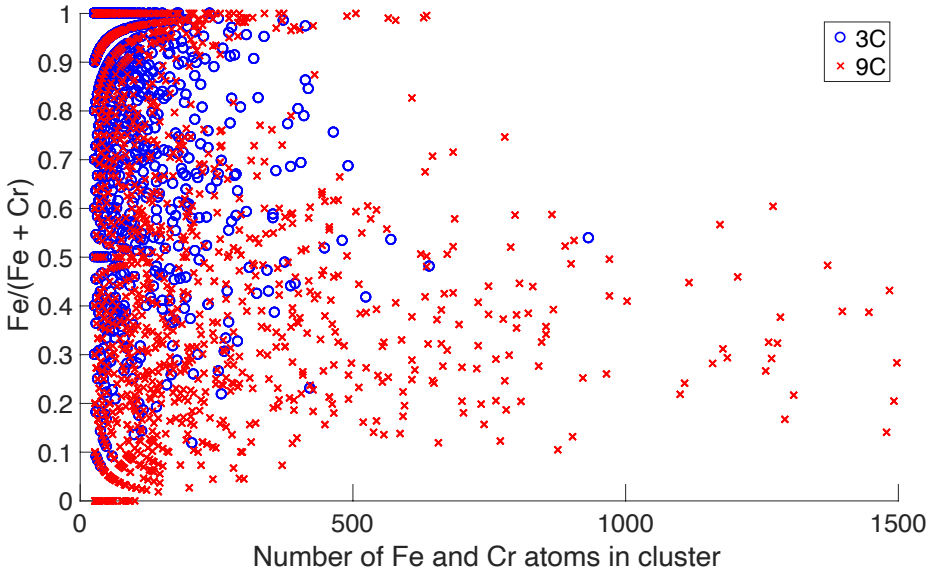


*Figure 9.2: Fe/(Fe+Cr) versus number of Fe and Cr atoms per cluster for the KKL materials. The 22 largest clusters (all Cr rich) after 9C have been omitted to make it possible to compare at the same scale.*

In addition to the previously observed Fe–Cr clusters, observations of clusters of Fe and Ni (Fe–Ni clusters) were also made (Papers I, IV–VI). Fe–Ni clusters appeared only when voltage pulse mode was used in the APT, whereas Fe–Cr clusters appeared both when laser pulse mode and when voltage pulse mode was used. It thus seems that voltage pulsing is needed to reliably detect Fe–Ni clusters, at least for instruments equipped with a green laser (as the instrument in this work). Like for Fe–Cr clusters, the Fe–Ni clusters were located in layers typical of layers of ⟨a⟩-loops. Both types of clusters were sometimes observed to be present within the same layers. Fe–Ni clusters were more widespread in the matrix than Fe–Cr clusters, i.e. not preferentially located close to grain boundaries or SPPs. An APT reconstruction containing a grain boundary and both types of clusters is shown in Figure 9.3.

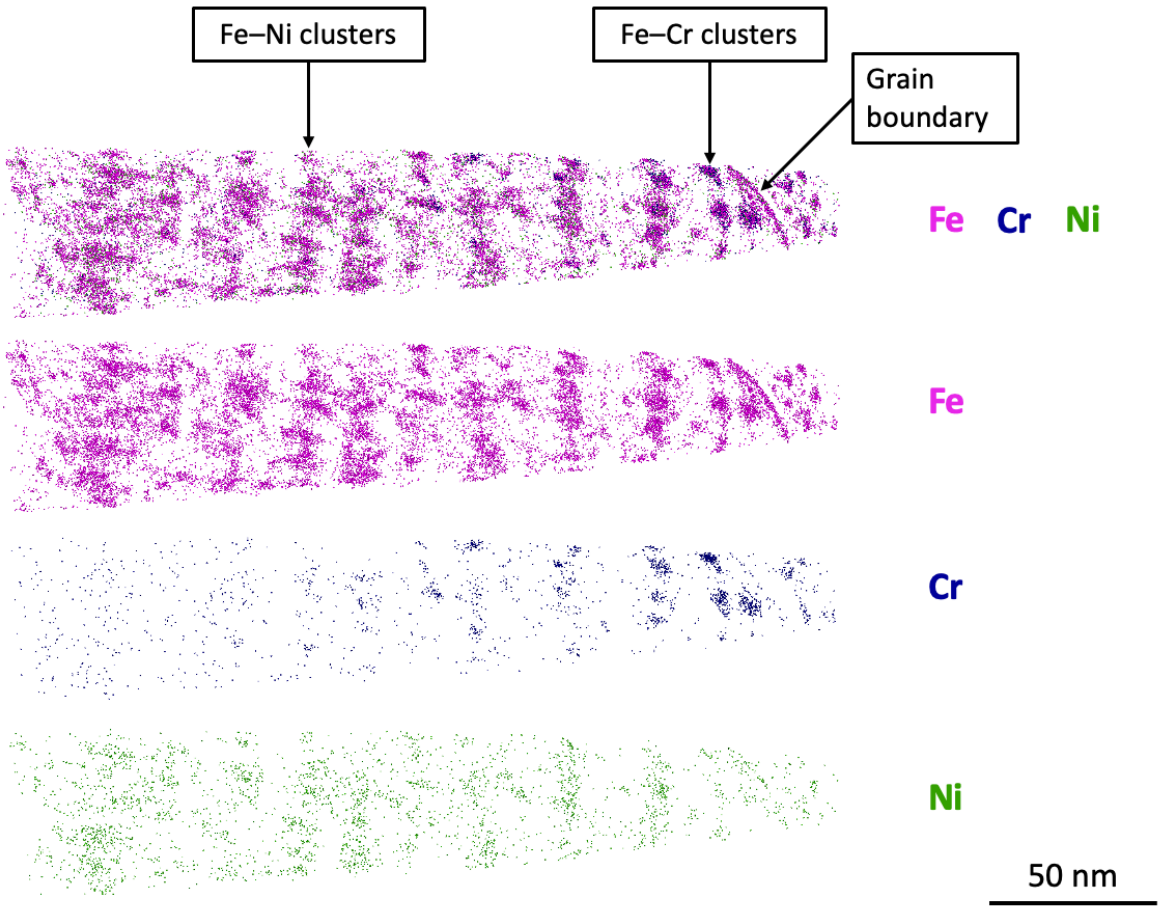


*Figure 9.3: Distribution of Fe, Cr, and Ni in a high-fluence LK3/L Alloy 2 specimen from O3.*

The Fe–Ni clusters were, in contrast to the Fe–Cr clusters, disc-shaped with diameter and thickness in the approximate ranges 5–15 (a few 20) nm and 2–4 nm, respectively. The Fe–Cr clusters were denser than the Fe–Ni clusters and had a higher Fe concentration (including Sn and Zr in the clusters). There were small amounts of Ni in the Fe–Cr clusters and very small amounts of Cr in the Fe–Ni clusters. In many of the voltage-pulsed APT analyses it was, from the crystallographic information obtained, possible to determine the ⟨c⟩-direction of the α-Zr matrix. It could thus be observed that the Fe–Ni discs occupied planes that were close to prismatic planes but with a tilt compared with perfect ⟨c⟩-axis alignment. This type of plane is what is the observed [67–69] and modelled [222] habit plane of ⟨a⟩-loops. It was, furthermore, observed that Fe–Ni discs within the same layer of clusters were oriented in directions with an angle of 60° between them, thus matching ⟨a⟩-loops located at all three families of first-order prismatic planes (Paper I). However, as the specimens were γ-hydrides during analysis (see Section 9.5), it could not unambiguously be determined that the segregation was closer to first-order than to second-order prismatic planes. (Since the transformation to γ-hydride had not been confirmed when Paper I was written, it was at that time assumed the analysed phase was α-Zr and the Fe–Ni discs were then concluded to be located on planes that were close to the first-order prismatic.) Nonetheless, it seems that the Fe–Ni

clusters are segregation of Fe and Ni at ⟨a⟩-loops. According to MD and Monte Carlo (MC) simulations, segregation of Fe [223] and Ni [224] at ⟨a⟩-loops can be expected, with segregation inside interstitial loops of 10 nm diameter and segregation along the edge of vacancy loops of the same size and interstitial loops of 18 nm diameter. The observation of disc-shaped Fe–Ni clusters thus matches the predicted segregation at the smaller interstitial loops. It is not clear how the Fe–Cr clusters are related to the loops, and their spheroidal shape does not match the predicted segregation of Fe and Ni to interstitial or vacancy loops. Figure 9.4 shows a typical Fe–Ni cluster and a typical Fe–Cr cluster and the ⟨c⟩-direction of the α-Zr matrix.

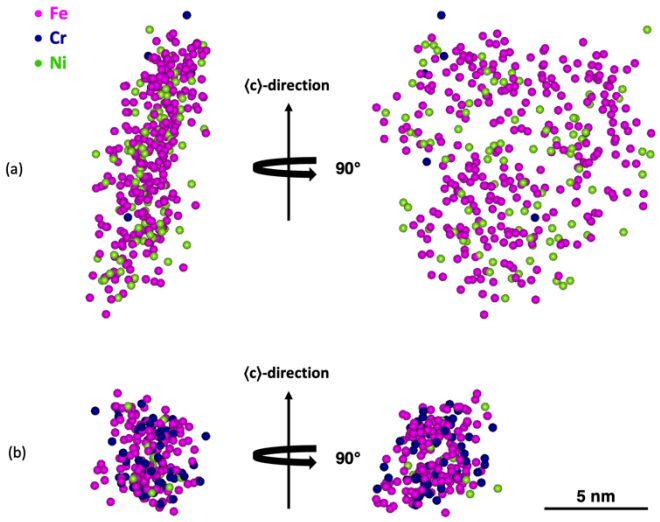


*Figure 9.4: (a) A typical Fe–Ni cluster and (b) a typical Fe–Cr cluster in a 9C specimen from KKL. The clusters are viewed in two directions with a relative rotation of 90° and perpendicular to the ⟨c⟩-direction of the Zr matrix. The Fe–Ni cluster is disc-shaped, and the Fe–Cr cluster is spheroidal.*

The concentrations of Fe, Cr, and Ni in the matrix surrounding the clusters were very low. In the Fe–Cr-rich regions of the KKL materials, the concentrations of Fe, Cr, and Ni in the matrix surrounding the clusters were in the approximate ranges 100–500, 50–200, and 10–90 at. ppm, respectively. There were no significant differences between 3C and 9C. As comparison, the bulk concentrations (including clusters and grain boundaries but excluding SPPs) were in the approximate ranges 1000–6000, 200–6000, and 20–200 at. ppm for Fe, Cr, and Ni, respectively. In the Fe–Ni-rich region observed using voltage pulsing after 9C presented in Paper I, similar observations were made, with the matrix concentrations of Fe, Cr, and Ni being about one order of magnitude lower than the bulk concentrations. The Ni concentration was, however, much higher

(1900 at. ppm) in this region compared with the Fe–Cr-rich regions observed using laser pulsing. The Sn concentration, which was close to the total concentration of 1.0 at.% in the alloy in both Fe–Cr- and Fe–Ni-rich regions, was not very different between bulk and matrix, with the matrix concentration being just a little lower (average differences of 0.15 at.% or lower). From the observations of the matrix and cluster content of Fe, Cr, and Ni being high, relative to the initial content below the detection limits, in all the studied in-reactor-exposed samples irrespective of exposure time and neutron dose, it is clear that the possible influence of the initial matrix content of these elements on degradation of Zircaloy-2-type alloys of the LK3 (or similar) heat treatment during reactor operation is negligible.

From the observations of the small average differences regarding Fe–Cr clusters between 3C and 9C (i.e. before and after acceleration in corrosion, HPU, and growth), it appears that these clusters are not decisive for acceleration in corrosion, HPU, and growth. In the KKL materials, Fe–Ni clusters were observed only after 9C and only using voltage pulsing. As no voltage pulsing was performed on 3C specimens, it cannot only from the work performed on the KKL materials be determined if disc-shaped Fe–Ni clusters were present also after 3C. However, as disc-shaped Fe–Ni clusters were observed, using voltage pulsing, in both the low- and the high-fluence samples from O3, it can be concluded that there should be Fe–Ni clusters also after 3C.

As Fe–Ni clusters were present in essentially all voltage runs, it can be expected that at least some of the Fe-rich clusters observed using laser pulsing were Fe–Ni clusters in which Ni was not detected. Using laser pulsing, no observations of disc-shaped Fe clusters were made, and it thus appears that laser pulsing using a green laser does not reveal the shape of Fe–Ni clusters. Disc- or ring-shaped clusters were not reported in previous work using green laser, where Fe–Cr clusters were observed [83], whereas ring-shaped clusters containing mainly Fe, but also Cr and Ni, have been observed using UV laser [84]. Irrespective of how reliable the detection of Ni in laser pulse mode is, the cluster number densities, the number of Fe and Cr atoms per cluster, and the Fe/Cr ratios observed should still be valid, and the differences observed between 3C and 9C should still be indicative of the evolution of clusters during reactor operation. The evolution of the Ni distribution, especially in clusters, on the other hand, would need voltage pulsing (or possibly another type of laser) to be revealed.

### 9.2.3 Distribution of Sn

Sn was in the irradiated materials observed to be non-randomly distributed. It formed a network-like structure, both between and within layers of Fe–Cr and Fe–Ni clusters, similar to observations made in other APT work [188]. Within the layers, Fe–Cr and Fe–Ni clusters were often located where Sn was enriched, although the Sn-enriched regions were larger, as shown in Figure 9.5. In some cases there was an anticorrelation between the concentration of Sn and the cluster layers, such that the Sn concentration was higher between than within the layers of clusters (Paper II), similar to other TEM and APT observations [21,188]. However, this anticorrelation was not always observed,

and the Sn concentration was sometimes higher within than between the layers of clusters. The network-like structure of Sn was observed in most of the voltage-pulsed analyses and in some of the laser-pulsed analyses.

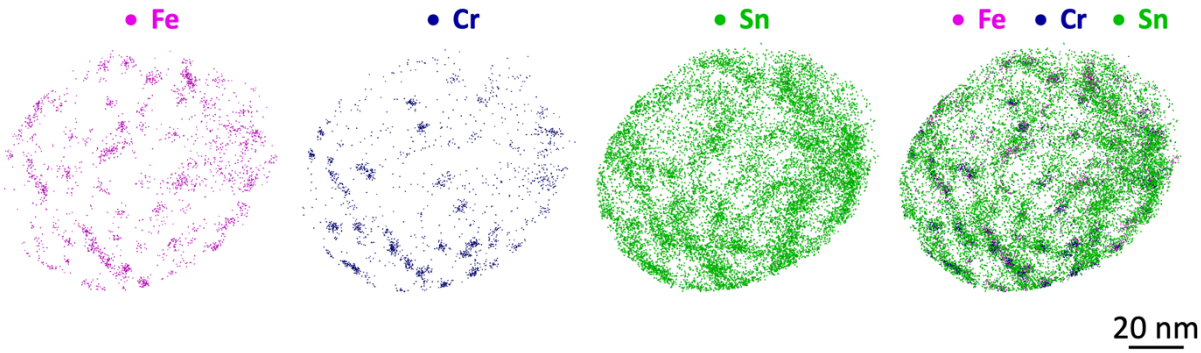


*Figure 9.5: One layer of clusters from a relatively Cr-rich part of a 3C specimen from KKL. The layer is viewed in the approximate ⟨c⟩-direction.*

In two grains or regions of grains, where there was almost no Fe, Cr, or Ni, and where the O content was lower than in the adjacent regions, Sn was observed to form clusters. Both of these regions were observed in the 9C material from KKL, and one of them (also containing what appears to be part of a ⟨c⟩-component loop, as described in Section 9.2.4) is shown in Figure 9.6. The number densities of Sn clusters were $14 \times 10^{23}$ m$^{-3}$ and $18 \times 10^{23}$ m$^{-3}$ (i.e. higher than the maximum number density of Fe–Cr clusters observed in the KKL materials), and the average values of the number of Sn atoms per cluster were 57 and 64. The Sn clusters were, in contrast to the Fe–Cr and Fe–Ni clusters, not clearly aligned, and it is thus unclear if the Sn clusters are related to ⟨a⟩-loops. A possible explanation for the existence of Sn clusters and the very low levels of Fe, Cr, and Ni is that these regions were hydride phases during reactor operation. Sn, Fe, Cr, and Ni have in modelling been predicted to prefer α-Zr over hydride phases [119]. Due to their faster diffusivities [56], Fe, Cr, and Ni might have migrated from the hydride upon its formation, whereas Sn formed clusters. Due to the necessity to use cryo-FIB in the specimen preparation process to study the H distribution (see Section 9.5), it was not possible to determine the phase by measuring the H content in the APT analysis of these specimens prepared using room-temperature FIB. If the Sn clusters are related to ⟨a⟩-loops in the same way Fe–Cr clusters are, and if they were located in hydride phases, the ⟨a⟩-loop number density appears to be higher in hydride phases than in α-Zr. It is also possible that Sn formed clusters without loops being present.

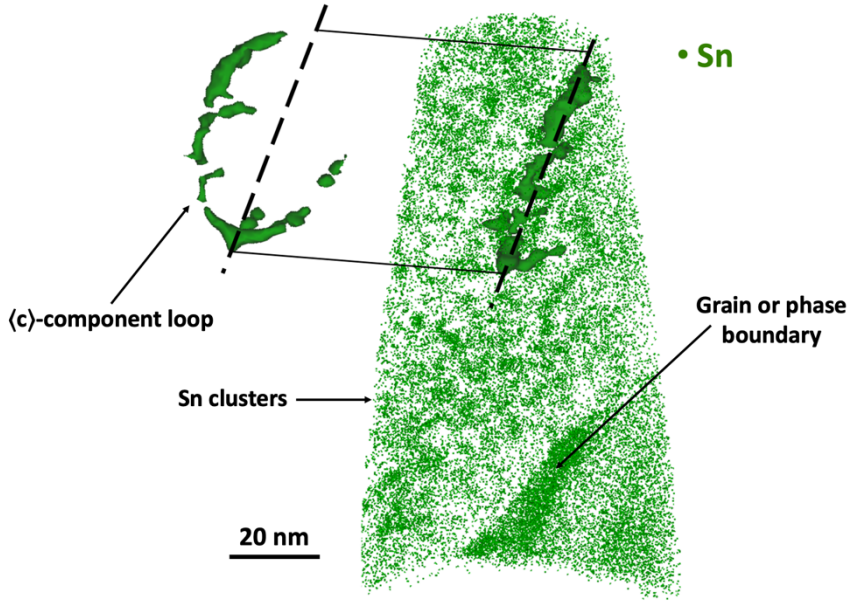


*Figure 9.6: APT reconstruction (36 nm thick slice) of a 9C specimen from KKL containing Sn clusters, a feature that appears to be part of a ⟨c⟩-component loop (displayed as an isoconcentration surface of Sn), and a grain or phase boundary.*

Sn was the alloying element found in highest concentration, around 2–3 at.%, at (sub)grain boundaries (Paper II). Apart from these observations of Sn, it was also detected at features interpreted to be ⟨c⟩-component loops, as described in Section 9.2.4.

### 9.2.4 ⟨c⟩-component loops

In the 9C material from KKL, five ring-shaped features (some of them also described in the previous work [18]) having diameters in the approximate range 20–60 nm and interpreted to be ⟨c⟩-component loops were observed. Three of the loops were decorated mainly with Sn, and two of the loops were decorated mainly with Fe. Small amounts of Fe were observed at the loops mainly decorated with Sn, and small amounts of Sn and Ni (at one of the loops) were observed at the loops mainly decorated with Fe. One of the loops decorated mainly with Sn, the one displayed in Figure 9.6, was observed as only a part of a loop and was located in one of the regions with Sn clusters described in Section 9.2.3. No ⟨c⟩-component loops were observed in any of the other materials. The presence of Sn and Fe, but not Ni, at ⟨c⟩-component loops is what should be expected from DFT modelling [63].

The sizes of the observed ⟨c⟩-component loops are smaller than those of ⟨c⟩-component loops observed with TEM [21,66]. As the volume of an APT analysis is very small,

only small ⟨c⟩-component loops can be detected in their entirety. Parts of larger loops present in APT reconstructions might, furthermore, sometimes be difficult to identify as ⟨c⟩-component loops. The observations of ⟨c⟩-component loops only in the 9C material from KKL might be due to the longer analyses obtained using laser pulsing for this material compared with the voltage-pulsed analyses of the high-fluence materials from O3. ⟨c⟩-component loops should be present in the high-fluence materials from O3, but it is from TEM measurements performed on the LK3/L from KKL [21] not clear if ⟨c⟩-component loops should be present in the 3C material from KKL or the low-fluence materials from O3. If there are ⟨c⟩-component loops in the 3C and the low-fluence materials, their number density should be significantly lower than in the 9C and the high-fluence materials [21,66].

## 9.3 Effects of higher Fe and Cr content

In this section the observations made on the distribution of alloying elements made in the O3 samples (Papers IV and V) are presented and discussed, especially in relation to the higher Fe and Cr content of Alloy 2.

There were after reactor exposure no obvious visual differences between Zircaloy-2 and Alloy 2. Small differences were observed between high-fluence and low-fluence specimens, with less Cr, smaller clusters, and, often, less clear cluster layers in the low-fluence specimens. From the composition measurements it was observed that there was on average lower content of Fe, Cr, and Ni in the matrix (including clusters) of the low-fluence specimens. However, the specimen-to-specimen variations were large, and the measured ranges overlapped between the two fluence levels, especially regarding Ni. There were no apparent differences between Zircaloy-2 and Alloy 2 regarding measured composition. The concentrations of Fe, Cr, and Ni in matrix and clusters after reactor operation of all four studied materials are shown in Table 9.4.

*Table 9.4: Measured concentrations (average and range) of Fe, Cr, and Ni in matrix and clusters of the LK3/L Zircaloy-2 and Alloy 2 from O3, in wt ppm.*

| Material | Fe | Cr | Ni |
|---|---|---|---|
| **High-fluence LK3/L Zry-2** | 1210 (800–1650) | 120 (28–440) | 160 (71–220) |
| **High-fluence Alloy 2** | 1150 (800–1500) | 81 (0–240) | 240 (170–290) |
| **Low-fluence LK3/L Zry-2** | 650 (530–880) | 24 (0–68) | 170 (120–340) |
| **Low-fluence Alloy 2** | 650 (510–840) | 15 (0–28) | 110 (84–140) |

Like for the concentrations presented in Table 9.4, there were from the cluster analysis (Paper V) no apparent differences between Zircaloy-2 and Alloy 2. The results of the cluster analysis (which was performed for one representative specimen of each material and fluence level) are shown in Tables 9.5 and 9.6 for two different values of the minimum number of detected Fe and Ni atoms needed to form a cluster, $N_{min} = 10$ (Table 9.5) and $N_{min} = 30$ (Table 9.6). The larger value, $N_{min} = 30$, was used to quantify mainly large clusters that appeared to be located at ⟨a⟩-loops, whereas the smaller value, $N_{min} = 10$, included also small clusters, not always located in the layers typical of layers of ⟨a⟩-loops.

*Table 9.5: Cluster number density, average number of Fe and Ni atoms per cluster, and average cluster content obtained in the O3 materials using $N_{min} = 10$.*

| Specimen | $10^{23}$ clusters/m$^3$ | Fe + Ni atoms/cluster | at.% Fe | at.% Ni | at.% Cr | at.% Sn | at.% Zr |
|---|---|---|---|---|---|---|---|
| **High-fluence Alloy 2** | 11 | 157 | 19 | 4.5 | 0.35 | 1.4 | 76 |
| **Low-fluence Alloy 2** | 5.0 | 135 | 23 | 1.9 | - | 1.1 | 74 |
| **High-fluence Zircaloy-2** | 12 | 175 | 23 | 3.2 | - | 1.3 | 73 |
| **Low-fluence Zircaloy-2** | 6.0 | 74 | 28 | 5.3 | - | 1.6 | 67 |

*Table 9.6: Cluster number density, average number of Fe and Ni atoms per cluster, and average cluster content obtained in the O3 materials using $N_{min} = 30$.*

| Specimen | $10^{23}$ clusters/m$^3$ | Fe + Ni atoms/cluster | at.% Fe | at.% Ni | at.% Cr | at.% Sn | at.% Zr |
|---|---|---|---|---|---|---|---|
| **High-fluence Alloy 2** | 5.6 | 262 | 17 | 4.3 | 0.38 | 1.5 | 78 |
| **Low-fluence Alloy 2** | 2.5 | 225 | 21 | 1.8 | - | 1.1 | 76 |
| **High-fluence Zircaloy-2** | 5.8 | 312 | 22 | 3.1 | - | 1.3 | 74 |
| **Low-fluence Zircaloy-2** | 1.7 | 148 | 23 | 4.9 | - | 1.5 | 72 |

The observed smaller cluster number density in the low-fluence specimens than in the high-fluence specimens could be explained by more loops being present in the high-fluence materials. A slight increase in ⟨a⟩-loop number density with fluence can be expected at the fluences of the O3 samples [21,219]. Alternatively, the lower cluster number density might be an effect of the clusters on average being smaller due to fewer Fe and Ni atoms being available after dissolution from SPPs, thereby making the number density of relatively large clusters not representative of the ⟨a⟩-loop number density. For the low-fluence Zircaloy-2 specimen, a smaller cluster size led to a lower cluster number density when $N_{min} = 30$ was used, but considering the large local chemical variations previously observed [18,21,22,83,85,190], this type of region with smaller cluster size could be expected also in the high-fluence materials. The observation of a slightly lower cluster number density in the low-fluence materials is in line with the observed difference between the 3C and 9C materials from KKL, although the difference appears to be more pronounced between the low-fluence and high-fluence O3 materials. It is likely that the larger difference in dose between the high- and low-fluence O3 materials is the reason for the larger dissimilarity between these samples.

The observations of there being no significant difference regarding matrix and cluster content of Fe, Cr, and Ni between Zircaloy-2 and Alloy 2 after reactor exposure is an indication that more of these elements remain in SPPs in Alloy 2. Alternatively, the analysed volumes might not be representative of the matrix and cluster chemistry on a larger scale. If there was more Fe, Cr, and Ni remaining in SPPs in Alloy 2, three speculative potential reasons for this could be that there was a larger reflux of dissolved Fe, Cr, and Ni to the SPPs in Alloy 2, that the chemical composition of the SPPs in Alloy 2 was altered so that they were more stable to irradiation, or that the SPPs in Alloy 2 were fewer and on average larger than in Zircaloy-2 so that the total SPP surface area (which should be decisive for dissolution) was similar in both materials. The first idea seems unlikely, considering that dislocation loops appear to be strong sinks for Fe, Cr, and Ni and that large (notably Cr-rich) clusters can form at the loops. No detailed comparison of the SPP size distribution, number density, or composition was made for the studied lots, neither before nor after reactor operation. Therefore it is not known how these SPP characteristics differed between the two materials, and there is thus no experimental evidence for any of the other two ideas.

SEM characterisation of LK3-type Zircaloy-2 and LK3-type HiFi has indicated that both $Zr(Fe,Cr)_2$ and $Zr_2(Fe,Ni)$ SPPs in HiFi on average are larger, whereas their number densities are similar for both alloys [55]. It is likely that the difference between Zircaloy-2 and Alloy 2 is similar with mainly larger SPPs in Alloy 2, although the higher Cr content of Alloy 2 should have a slight impact on the average SPP size and composition. If the SPP size in Alloy 2 is larger without the number density being lower, the surface area is larger than in Zircaloy-2, and the total dissolution of Fe, Cr, and Ni should be higher in Alloy 2.

A larger SPP size in Alloy 2 is likely the reason for the improved corrosion and HPU properties, since larger SPP size in Zircaloy-2 has been observed to lead to lower HPU and corrosion in reactor [204]. This observation is, however, not well understood at a

mechanistic level. One possible explanation for the lower HPU and corrosion due to larger SPP size might be that larger and fewer SPPs lead to a more favourable distribution of lateral cracks in the oxide, according to the mechanism proposed for corrosion in autoclave [99]. An additional explanation for the lower HPU and corrosion of Alloy 2 could be that it is due to the distribution of alloying elements in the oxide. The Fe/Ni ratio at oxide grain boundaries has been proposed to be of importance for HPU [112,225], and it is likely that the higher Fe content in Alloy 2 leads to more Fe at oxide grain boundaries, potentially leading to lower HPU.

The possibility that any real differences between Zircaloy-2 and Alloy 2 were not captured cannot be excluded. Similarly to in the KKL materials, there were large variations between and within specimens, meaning that statistical effects can have a large impact on the results. The lift-outs were approximately 20–30 μm in length, meaning that they sometimes spanned over just a few grains. As the grain-to-grain variations can be large, the lift-outs might not be representative of the material on a larger scale. However, there was no observed variability between the two alloys at either of the two fluence levels, meaning that any differences, if existing in both the low-fluence and the high-fluence samples, were missed twice.

## 9.4 In-reactor degradation

This section summarises the main observations made in the review paper (Paper III), which is focused on LK3/L Zircaloy-2 from KKL, and relates the observations made in the APT work performed in the project of this thesis to observations made in other studies. The idea is to connect observations made using various techniques to better understand in-reactor degradation of Zircaloy-2-type alloys.

### 9.4.1 Corrosion and H pickup

Regarding HPU and corrosion, the most relevant observations reviewed in Paper III seem to be the ones concerning the cracking of the oxide. In 3D-FIB examinations after 9C, hydrides extending from the metal to the metal/oxide interface were associated with cracks in the oxide [24,217]. The crack number density appears to increase with increasing exposure time, thus likely leading to an oxide that is more pervious and provides more paths for oxidising and hydriding species toward the metal/oxide interface. As there is a volume expansion in the transformation from α-Zr to hydride phases, it is likely that these cracks were formed during formation of the hydrides. Additionally, it is also possible that the better transport paths for hydrogen through the oxide to the metal leads to more hydrogen uptake and hydride precipitation when there are more cracks in the oxide.

Relating the APT observations to the increased corrosion and HPU at high burnup is not straightforward. As no large differences in alloying element content outside SPPs between 3C and 9C was observed, whereas there is a marked difference in oxide microstructure and SPP number density, it appears, like in the investigation of the O3 materials, that the SPPs themselves are more important for corrosion than the alloying element content in matrix and clusters. This gives support to the hypothesis of lateral crack formation at SPPs being important for corrosion resistance [99], although the relation between SPPs and cracks in the oxide was not thoroughly investigated in the reviewed papers. Apart from the potential effects of SPPs, it is possible that alloying elements have an important role in the transport of O and H through the oxide. One of the reviewed TEM studies revealed the segregation of Fe and Ni at what might be oxide grain boundaries close to dissolving SPPs in the oxide close to the metal/oxide interface [85], reminiscent of the APT observations after autoclave testing [107]. This type of segregation might be of importance, as it has been proposed that the Fe/Ni ratio at oxide grain boundaries affects HPU [112,225]. However, the APT observations from the KKL and the O3 materials do not provide much information on how the chemistry outside SPPs leads to differences between various exposure times regarding grain boundary segregation in the oxide.

### 9.4.2 Growth

As discussed in Paper III, it can be observed from values of rod growth [80], H content [80], and sizes and number densities of ⟨a⟩- and ⟨c⟩-component loops [21] that the number density of ⟨c⟩-component loops seems to be an important contributor to growth. The number density of ⟨a⟩-loops might also affect growth, but seemingly not as much. Additionally, the H content can according to the data be a contributor to growth, possibly to a lesser extent than ⟨c⟩-component loops. Similar observations of the H content (via precipitation of hydrides) inducing less growth than ⟨c⟩-component loops have been made elsewhere [4]. It should be noted that the rod growth measured is the elongation of the cladding tubes, which is a result of a combination of growth, creep, and volume expansion due to hydride precipitation.

The APT observations of the number density of Fe–Cr clusters not being very different after 9C compared with 3C is in line with the relatively low impact of ⟨a⟩-loops on growth. Also the observations of ⟨c⟩-component loops after 9C but not after 3C are in line with ⟨c⟩-component loops being important for growth. As Sn, Fe, and Ni were observed at ⟨c⟩-component loops, these elements can be suspected to impact one or more of formation, stability, and growth of ⟨c⟩-component loops, which in turn should affect growth.

## 9.5 Introduction of H during APT specimen preparation

During the course of this project it was discovered that preparation of APT specimens using standard room-temperature FIB introduced large amounts of hydrogen in the specimens. For specimens prepared using this method, voltage-pulsed APT analyses contained around 50 at.% H and laser-pulsed APT analyses 20–45 at.%. These observations were made for both irradiated and non-irradiated materials. From the 50 at.% H observed for voltage-pulsed runs, it was expected that the specimens during analysis were γ-hydrides rather than α-Zr. However, there is a potential of H ions escaping detection (e.g. due to dissociation of molecular ions after field evaporation and pile-up of H ions at the detector). Ion-correlation histograms [226] were used to estimate the potential loss of H ions. These histograms indicated that there was no significant H ion loss, thus indicating that the analysed phase actually was γ-hydride. This was confirmed by the crystallographic information obtained in the APT analyses. Although the γ-hydride phase matched well with the crystallographic information (poles and zone lines) visible on the individual hitmaps, it was in some cases not possible from this information only to clearly distinguish γ- from δ- and ε-hydrides. Adding analyses of interplanar spacings at pole positions and evaluating around 20 specimens, however, showed that γ-hydride best fitted the crystallographic information obtained in the data. It was thus concluded that the voltage-pulsed specimens during analysis were γ-hydrides. For the laser-pulsed specimens, in which the H content was lower, the crystallographic information obtained was less clear and did not allow for determination of the crystal structure. As the temperature during laser pulsing generally is higher than during voltage pulsing, the mobility of H, and accordingly also its migration away from the specimen apex, should be higher when laser pulse mode is used. It is thus reasonable to assume that also the laser-pulsed specimens were γ-hydrides during analysis. As the specimen preparation procedure was the same for both voltage-pulsed and laser-pulsed specimens, the phase transformation should have occurred for all specimens.

Other work has shown that the formation of hydride phases during FIB preparation of APT specimens of Zr alloys [178] and Ti alloys [227] can be avoided if the final milling steps in the FIB are performed at cryogenic temperature. To verify that the samples studied in the work of this thesis were not γ-hydrides before FIB preparation and to study the effect of the phase transformation from α-Zr to γ-hydride on the redistribution and clustering of alloying elements, a number of specimens of the LK3/L Zircaloy-2 and Alloy 2 described in Section 8.2, in both as-produced state and after reactor exposure, were prepared at cryogenic temperature at the final milling steps. As expected, these specimens were α-Zr during APT analysis, as confirmed by the crystallographic information obtained and the measured H content of below 2 at.%. Figure 9.7 shows an example of a hitmap from a γ-hydride specimen and an example of a hitmap from an α-Zr specimen along with stereographic projections used for phase identification.

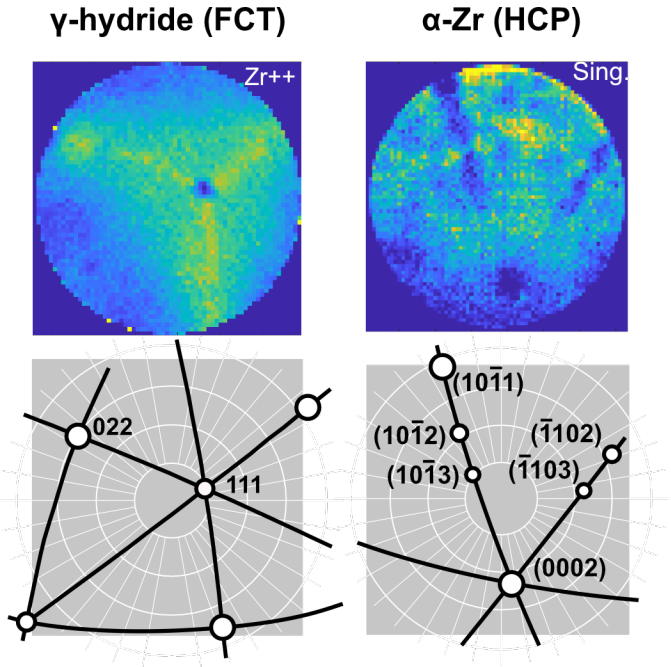


*Figure 9.7: Hitmaps obtained from analysis of a γ-hydride specimen and of an α-Zr specimen. Stereographic projections for pole identification are shown below the hitmaps. The γ-hydride hitmap has been filtered to display only $Zr^{2+}$ ions and the α-Zr hitmap to display only single detector events.*

The cryo-FIB-prepared specimens had a much lower yield than specimens prepared using room-temperature FIB. This is likely due to the higher field strength that was observed to be necessary to trigger field evaporation in α-Zr compared with γ-hydride specimens, which in turn leads to higher stresses exerted on the tips that then cause specimen fracture much earlier. In the relatively few runs of the cryo-FIB-prepared specimens that yielded enough data to show several layers of clusters of Fe, Cr, and Ni in the in-reactor-exposed materials, no evident differences in cluster appearance compared with γ-hydride specimens were observed. The variations between the specimens of the two preparation methods were lower than the typically observed variations between in-reactor-exposed specimens of room-temperature-FIB preparation. It thus seems that specimen preparation at cryogenic temperature is not needed when studying redistribution of these elements. However, it is still possible that better statistics could indicate differences between α-Zr and γ-hydride specimens. There is a volume expansion of 10–14 % associated with the transformation from α-Zr to γ-hydride [114], so slight differences regarding cluster sizes and distances between clusters can be expected. However, if the differences are very small, uncertainties in the APT reconstructions, even if calibrated using crystallographic information, can be so large that the differences might not be discernible.

Additionally, some APT specimens that had been prepared from the α-annealed Zircaloy-2 by electropolishing and studied in previous work [19,50] were included in the analysis of H content. These specimens were α-Zr during analysis, meaning that the electropolishing did not cause any phase transformation.

The observations of this study on introduction of H during specimen preparation might be of importance, as it strongly indicates that the use of the more time-consuming cryo-FIB preparation method resulting in lower APT specimen yield compared with room-temperature-FIB preparation is not needed when studying redistribution of alloying elements in Zircaloy-2-type (and likely other Zr) alloys. It also shows that cryo-FIB preparation or electropolishing (in addition to further measures) is necessary when attempting to study the H distribution in these alloys. It is, however, not impossible that the amount of hydrogen introduced during specimen preparation can be somewhat different if other types of Zr alloys are studied, if other types of FIB instruments are used, or if other types of electropolishing methods are employed. Zircaloy-4 has been reported not always to transform into hydride during room-temperature-FIB preparation [178].

# 10. Conclusions and outlook

The main conclusions that can be drawn from the research performed within this thesis are presented in the first section of this chapter. An outlook with suggestions for future work is given in the second section.

## 10.1 Conclusions

The research performed within the project of this thesis has contributed with new information regarding in-reactor degradation of Zircaloy-2-type alloys. Additionally, new insights regarding APT analysis of Zr alloys have been gained. There is a need for more studies to get a detailed mechanistic understanding of the processes leading to degradation of the alloys. The information obtained in this work can be used as pieces of the large puzzle of Zr alloy degradation and as input for future research. The key findings are summarised in the following list:

- The matrix concentrations of Fe, Cr, and Ni in as-produced commercial Zircaloy-2-type alloys are very low, below 10 wt ppm.

- The initial matrix content of Fe, Cr, and Ni in Zircaloy-2-type alloys seems less important than the SPP size distribution for autoclave corrosion properties.

- The initial matrix content of Fe, Cr, and Ni in Zircaloy-2-type alloys seems unimportant for in-reactor degradation.

- The content of Fe, Cr, and Ni outside SPPs increased with increasing fluence in Zircaloy-2-type alloys after use as cladding tubes in commercial BWRs, but there were large variations between specimens.

- Fe–Cr clusters and Fe–Ni clusters were observed at expected positions of ⟨a⟩-loops.

- Fe–Cr clusters appeared spheroidal, whereas Fe–Ni clusters appeared disc-shaped.

- Fe–Cr clusters, predominantly large and Cr rich, were preferentially located close to grain boundaries or partly dissolved SPPs, whereas Fe–Ni clusters were more widespread in the matrix.

- There was no large difference between Fe–Cr clusters before and after acceleration in corrosion, HPU, and growth; only small average increases in cluster number density, cluster size, and cluster Cr content were observed.

- After reactor exposure, no apparent differences regarding matrix content (including clusters), cluster number density, or cluster content were observed between Zircaloy-2 and the similar model alloy called Alloy 2, which has higher Fe and Cr content and better HPU and corrosion properties. It thus appears that the positive effects of higher alloy content of Fe and Cr are due to the presence of these elements in SPPs.

- ⟨c⟩-component loops decorated with Sn, Fe, and Ni were observed after but not before acceleration in corrosion, HPU, and growth.

- Sn formed a network-like structure, both within and between layers of Fe–Cr and Fe–Ni clusters.

- Room-temperature-FIB preparation of APT specimens transforms α-Zr to γ-hydride, whereas cryo-FIB or electropolishing preparation does not.

- The phase transformation from α-Zr to γ-hydride during FIB preparation seems not to affect the appearance of clusters of Fe, Cr, and Ni after reactor exposure.

- It is possible to analyse Zr alloys, both irradiated and unirradiated, using voltage-pulsed APT.

- The yield of γ-hydride APT specimens was higher than that of α-Zr specimens.

- Fe–Ni clusters in reactor-exposed samples were detected using voltage-pulsed APT, but not using laser-pulsed APT.

## 10.2 Outlook

To add information to the interpretation of the results obtained in the work of this thesis and to further enhance the understanding of degradation of Zircaloy-2-type alloys, more experimental as well as modelling studies are needed. Some suggestions, with focus on experimental studies, are discussed in this section.

To understand the effect of matrix content of alloying elements during autoclave corrosion, it could be of interest to perform APT of material that has been rapidly cooled after autoclave exposure so that the alloying elements are retained in the matrix. Performing this type of experiment on materials of different initial matrix content of alloying elements (as the α-annealed Zircaloy-2 materials in Paper IV) would, additionally, allow for an investigation of the influence of initial matrix content on matrix content during autoclave exposure.

After reactor exposure, it is not clear if the Fe–Cr and Fe–Ni clusters are located at both of interstitial and vacancy ⟨a⟩-loops or at only one of these types. TEM work has confirmed the colocalisation of Fe–Cr and Fe–Ni clusters with ⟨a⟩-loops of unknown characters [21]. Although TEM in principle is capable of determining the loop character of small ⟨a⟩-loops [228], it has proved difficult to do so on samples from in-reactor-exposed Zircaloy-2 [21]. Employing very careful specimen preparation might enable TEM determination of the distribution of alloying elements at the two types of ⟨a⟩-loops. In addition to experimental techniques, modelling might be useful to investigate if there is a preferred segregation of specific elements to interstitial or vacancy ⟨a⟩-loops. Modelling for Cr, similar to the MD and MC simulations that have predicted the segregation of Fe and Ni at ⟨a⟩-loops to be ring- or disc-shaped [223,224], could be used in predicting the energetically most favourable shape of Cr segregation at ⟨a⟩-loops.

To better understand the crystallography observed in the APT reconstructions, it might be beneficial to perform correlative studies, combining APT with e.g. FIM, TEM, TKD, or EBSD. Such studies might elucidate the crystal structure of grains in which it cannot be inferred from the information on the detector hitmap and might give better understanding of features such as grain boundaries and ⟨c⟩-component loops. Also the question of which character the loops associated with Fe–Cr and Fe–Ni clusters have might be resolved using correlative APT and TEM.

The Sn distribution in irradiated materials observed in this work and in the work by others [21,84,188] is not very well understood. By in greater detail studying the distribution of Sn, using APT and other experimental techniques, a more holistic view of how Sn is distributed after irradiation can be obtained. Modelling might be a good tool to get a better understanding of the observations of Sn.

It is still not clear what happens with the alloying elements, especially at small length scales, when they are incorporated into the oxide during reactor exposure. Therefore, more analyses of alloying elements in the oxide could be of importance. New APT instruments with new types of lasers, e.g. deep-UV laser, might improve the analysis of oxides compared with previous instruments. Also techniques complementary to APT might be useful in studying the distribution of alloying elements in the oxide. Although some electron probe microanalysis (EPMA) and TEM investigations have been performed to study alloying elements in the oxide [85,217], more information on e.g. grain boundary segregation and SPP distribution could be obtained if more studies using these techniques were performed. Also the microstructural evolution (apart from chemistry) of the oxide of in-reactor-exposed Zircaloy-2-type alloys could be better understood by more TEM investigations of the oxide. Comparing the in-reactor-formed oxides of Zircaloy-2 and Alloy 2 might give an increased understanding of how the increased Fe and Cr content leads to the lower corrosion and HPU of Alloy 2.

Furthermore, the positive effects of higher Fe and Cr content on hydrogen pickup and corrosion might be better understood by in detail studying the SPP size distribution in the metal of Alloy 2 and Zircaloy-2 before and after reactor operation (ideally by the same person on the same lots of materials and using the same instrument and specimen

preparation protocol). The region close to the metal/oxide interface should be of most interest in post-reactor material. Additionally, chemical analysis of the SPPs is needed to understand the chemical evolution of the materials.

It could be of interest to compare the post-reactor alloying element distribution in Zircaloy-2-type alloys with that in Zircaloy-4-type alloys. As the main difference between Zircaloy-2 and Zircaloy-4 is the absence of Ni in Zircaloy-4, such a comparison might give information on the role of Ni in the processes leading to degradation of Zircaloy-2-type alloys. APT, as well as other techniques, could be used for this comparison.

More understanding of the observations made and important information for future APT studies of Zr alloys might be obtained by in detail investigating the effect of conditions and parameters during APT analysis. For example, it is of interest to compare laser-pulsed APT utilising various laser types. Comparing results obtained using various laser types with each other and with results obtained using voltage pulsing might give information on potential artefacts introduced by the various lasers, e.g. the likely erroneous composition and distorted shape of Fe–Ni clusters using green laser. Also the effects on the results of applying simultaneous voltage and laser pulsing are of interest to investigate. Additionally, varying other analysis parameters, notably temperature, might have a slight influence on the results. Thus, an extensive study investigating the effect of analysis parameters might give some new insights.

# Acknowledgements

I would like to thank a number of people who have made me enjoy my time as a PhD student.

First of all I would like to thank my main supervisor Mattias Thuvander for giving me the opportunity to do this research and for the excellent support and guidance in this project. Thanks for teaching me atom probe analysis, for discussing interpretation of results, and for giving me constructive feedback on my presentations and drafts, no matter how close to the deadline I send them to you.

Many thanks to my co-supervisor Hans-Olof Andrén. Thank you for your enthusiasm about the subject, sharing your knowledge, and the valuable suggestions for improvement of my drafts. Many thanks also to my co-supervisor Mohammad Sattari for giving me guidance regarding microscopy.

Thanks to the other members of our small "Zr group", Krystyna Stiller, Andrea Fazi, and David Mayweg, for our good teamwork. Special thanks to David for the work we have done together; it has greatly improved the outcome of this project.

Thanks to Gustav Sundell and Pia Tejland for performing the experimental work that gave me good APT data to evaluate in the beginning of this project.

I would like to thank Sousan Abolhassani at Paul Scherrer Institut for the work we have done together on the review paper. It is good to combine the APT observations with the bigger picture.

This project has been facilitated thanks to my industrial collaborators; Magnus Limbäck, Zaheen Shah, Jonathan Wright, Antoine Claisse, and Jonna Partezana at Westinghouse; Karin Carling, David Schrire, and Clara Anghel at Vattenfall; Reidar Löfström, Henrik Eisenberg, Kristina Olsson, and Marcus Nilsson at OKG. Thanks for interesting and valuable discussions, and for providing relevant materials for the project.

The members of the international MUZIC-3 and MIDAS collaborations are acknowledged for interesting and fruitful discussions during the many meetings and webinars.

Göran Embring, Lars-Eric Bjerke, and Tell Andersson at Onsala Ingenjörsbyrå are acknowledged for interesting discussions on nuclear power, zirconium alloys, and accident tolerant fuel. Special thanks to Lars-Eric for trying to teach me how to play tennis.

Thanks to all my colleagues at the Division of Microstructure Physics, Eva Olsson Group, and Chalmers Materials Analysis Laboratory for company during lunch and coffee breaks. Special thanks to Stefan Gustafsson and Ludvig de Knoop for assistance with the microscopes, to Katarina Logg for taking care of the new LEAP instrument and organising the APT user group meetings, and to Ola Löfgren for assistance with computer-related issues. A special thank also to my office mate Kristina for keeping me company during the many hours spent in the office.

I would like to give a big thank to my friends and to my family; the greater family, grandparents, aunts, uncles, cousins, sister-in-law; and, last but not least, to my parents Gunnar and Annelie, my sister Anna, and my brother Mattias. Thank you for all your love and support!

# References


[1] BP, bp Statistical Review of World Energy, 71st edition, 2022.

[2] UNECE, Carbon Neutrality in the UNECE Region: Integrated Life-cycle Assessment of Electricity Sources, 2022.

[3] IAEA, Nuclear Power Reactors in the World, 2022.

[4] R.B. Adamson, C.E. Coleman, M. Griffiths, Irradiation creep and growth of zirconium alloys: A critical review, J. Nucl. Mater. 521 (2019) 167–244. https://doi.org/10.1016/j.jnucmat.2019.04.021.

[5] B. Cheng, R. Adamson, Mechanistic Studies of Zircaloy Nodular Corrosion, ASTM STP 939 (1987) 387–416. https://doi.org/10.1520/stp28134s.

[6] W.E. Berry, D.A. Vaughan, E.L. White, Hydrogen Pickup During Aqueous Corrosion Of Zirconium Alloys, Corrosion 17 (1961) 109t–117t. https://doi.org/10.5006/0010-9312-17.3.81.

[7] J. Eriksson, Atom probe tomography of Zircaloy-2 exposed to boiling water reactor operation, Licentiate thesis, Chalmers University of Technology, 2021.

[8] B. Wadman, H.-O. Andrén, Microanalysis of the Matrix and the Oxide-Metal Interface of Uniformly Corroded Zircaloy, ASTM STP 1132 (1991) 461–475. https://doi.org/10.1520/stp25522s.

[9] R.M. Kruger, R.B. Adamson, S.S. Brenner, Effects of microchemistry and precipitate size on nodular corrosion resistance of Zircaloy-2, J. Nucl. Mater. 189 (1992) 193–200. https://doi.org/10.1016/0022-3115(92)90532-P.

[10] H. Zou, G.M. Hood, J.A. Roy, R.H. Packwood, V. Weatherall, Solute distribution in annealed Zircaloy-2 and Zr-2.5Nb, J. Nucl. Mater. 208 (1994) 159–165. https://doi.org/10.1016/0022-3115(94)90207-0.

[11] A. Yilmazbayhan, O. Delaire, A.T. Motta, R.C. Birtcher, J.M. Maser, B. Lai, Determination of the alloying content in the matrix of Zr alloys using synchrotron radiation microprobe X-ray fluorescence, J. Nucl. Mater. 321 (2003) 221–232. https://doi.org/10.1016/S0022-3115(03)00267-8.

[12] M. Ivermark, Characterisation of the matrix chemistry in zirconium alloys, Ph.D. thesis, University of Manchester, 2009.

[13] D. Hudson, G.D.W. Smith, Initial observation of grain boundary solute segregation in a zirconium alloy (ZIRLO) by three-dimensional atom probe, Scr. Mater. 61 (2009) 411–414. https://doi.org/10.1016/j.scriptamat.2009.04.032.

[14] B. Hutchinson, B. Lehtinen, M. Limbäck, M. Dahlbäck, A Study of the Structure and Chemistry in Zircaloy-2 and the Resulting Oxide After High Temperature Corrosion, ASTM STP 1505 (2009) 269–284. https://doi.org/10.1520/JAI101106.

[15] M.Y. Yao, Y.F. Shen, Q. Li, J.C. Peng, B.X. Zhou, J.L. Zhang, The effect of final annealing after β-quenching on the corrosion resistance of Zircaloy-4 in lithiated water with 0.04 M LiOH, J. Nucl. Mater. 435 (2013) 63–70. https://doi.org/10.1016/j.jnucmat.2012.12.029.

[16] M. Griffiths, R.W. Gilbert, G.J.C. Carpenter, Phase instability, decomposition and redistribution of intermetallic precipitates in Zircaloy-2 and -4 during neutron irradiation, J. Nucl. Mater. 150 (1987) 53–66. https://doi.org/10.1016/0022-3115(87)90093-6.

[17] B.-C. Cheng, R. Kruger, R. Adamson, Corrosion Behavior of Irradiated Zircaloy, ASTM STP 1245 (1994) 400–418. https://doi.org/10.1520/stp15200s.

[18] G. Sundell, M. Thuvander, P. Tejland, M. Dahlbäck, L. Hallstadius, H.-O. Andrén, Redistribution of alloying elements in Zircaloy-2 after in-reactor exposure, J. Nucl. Mater. 454 (2014) 178–185. https://doi.org/10.1016/j.jnucmat.2014.07.072.

[19] G. Sundell, Atomic Scale Degradation of Zirconium Alloys for Nuclear Applications, Ph.D. thesis, Chalmers University of Technology, 2015.

[20] A. Harte, A Comparison of Proton and Neutron Irradiation-Induced Microstructural and Microchemical Evolution in Zircaloy-2, PhD thesis, University of Manchester, 2015.

[21] A. Harte, D. Jädernäs, M. Topping, P. Frankel, C.P. Race, J. Romero, L. Hallstadius, E.C. Darby, M. Preuss, The effect of matrix chemistry on dislocation evolution in an irradiated Zr alloy, Acta Mater. 130 (2017) 69–82. https://doi.org/10.1016/j.actamat.2017.03.024.

[22] A. Harte, M. Topping, P. Frankel, D. Jädernäs, J. Romero, L. Hallstadius, E.C. Darby, M. Preuss, Nano-scale chemical evolution in a proton-and neutron-irradiated Zr alloy, J. Nucl. Mater. 487 (2017) 30–42. https://doi.org/10.1016/j.jnucmat.2017.01.049.

[23] M. Topping, A. Harte, P. Frankel, C. Race, G. Sundell, M. Thuvander, H.-O. Andrén, D. Jädernäs, P. Tejland, J.E. Romero, E.C. Darby, S. Dumbill, L. Hallstadius, M. Preuss, The Effect of Iron on Dislocation Evolution in Model and Commercial Zirconium Alloys, ASTM STP 1597 (2018) 796–822.

https://doi.org/10.1520/stp159720160068.
[24] A. Baris, R. Restani, R. Grabherr, Y.-L. Chiu, H.E. Evans, K. Ammon, M. Limbäck, S. Abolhassani, Chemical and microstructural characterization of a 9 cycle Zircaloy-2 cladding using EPMA and FIB tomography, J. Nucl. Mater. 504 (2018) 144–160. https://doi.org/10.1016/j.jnucmat.2018.01.065.
[25] J.M. Wright, M. Limbäck, D. Schrire, M. Owaki, M. Nilsson, Commercial introduction and experience with the advanced high iron cladding HiFi in boiling water reactors, in: Proceedings of TopFuel, Prague, Czech Republic, ENS, 2018, A 0101.
[26] G. Choppin, J.-O. Liljenzin, J. Rydberg, Radiochemistry and Nuclear Chemistry, 3rd ed., Butterworth-Heinemann, 2002.
[27] IAEA, Nuclear Power Reactors in the World, Reference Data Series No.2, 2017 Edition, 2017.
[28] D.D. Baron, L. Hallstadius, Fuel Performance of Light Water Reactors (Uranium Oxide and MOX), in: Comprehensive Nuclear Materials – Basic Aspects of Radiation Efftects in Solid/Basic Aspects of Multi-Scale Modeling. Editor-in-Chief: R.J.M. Konings, Section Editors: T.R. Allen, R.E. Stoller, S. Yamanaka, Elsevier Ltd., 2012.
[29] C. Lemaignan, A.T. Motta, Zirconium Alloys in Nuclear Applications, in: Materials Science and Technology – A Comprehensive Treatment, R.W. Cahn, P. Haasen, E.J. Kramer (Eds.), Volume 10B: Nuclear Materials Part II (Chapter 7), Volume Editor B.T. Frost, 1994. https://doi.org/10.1002/adma.19950071220.
[30] G. Pfenning, H. Klewe-Nebenius, W. Seelmann-Eggebert, Karslruher Nuklidkarte, 6th ed., Forschungszentrum Karslruhe GmbH, 1998.
[31] Vattenfall. Tekniska data Ringhals. https://group.vattenfall.com/se/siteassets/sverige/ringhals/produktion/tekniska-data-utforlig-ringhals-151207.pdf. Retrieved 14 August, 2020.
[32] https://www.nrc.gov/reading-rm/basic-ref/students/animated-pwr.html. Retrieved 20 March, 2021.
[33] https://www.nrc.gov/reading-rm/basic-ref/students/animated-bwr.html. Retrieved 20 March, 2021.
[34] L. Hallstadius, S. Johnson, E. Lahoda, Cladding for high performance fuel, Prog. Nucl. Energy 57 (2012) 71–76. https://doi.org/10.1016/j.pnucene.2011.10.008.
[35] H.G. Rickover, The Decision to Use Zirconium in Nuclear Reactors, Zirconium Production and Technology: The Kroll Medal Papers 1975–2010, pp. 9–17, editor R.B. Adamson, ASTM, (2010).
[36] Z. Karoutas, J. Brown, A. Atwood, L. Hallstadius, E. Lahoda, S. Ray, J. Bradfute, The maturing of nuclear fuel: Past to Accident Tolerant Fuel, Prog. Nucl. Energy 102 (2018) 68–78. https://doi.org/10.1016/j.pnucene.2017.07.016.
[37] Standard Specification for Zirconium and Zirconium Alloy Ingots for Nuclear Application, ASTM Standard B350/B350M - 11(2021)e1, 2021.
[38] A.V. Nikulina, Zirconium-niobium alloys for core elements of pressurized water reactors, Met. Sci. Heat Treat. 45 (2003) 287–292. https://doi.org/10.1023/A:1027388503837.
[39] A. Fazi, H. Aboulfadl, A.H.S. Iyer, M. Sattari, K.M. Stiller, P. Lokhande, M. Thuvander, H.-O. Andrén, Characterization of as-deposited cold sprayed Cr-coating on Optimized ZIRLO™ claddings, J. Nucl. Mater. 549 (2021). https://doi.org/10.1016/j.jnucmat.2021.152892.
[40] A.V. Nikulina, Structural materials for elements of nuclear-reactor active zones: zirconium alloys in nuclear power engineering, Met. Sci. Heat Treat. 46 (2004) 458–462.
[41] A. Jostsons, J.G. Napier, Crystallographic techniques and data for transmission electron microscopy of zirconium, Australian Atomic Energy Commission, 1970.
[42] R.A. Johnson, J.R. Beeler, Point Defects in Titanium, in: Proceedings of Interatomic Potentials and Crystalline Defects, AIME, Pittsburgh, PA, 1981: pp. 165–177.
[43] G. Vérité, C. Domain, C.C. Fu, P. Gasca, A. Legris, F. Willaime, Self-interstitial defects in hexagonal close packed metals revisited: Evidence for low-symmetry configurations in Ti, Zr, and Hf, Phys. Rev. B. 87 (2013) 134108. https://doi.org/10.1103/PhysRevB.87.134108.
[44] P.J. Hazell, G.J. Appleby-Thomas, E. Wielewski, J.P. Escobedo, The shock and spall response of three industrially important hexagonal close-packed metals: Magnesium, titanium and zirconium, Philos. Trans. R. Soc. A Math. Phys. Eng. Sci. 372 (2014) 20130204. https://doi.org/10.1098/rsta.2013.0204.
[45] D.J. Bacon, Point defects and clusters in the hcp metals: their role in the dose transition, J. Nucl. Mater. 206 (1993) 249–265. https://doi.org/10.1016/0022-3115(93)90127-K.
[46] A.R. Verma, O.N. Srivistava, Crystallography for Solid State Physics, Wiley Eastern Limited, 1982.
[47] D. Hull, D.J. Bacon, Introduction to Dislocations, 5th ed., Butterworth-Heinemann, 2011.
[48] V.G. Kapinos, Y.N. Osetsky, P.A. Platonov, Computer simulation of vacancy loops and stacking faults in zirconium, J. Nucl. Mater. 195 (1992) 83–101. https://doi.org/10.1016/0022-3115(92)90365-R.

[49] D.E. Laughlin, B.Y. Wong, The Crystallography And Texture Of Co-Based Thin Film Deposited On Cr Underlayers, IEEE Trans. Magn. 27 (1991) 4713–4717. https://doi.org/10.1109/20.278924.
[50] M. Thuvander, H.-O. Andrén, Methods of quantitative matrix analysis of Zircaloy-2, Ultramicroscopy 111 (2011) 711–714. https://doi.org/10.1016/j.ultramic.2010.12.008.
[51] T. Sawabe, T. Sonoda, S. Kitajima, T. Kameyama, Analysis of atomic distribution in as-fabricated Zircaloy-2 claddings by atom probe tomography under high-energy pulsed laser, J. Nucl. Mater. 442 (2013) 168–174. https://doi.org/10.1016/j.jnucmat.2013.08.048.
[52] S. Abolhassani, D. Gavillet, F. Groeschel, P. Jourdain, H.U. Zwicky, Recent Observations on the Evolution of the Secondary Phase Particles in Zircaloy-2 under Irradiation in a BWR up to a High Burnup, in: Proceedings of International Topical Meeting on LWR Fuel Performance, April 10–13, Park City, Utah, USA, 2000: pp. 470–484.
[53] P. Rudling, K. Lundblad Vannesjö, G. Vesterlund, A.R. Massih, Influence of Second-Phase Particles on Zircaloy Corrosion in BWR Environment, ASTM STP 939 (1987) 292–306. https://doi.org/10.1520/STP28128S.
[54] Y. Ito, T. Furuya, The Effect of Annealing Parameter on Corrosion Resistance of Zircaloy-2, J. Nucl. Sci. Technol. 32 (1995) 1118–1126. https://doi.org/10.1080/18811248.1995.9731826.
[55] Z.D. Shah, Characterizing and Modelling Precipitation in Zirconium Alloys, Ph.D. thesis, University of Manchester, 2019.
[56] G.M. Hood, Point defect diffusion in α-Zr, J. Nucl. Mater. 159 (1988) 149–175. https://doi.org/10.1016/0022-3115(88)90091-8.
[57] E. Tenckhoff, Review of Deformation Mechanisms, Texture, and Mechanical Anisotropy in Zirconium and Zirconium Base Alloys, ASTM STP 1467 (2005) 25–50. https://doi.org/10.1520/stp37501s.
[58] F. Onimus, J.L. Béchade, Radiation Effects in Zirconium Alloys, Elsevier Inc., 2012. https://doi.org/10.1016/B978-0-08-056033-5.00064-1.
[59] K. Nordlund, S.J. Zinkle, A.E. Sand, F. Granberg, R.S. Averback, R.E. Stoller, T. Suzudo, L. Malerba, F. Banhart, W.J. Weber, F. Willaime, S.L. Dudarev, D. Simeone, Primary radiation damage: A review of current understanding and models, J. Nucl. Mater. 512 (2018) 450–479. https://doi.org/10.1016/j.jnucmat.2018.10.027.
[60] C.H. Woo, Theory of irradiation deformation in non-cubic metals: Effects of anisotropic diffusion, J. Nucl. Mater. 159 (1988) 237–256. https://doi.org/10.1016/0022-3115(88)90096-7.
[61] Y.N. Osetsky, D.J. Bacon, N. de Diego, Anisotropy of point defect diffusion in alpha-zirconium, Metall. Mater. Trans. A Phys. Metall. Mater. Sci. 33 (2002) 777–782. https://doi.org/10.1007/s11661-002-0144-z.
[62] G.D. Samolyuk, A.V. Barashev, S.I. Golubov, Y.N. Osetsky, R.E. Stoller, Analysis of the anisotropy of point defect diffusion in hcp Zr, Acta Mater. 78 (2014) 173–180. https://doi.org/10.1016/j.actamat.2014.06.024.
[63] J.F. March-Rico, G. Huang, B.D. Wirth, The effect of local chemical environment on the energetics of stacking faults and vacancy platelets in α-zirconium, J. Nucl. Mater. 540 (2020) 152339. https://doi.org/10.1016/j.jnucmat.2020.152339.
[64] L. Walters, S.R. Douglas, M. Griffiths, Equivalent Radiation Damage in Zirconium Irradiated in Various Reactors, ASTM STP 1597 (2018) 676–690. https://doi.org/10.1520/STP159720160101.
[65] C. Varvenne, O. Mackain, E. Clouet, Vacancy clustering in zirconium: An atomic-scale study, Acta Mater. 78 (2014) 65–77. https://doi.org/10.1016/j.actamat.2014.06.012.
[66] M. Griffiths, A review of microstructure evolution in zirconium alloys during irradiation, J. Nucl. Mater. 159 (1988) 190–218. https://doi.org/10.1016/0022-3115(88)90093-1.
[67] A. Jostsons, P.M. Kelly, R.G. Blake, The nature of dislocation loops in neutron irradiated zirconium, J. Nucl. Mater. 66 (1977) 236–256. https://doi.org/10.1016/0022-3115(77)90113-1.
[68] P.M. Kelly, R.G. Blake, The characterization of dislocation loops in neutron irradiated zirconium, Philos. Mag. 28 (1973) 415–426. https://doi.org/10.1080/14786437308217463.
[69] D.O. Northwood, R.W. Gilbert, L.E. Bahen, P.M. Kelly, R.G. Blake, A. Jostsons, P.K. Madden, D. Faulkner, W. Bell, R.B. Adamson, Characterization of neutron irradiation damage in zirconium alloys — an international “round-robin” experiment, J. Nucl. Mater. 79 (1979) 379–394. https://doi.org/10.1016/0022-3115(79)90103-X.
[70] D.O. Northwood, R.W. Gilbert, Some comments on damage alignment in neutron-irradiated zirconium alloys, J. Nucl. Mater. 51 (1974) 271–276. https://doi.org/10.1016/0022-3115(74)90015-4.
[71] A. Jostsons, R.G. Blake, J.G. Napier, P.M. Kelly, K. Farrell, Faulted loops in neutron-irradiated zirconium, J. Nucl. Mater. 68 (1977) 267–276. https://doi.org/10.1016/0022-3115(77)90251-3.

[72] C. Dai, L. Balogh, Z. Yao, M.R. Daymond, Atomistic simulations of the formation of <c>-type dislocation loops in α-zirconium, J. Nucl. Mater. 478 (2016) 125–134. https://doi.org/10.1016/j.jnucmat.2016.06.002.
[73] C. Dai, P. Saidi, M. Topping, L.K. Béland, Z. Yao, M.R. Daymond, A mechanism for basal vacancy loop formation in zirconium, Scr. Mater. 172 (2019) 72–76. https://doi.org/10.1016/j.scriptamat.2019.07.006.
[74] B. Christiaen, C. Domain, L. Thuinet, A. Ambard, A. Legris, A new scenario for ‹c› vacancy loop formation in zirconium based on atomic-scale modeling, Acta Mater. 179 (2019) 93–106. https://doi.org/10.1016/j.actamat.2019.07.030.
[75] R.A. Holt, R.W. Gilbert, 〈c〉 Component dislocations in annealed Zircaloy irradiated at about 570 K, J. Nucl. Mater. 137 (1986) 185–189. https://doi.org/10.1016/0022-3115(86)90218-7.
[76] S. Yagnik, R.B. Adamson, G. Kobylyansky, J.H. Chen, D. Gilbon, S. Ishimoto, T. Fukuda, L. Hallstadius, A. Obukhov, S. Mahmood, Effect of Alloying Elements, Cold Work, and Hydrogen on the Irradiation-Induced Growth Behavior of Zirconium Alloy Variants, ASTM STP 1597 (2018) 748–795. https://doi.org/10.1520/STP159720160040.
[77] Y. Li, N. Ghoniem, Cluster dynamics modeling of irradiation growth in single crystal Zr, J. Nucl. Mater. 540 (2020) 152312. https://doi.org/10.1016/j.jnucmat.2020.152312.
[78] B. Christiaen, C. Domain, L. Thuinet, A. Ambard, A. Legris, Influence of vacancy diffusional anisotropy: Understanding the growth of zirconium alloys under irradiation and their microstructure evolution, Acta Mater. 195 (2020) 631–644. https://doi.org/10.1016/j.actamat.2020.06.004.
[79] D.G. Franklin, R.B. Adamson, Implications of Zircaloy creep and growth to light water reactor performance, J. Nucl. Mater. 159 (1988) 12–21. https://doi.org/10.1016/0022-3115(88)90082-7.
[80] S. Valizadeh, G. Ledergerber, S. Abolhassani, D. Jädernäs, M. Dahlbäck, E.V. Mader, G. Zhou, J. Wright, L. Hallstadius, Effects of Secondary Phase Particle Dissolution on the in-Reactor Performance of BWR Cladding, ASTM STP 1529 (2011) 729–753. https://doi.org/10.1520/JAI103025.
[81] P.Y. Huang, S.T. Mahmood, R.B. Adamson, Effects of Thermomechanical Processing on In-Reactor Corrosion and Post-Irradiation Mechanical Properties of Zircaloy-2, ASTM STP 1295 (1996) 726–757. https://doi.org/10.1520/STP16199S.
[82] Y. Etoh, S. Shimada, Neutron irradiation effects on intermetallic precipitates in Zircaloy as a function of fluence, J. Nucl. Mater. 200 (1993) 59–69. https://doi.org/10.1016/0022-3115(93)90009-N.
[83] T. Sawabe, T. Sonoda, Evolution of nanoscopic iron clusters in irradiated zirconium alloys with different iron contents, J. Nucl. Sci. Technol. 55 (2018) 1110–1118. https://doi.org/10.1080/00223131.2018.1479987.
[84] T. Sawabe, T. Sonoda, An atom probe study on the Fe distribution in Zr-based alloys with different Fe content under high fluence neutron irradiation, J. Nucl. Mater. 567 (2022) 153809. https://doi.org/10.1016/j.jnucmat.2022.153809.
[85] A. Baris, S. Abolhassani, R. Grabherr, R. Restani, R. Schäublin, Y.L. Chiu, H.E. Evans, K. Ammon, M. Limbäck, Causes of Increased Corrosion and Hydrogen Uptake of Zircaloy-2 Cladding At High Burnups – a Comparative Study of the Chemical Composition of a 3 Cycle and a 9 Cycle Cladding, in: Proceedings of TopFuel, Prague, Czech Republic, ENS, 2018, A 0172.
[86] B.V. Cockeram, P.D. Edmondson, K.J. Leonard, B.F. Kammenzind, J.L. Hollenbeck, Atom probe examinations of Zircaloy irradiated at nominally 358 °C, Nucl. Mater. Energy 19 (2019) 416–432. https://doi.org/10.1016/j.nme.2019.03.023.
[87] B. Cox, Pellet-clad interaction (PCI) failures of zirconium alloy fuel cladding - A review, J. Nucl. Mater. 172 (1990) 249–292. https://doi.org/10.1016/0022-3115(90)90282-R.
[88] M. Dahlbäck, L. Hallstadius, M. Limbäck, G. Vesterlund, T. Andersson, P. Witt, J. Izquierdo, B. Remartinez, M. Díaz, J.L. Sacedon, A.M. Alvarez, U. Engman, R. Jakobsson, A.R. Massih, M. Billone, M. Elmoselhi, N. Yamashita, B. Cheng, The Effect of Liner Component Iron Content on Cladding Corrosion, Hydriding, and PCI Resistance, ASTM STP 1467 (2005) 873–895. https://doi.org/10.1520/stp37539s.
[89] P. Rudling, ANT International report: Zr Alloy Corrosion and Hydrogen Pickup, 2013. https://www.nrc.gov/docs/ML1525/ML15253A227.pdf.
[90] R. Stevens, An introduction to zirconia, 2nd ed., Magnesium Elektron, 1986.
[91] J. Godlewski, J. Gros, M. Lambertin, J. Wadier, H. Weidinger, Raman Spectroscopy Study of the Tetragonal-to-monoclinic Transition in Zirconium Oxide Scales and Determination of Overall Oxygen Diffusion by Nuclear Microanalysis of O, ASTM STP 1132 (1991) 416–436. https://doi.org/10.1520/stp25520s.
[92] B. Cox, Some thoughts on the mechanisms of in-reactor corrosion of zirconium alloys, J. Nucl. Mater.

336 (2005) 331–368. https://doi.org/10.1016/j.jnucmat.2004.09.029.
[93] P. Tejland, C. Langhammer, H.-O. Andrén, On the black oxide colour of zirconium alloys, J. Nucl. Mater. 400 (2010) 79–83. https://doi.org/10.1016/j.jnucmat.2010.02.013.
[94] V. Bouineau, A. Ambard, G. Bénier, D. Pêcheur, J. Godlewski, L. Fayette, T. Duverneix, A New Model to Predict the Oxidation Kinetics of Zirconium Alloys in a Pressurized Water Reactor, ASTM STP 1505 (2009) 405–429. https://doi.org/10.1520/JAI101312.
[95] E. Hillner, D.G. Franklin, J.D. Smee, Long-term corrosion of Zircaloy before and after irradiation, J. Nucl. Mater. 278 (2000) 334–345. https://doi.org/10.1016/S0022-3115(99)00230-5.
[96] D. Hudson, N. Ni, S. Lozano-Perez, D. Saxey, C. English, G.D.W. Smith, J. Sykes, C. Grovenor, The atomic scale structure and chemistry of the Zircaloy-4 metal-oxide interface, in: Proceedings of 14th International Conference on Environmental Degradation of Materials in Nuclear Power Systems, Virginia Beach, VA, August 23–27, 2009.
[97] P. Tejland, M. Thuvander, H.-O. Andrén, S. Ciurea, T. Andersson, M. Dahlbäck, L. Hallstadius, Detailed Analysis of the Microstructure of the Metal/Oxide Interface Region in Zircaloy-2 after Autoclave Corrosion Testing, ASTM STP 1529 (2011) 595–619. https://doi.org/10.1520/JAI102956.
[98] Y. Dong, A.T. Motta, E.A. Marquis, Atom probe tomography study of alloying element distributions in Zr alloys and their oxides, J. Nucl. Mater. 442 (2013) 270–281. https://doi.org/10.1016/j.jnucmat.2013.08.055.
[99] P. Tejland, H.-O. Andrén, Origin and effect of lateral cracks in oxide scales formed on zirconium alloys, J. Nucl. Mater. 430 (2012) 64–71. https://doi.org/10.1016/j.jnucmat.2012.06.039.
[100] P. Tejland, H.-O. Andrén, Oxidation induced localized creep deformation in Zircaloy-2, J. Nucl. Mater. 444 (2014) 30–34. https://doi.org/10.1016/j.jnucmat.2013.09.020.
[101] A. Garner, F. Baxter, P. Frankel, M. Topping, A. Harte, T. Slater, P. Tejland, J.E. Romero, E.C. Darby, A. Cole-Baker, M. Gass, M. Preuss, Investigating the Effect of Zirconium Oxide Microstructure on Corrosion Performance: A Comparison between Neutron, Proton, and Nonirradiated Oxides, ASTM STP 1597 (2018) 491–523. https://doi.org/10.1520/stp159720160069.
[102] A. Baris, S. Abolhassani, Y.L. Chiu, H.E. Evans, Observation of crack microstructure in oxides and its correlation to oxidation and hydrogen-uptake by 3D FIB Tomography — case of Zr-ZrO2 in reactor, Mater. High Temp. 35 (2018) 14–21. https://doi.org/10.1080/09603409.2017.1392412.
[103] S. Abolhassani, A. Baris, R. Grabherr, J. Hawes, A. Colldeweih, R. Vanta, R. Restani, A. Hermann, J. Bertsch, M. Chollet, G. Kuri, M. Martin, S. Portier, H. Wiese, H. Schweikert, G. Bart, K. Ammon, G. Ledergerber, M. Limbäck, Toward an Improved Understanding of the Mechanisms Involved in the Increased Hydrogen Uptake and Corrosion at High Burnups in Zirconium Based Claddings, ASTM STP1622 (2021) 435–466. https://doi.org/https://doi.org/10.1520/STP162220190052.
[104] IAEA, Increased local corrosion of SVEA-96 fuel assemblies in KKL. Final report, 2001.
[105] W.J. Marble, An Overview of Zinc Addition for BWR Dose Rate Control, in: T.A. Khan (Ed.), Proceedings of Third International Workshop on Implementation of ALARA in Nuclear Power Plants, USNRC, 1995, pp. 67–84.
[106] D. Pêcheur, F. Lefebvre, A.T. Motta, C. Lemaignan, J.F. Wadier, Precipitate evolution in the Zircaloy-4 oxide layer, J. Nucl. Mater. 189 (1992) 318–332. https://doi.org/10.1016/0022-3115(92)90385-X.
[107] G. Sundell, M. Thuvander, H.-O. Andrén, Enrichment of Fe and Ni at metal and oxide grain boundaries in corroded Zircaloy-2, Corros. Sci. 65 (2012) 10–12. https://doi.org/10.1016/j.corsci.2012.08.061.
[108] J. Romero, L. Hallstadius, M. Owaki, G. Pan, K. Kataoka, K. Kakiuchi, R.J. Comstock, J. Partezana, A. Mueller, M. Dahlbäck, A. Garde, A. Atwood, M. Åslund, Evolution of Westinghouse Fuel Cladding, in: Proceedings of WRFPM/TopFuel, Sendai, Japan, Sept. 14–17, 2014.
[109] P. Bossis, D. Pêcheur, K. Hanift, J. Thomazet, M. Blat, S. Yagnik, K.Y. Suk, Comparison of the High Burn-Up Corrosion on M5 and Low Tin Zircaloy-4, ASTM STP 1467 (2005) 494–525. https://doi.org/10.1520/JAI12404.
[110] M. Preuss, P. Frankel, S. Lozano-Perez, D. Hudson, E. Polatidis, N. Ni, J. Wei, C. English, S. Storer, K.B. Chong, M. Fitzpatrick, P. Wang, J. Smith, C. Grovenor, G. Smith, J. Sykes, B. Cottis, S. Lyon, L. Hallstadius, B. Comstock, A. Ambard, M. Blat-Yrieix, Studies Regarding Corrosion Mechanisms in Zirconium Alloys, ASTM STP 1529 (2011) 649–681. https://doi.org/10.1520/JAI103246.
[111] G. Sundell, M. Thuvander, H.-O. Andrén, Tin clustering and precipitation in the oxide during autoclave corrosion of Zircaloy-2, J. Nucl. Mater. 456 (2015) 409–414. https://doi.org/10.1016/j.jnucmat.2014.10.003.
[112] M. Lindgren, G. Sundell, I. Panas, L. Hallstadius, M. Thuvander, H.-O. Andrén, Toward a Comprehensive Mechanistic Understanding of Hydrogen Uptake in Zirconium Alloys by Combining Atom Probe Analysis

With Electronic Structure Calculations, ASTM STP 1543 (2015) 515–539. https://doi.org/10.1520/stp154320120164.
[113] G.P. Sabol, G. Kilp, M. Balfour, E. Roberts, Development of a Cladding Alloy for High Burnup, ASTM STP 1023 (1989) 227–244. https://doi.org/10.1520/STP18868S.
[114] M. Christensen, W. Wolf, C. Freeman, E. Wimmer, R.B. Adamson, L. Hallstadius, P.E. Cantonwine, E.V. Mader, H in $\alpha$-Zr and in zirconium hydrides: Solubility, effect on dimensional changes, and the role of defects, J. Phys. Condens. Matter 27 (2015) 025402. https://doi.org/10.1088/0953-8984/27/2/025402.
[115] J. Bair, M. Asle Zaeem, M. Tonks, A review on hydride precipitation in zirconium alloys, J. Nucl. Mater. 466 (2015) 12–20. https://doi.org/10.1016/j.jnucmat.2015.07.014.
[116] K. Une, S. Ishimoto, Y. Etoh, K. Ito, K. Ogata, T. Baba, K. Kamimura, Y. Kobayashi, The terminal solid solubility of hydrogen in irradiated Zircaloy-2 and microscopic modeling of hydride behavior, J. Nucl. Mater. 389 (2009) 127–136. https://doi.org/10.1016/j.jnucmat.2009.01.017.
[117] A. McMinn, E.C. Darby, J.S. Schofieid, The Terminal Solid Solubility of Hydrogen in Zirconium Alloys, ASTM STP 1354 (2000) 173–195. https://doi.org/10.1520/stp14300s.
[118] P. Vizcaíno, A.D. Banchik, J.P. Abriata, Solubility of hydrogen in Zircaloy-4: Irradiation induced increase and thermal recovery, J. Nucl. Mater. 304 (2002) 96–106. https://doi.org/10.1016/S0022-3115(02)00883-8.
[119] M. Christensen, W. Wolf, C.M. Freeman, E. Wimmer, R.B. Adamson, L. Hallstadius, P.E. Cantonwine, E.V. Mader, Effect of alloying elements on the properties of Zr and the Zr–H system, J. Nucl. Mater. 445 (2014) 241–250. https://doi.org/10.1016/j.jnucmat.2013.10.040.
[120] J. Blomqvist, J. Olofsson, A.M. Alvarez, C. Bjerkén, Structure and thermodynamical properties of zirconium hydrides from first-principle, 15th Int. Conference on Environmental Degradation of Materials in Nuclear Power Systems–Water Reactors (2011) 635–643. https://doi.org/10.1007/978-3-319-48760-1_42.
[121] J. Zheng, X. Zhou, L. Mao, H. Zhang, J. Liang, L. Sheng, S. Peng, First-principles study of the relative stability of various zirconium hydrides using the special quasirandom structures approach, Int. J. Hydrogen Energy 40 (2015) 4597–4604. https://doi.org/10.1016/j.ijhydene.2015.02.045.
[122] Z. Zhao, M. Blat-Yrieix, J.P. Morniroli, A. Legris, L. Thuinet, Y. Kihn, A. Ambard, L. Legras, Characterization of Zirconium Hydrides and Phase Field Approach to a Mesoscopic-Scale Modeling of their Precipitation, ASTM STP 1505 (2009) 29–50. https://doi.org/10.1520/JAI101161.
[123] E. Zuzek, J.P. Abriata, A. San-Martin, F.D. Manchester, The H-Zr (Hydrogen-Zirconium) System, Bull. Alloy Phase Diagrams 11 (1990) 385–395. https://doi.org/10.1007/BF02843318.
[124] J. Goldak, L.T. Lloyd, C.S. Barrett, Lattice Parameters, Thermal Expansions, and Grüneisen Coefficients of Zirconium, 4.2 to 1130°K, Phys. Rev. 144 (1966) 478–484. https://doi.org/10.1103/PhysRev.144.478.
[125] S.S. Sidhu, N.S. Satya Murthy, F.P. Campos, D.D. Zauberis, Neutron and X-Ray Diffraction Studies of Nonstoichiometric Metal Hydrides, Adv. Chemsitry 39 (1963) 87–98. https://doi.org/10.1021/ba-1964-0039.ch008.
[126] S. Yamanaka, K. Yamada, K. Kurosaki, M. Uno, K. Takeda, H. Anada, T. Matsuda, S. Kobayashi, Characteristics of zirconium hydride and deuteride, J. Alloys Compd. 330–332 (2002) 99–104. https://doi.org/10.1016/S0925-8388(01)01448-7.
[127] K. Niedźwiedź, B. Nowak, O.J. Zogał, 91Zr NMR in non-stoichiometric zirconium hydrides, ZrHx ($1.55 \leq x \leq 2$), J. Alloys Compd. 194 (1993) 47–51. https://doi.org/10.1016/0925-8388(93)90643-2.
[128] H.H. Shen, X.T. Zu, B. Chen, C.Q. Huang, K. Sun, Direct observation of hydrogenation and dehydrogenation of a zirconium alloy, J. Alloys Compd. 659 (2016) 23–30. https://doi.org/10.1016/j.jallcom.2015.11.031.
[129] S.M. Hanlon, S.Y. Persaud, F. Long, A. Korinek, M.R. Daymond, A solution to FIB induced artefact hydrides in Zr alloys, J. Nucl. Mater. 515 (2019) 122–134. https://doi.org/10.1016/j.jnucmat.2018.12.020.
[130] B. Gault, M.P. Moody, J.M. Cairney, S.P. Ringer, Atom Probe Microscopy, Springer, 2012. https://doi.org/10.1007/978-1-4614-3436-8.
[131] D.J. Larson, T.J. Prosa, R.M. Ulfig, B.P. Geiser, T.F. Kelly, Local Electrode Atom Probe Tomography, Springer, 2013. https://doi.org/10.1007/978-1-4614-8721-0.
[132] M.K. Miller, R.G. Forbes, Atom-probe tomography: The local electrode atom probe, Springer, 2014. https://doi.org/10.1007/978-1-4899-7430-3.
[133] D.B. Williams, C.B. Carrter, Transmission Electron Micrsocopy, 2nd ed., Springer, New York, 2009.
[134] T. Prosa, D. Lenz, I. Martin, D. Reinhard, D. Larson, J. Bunton, Evaporation-Field Differences with Deep-UV Atom Probe Tomography, Microsc. Microanal. 27 (S1) (2021) 1262–1264.

https://doi.org/10.1017/s1431927621004736.
[135] Cameca. LEAP 6000 XR. https://www.cameca.com/products/apt/leap-6000. Retrieved 3 August, (2022).
[136] P. Bas, A. Bostel, B. Deconihout, D. Blavette, A general protocol for the reconstruction of 3D atom probe data, Appl. Surf. Sci. 87–88 (1995) 298–304. https://doi.org/10.1016/0169-4332(94)00561-3.
[137] W.H. Miller, A Treatise on Crystallography, J. & J. J. Deighton, 1839.
[138] A.R. Waugh, E.D. Boyes, M.J. Southon, Investigations of field evaporation with a field-desorption microscope, Surf. Sci. 61 (1976) 109–142. https://doi.org/10.1016/0039-6028(76)90411-8.
[139] M.P. Moody, B. Gault, L.T. Stephenson, D. Haley, S.P. Ringer, Qualification of the tomographic reconstruction in atom probe by advanced spatial distribution map techniques, Ultramicroscopy 109 (2009) 815–824. https://doi.org/10.1016/j.ultramic.2009.03.016.
[140] J.M. Hyde, C.A. English, An Analysis of the Structure of Irradiation induced Cu-enriched Clusters in Low and High Nickel Welds, MRS Online Proc. Libr. 650 (2000) 66. https://doi.org/10.1557/PROC-650-R6.6.
[141] D. Vaumousse, A. Cerezo, P.J. Warren, A procedure for quantification of precipitate microstructures from three-dimensional atom probe data, Ultramicroscopy 95 (2003) 215–221. https://doi.org/10.1016/S0304-3991(02)00319-4.
[142] M. Ester, H.-P. Kriegel, J. Sander, X. Xu, A Density-Based Algorithm for Discovering Clusters in Large Spatial Databases with Noise, in: KDD-96, AAAI, 1996.
[143] O.C. Hellman, J.A. Vandenbroucke, J. Rüsing, D. Isheim, D.N. Seidman, Analysis of Three-dimensional Atom-probe Data by the Proximity Histogram, Microsc. Microanal. 6 (2000) 437–444. https://doi.org/10.1007/s100050010051.
[144] K. Lindgren, K. Stiller, P. Efsing, M. Thuvander, On the Analysis of Clustering in an Irradiated Low Alloy Reactor Pressure Vessel Steel Weld, Microsc. Microanal. 23 (2017) 376–384. https://doi.org/10.1017/S1431927617000162.
[145] A. Shariq, S. Mutas, K. Wedderhoff, C. Klein, H. Hortenbach, S. Teichert, P. Kücher, S.S.A. Gerstl, Investigations of field-evaporated end forms in voltage- and laser-pulsed atom probe tomography, Ultramicroscopy 109 (2009) 472–479. https://doi.org/10.1016/j.ultramic.2008.10.001.
[146] B. Gault, Y.M. Chen, M.P. Moody, T. Ohkubo, K. Hono, S.P. Ringer, Influence of the wavelength on the spatial resolution of pulsed-laser atom probe, J. Appl. Phys. 110 (2011). https://doi.org/10.1063/1.3657846.
[147] F. Meisenkothen, E.B. Steel, T.J. Prosa, K.T. Henry, R.P. Kolli, Effects of detector dead-time on quantitative analyses involving boron and multi-hit detection events in atom probe tomography, Ultramicroscopy 159 (2015) 101–111. https://doi.org/10.1016/j.ultramic.2015.07.009.
[148] Z. Peng, P.-P. Choi, B. Gault, D. Raabe, Evaluation of Analysis Conditions for Laser-Pulsed Atom Probe Tomography: Example of Cemented Tungsten Carbide, Microsc. Microanal. 23 (2017) 431–442. https://doi.org/10.1017/S1431927616012654.
[149] P.H. Clifton, T.J. Gribb, S.S.A. Gerstl, R.U. Ulfig, D.J. Larson, Performance Advantages of a Modern, Ultra-High Mass Resolution Atom Probe, Microsc. Microanal. 14 (2008) 454–455. https://doi.org/10.1017/S1431927608087217.
[150] L.A. Currie, Limits for Qualitative Detection and Quantitative Determination: Application to Radiochemistry, Anal. Chem. 40 (1968) 586–593. https://doi.org/10.1021/ac60259a007.
[151] A. La Fontaine, S. Piazolo, P. Trimby, L. Yang, J.M. Cairney, Laser-Assisted Atom Probe Tomography of Deformed Minerals: A Zircon Case Study, Microsc. Microanal. 23 (2017) 404–413. https://doi.org/10.1017/S1431927616012745.
[152] D. Haley, A.J. London, M.P. Moody, Processing APT Spectral Backgrounds for Improved Quantification, Microsc. Microanal. 26 (2020) 964–977. https://doi.org/10.1017/S1431927620024290.
[153] J.M. Hyde, M.G. Burke, B. Gault, D.W. Saxey, P. Styman, K.B. Wilford, T.J. Williams, Atom probe tomography of reactor pressure vessel steels: An analysis of data integrity, Ultramicroscopy 111 (2011) 676–682. https://doi.org/10.1016/j.ultramic.2010.12.033.
[154] D. Hudson, A. Cerezo, G.D.W. Smith, Zirconium oxidation on the atomic scale, Ultramicroscopy 109 (2009) 667–671. https://doi.org/10.1016/j.ultramic.2008.10.020.
[155] D. Hudson, G.D.W. Smith, B. Gault, Optimisation of mass ranging for atom probe microanalysis and application to the corrosion processes in Zr alloys, Ultramicroscopy 111 (2011) 480–486. https://doi.org/10.1016/j.ultramic.2010.11.007.
[156] C.R.M. Grovenor, N. Ni, D. Hudson, S.S. Yardley, K.L. Moore, G.D.W. Smith, S. Lozano-Perez, J.M. Sykes, Mechanisms of Oxidation of Fuel Cladding Alloys Revealed by High Resolution APT, TEM and SIMS Analysis, in: Mater. Res. Soc. Symp. Proceedings, 2012. https://doi.org/10.1557/opl.2012.521.

[157] N. Ni, D. Hudson, J. Wei, P. Wang, S. Lozano-Perez, G.D.W. Smith, J.M. Sykes, S.S. Yardley, K.L. Moore, S. Lyon, R. Cottis, M. Preuss, C.R.M. Grovenor, How the crystallography and nanoscale chemistry of the metal/oxide interface develops during the aqueous oxidation of zirconium cladding alloys, Acta Mater. 60 (2012) 7132–7149. https://doi.org/10.1016/j.actamat.2012.09.021.
[158] B.V. Cockeram, K.J. Leonard, L.L. Snead, M.K. Miller, The use of a laser-assisted Local Electrode Atom Probe and TEM to examine the microstructure of Zircaloy and precipitate structure following low dose neutron irradiation at nominally 358 °C, J. Nucl. Mater. 433 (2013) 460–478. https://doi.org/10.1016/j.jnucmat.2012.10.006.
[159] J. Wei, P. Frankel, E. Polatidis, M. Blat, A. Ambard, R.J. Comstock, L. Hallstadius, D. Hudson, G.D.W. Smith, C.R.M. Grovenor, M. Klaus, R.A. Cottis, S. Lyon, M. Preuss, The effect of Sn on autoclave corrosion performance and corrosion mechanisms in Zr-Sn-Nb alloys, Acta Mater. 61 (2013) 4200–4214. https://doi.org/10.1016/j.actamat.2013.03.046.
[160] T. Sawabe, T. Sonoda, S. Kitajima, Distribution of alloying elelments in irradiated Zircaloy-2 by atom probe tomography and transmission electron microscopy, in: Proceedings of WRFPM/TopFuel 2014, Sendai, Japan, Sep- 14–17, 2014, Pap. No. 100139.
[161] P. Tejland, H.-O. Andrén, G. Sundell, M. Thuvander, B. Josefsson, L. Hallstadius, M. Ivermark, M. Dahlbäck, Oxidation Mechanism in Zircaloy-2—The Effect of SPP Size Distribution, ASTM STP 1543 (2015) 373–403. https://doi.org/10.1520/stp154320130052.
[162] T. Sawabe, T. Sonoda, S. Kitajima, Analysis method of matrix and second phase particles in Zircaloy-2 by atom probe tomography, Prog. Nucl. Energy 82 (2015) 159–164. https://doi.org/10.1016/j.pnucene.2014.07.012.
[163] G. Sundell, M. Thuvander, A.K. Yatim, H. Nordin, H.-O. Andrén, Direct observation of hydrogen and deuterium in oxide grain boundaries in corroded Zirconium alloys, Corros. Sci. 90 (2015) 1–4. https://doi.org/10.1016/j.corsci.2014.10.016.
[164] B. De Gabory, Y. Dong, A.T. Motta, E.A. Marquis, EELS and atom probe tomography study of the evolution of the metal/oxide interface during zirconium alloy oxidation, J. Nucl. Mater. 462 (2015) 304–309. https://doi.org/10.1016/j.jnucmat.2015.03.043.
[165] P.A. Burr, M.R. Wenman, B. Gault, M.P. Moody, M. Ivermark, M.J.D. Rushton, M. Preuss, L. Edwards, R.W. Grimes, From solid solution to cluster formation of Fe and Cr in α-Zr, J. Nucl. Mater. 467 (2015) 320–331. https://doi.org/10.1016/j.jnucmat.2015.10.001.
[166] G. Sundell, M. Thuvander, H.-O. Andrén, Barrier oxide chemistry and hydrogen pick-up mechanisms in zirconium alloys, Corros. Sci. 102 (2016) 490–502. https://doi.org/10.1016/j.corsci.2015.11.002.
[167] J. Hu, B. Setiadinata, T. Aarholt, A. Garner, A. Vilalta-Clemente, J.M. Partezana, P. Frankel, P. Bagot, S. Lozano-Perez, A. Wilkinson, M. Preuss, M. Moody, C. Grovenor, Understanding Corrosion and Hydrogen Pickup of Zirconium Fuel Cladding Alloys: The Role of Oxide Microstructure, Porosity, Suboxides, and Second-Phase Particles, ASTM STP 1597 (2018) 93–126. https://doi.org/10.1520/STP159720160071.
[168] A.J. Breen, I. Mouton, W. Lu, S. Wang, A. Szczepaniak, P. Kontis, L.T. Stephenson, Y. Chang, A.K. da Silva, C.H. Liebscher, D. Raabe, T.B. Britton, M. Herbig, B. Gault, Atomic scale analysis of grain boundary deuteride growth front in Zircaloy-4, Scr. Mater. 156 (2018) 42–46. https://doi.org/10.1016/j.scriptamat.2018.06.044.
[169] A. Harte, R.P. Babu, C.A. Hirst, T.L. Martin, P.A.J. Bagot, M.P. Moody, P. Frankel, J. Romero, L. Hallstadius, E.C. Darby, M. Preuss, Understanding irradiation-induced nanoprecipitation in zirconium alloys using parallel TEM and APT, J. Nucl. Mater. 510 (2018) 460–471. https://doi.org/10.1016/j.jnucmat.2018.08.033.
[170] I. Mouton, A.J. Breen, S. Wang, Y. Chang, A. Szczepaniak, P. Kontis, L.T. Stephenson, D. Raabe, M. Herbig, T.B. Britton, B. Gault, Quantification Challenges for Atom Probe Tomography of Hydrogen and Deuterium in Zircaloy-4, Microsc. Microanal. 25 (2019) 481–488. https://doi.org/10.1017/S143192761801615X.
[171] E. Francis, R.P. Babu, A. Harte, T.L. Martin, P. Frankel, D. Jädernäs, J. Romero, L. Hallstadius, P.A.J. Bagot, M.P. Moody, M. Preuss, Effect of Nb and Fe on damage evolution in a Zr-alloy during proton and neutron irradiation, Acta Mater. 165 (2019) 603–614. https://doi.org/10.1016/j.actamat.2018.12.021.
[172] B. Tao, B. Luan, R. Qiu, Q. Fang, L. Cao, Y. Liu, X. Zhang, R. Liu, Q. Liu, Analysis of atomic distribution near grain boundary in Zr–Sn–Nb–Fe-(Cu) alloys by atom probe tomography, J. Nucl. Mater. 515 (2019) 135–139. https://doi.org/10.1016/j.jnucmat.2018.12.033.
[173] Z. Yu, A. Couet, M. Bachhav, Irradiation-induced Nb redistribution of ZrNb alloy: An APT study, J. Nucl.

Mater. 516 (2019) 100–110. https://doi.org/10.1016/j.jnucmat.2019.01.015.
[174] J. Hu, T. Aarholt, B. Setiadinata, K. Li, A. Garner, S. Lozano-Perez, M. Moody, P. Frankel, M. Preuss, C. Grovenor, A multi-technique study of “barrier layer” nano-porosity in Zr oxides during corrosion and hydrogen pickup using (S)TEM, TKD, APT and NanoSIMS, Corros. Sci. 158 (2019) 108109. https://doi.org/10.1016/j.corsci.2019.108109.
[175] S. Xie, B. Zhou, X. Liang, Q. Li, W. Liu, M. Yao, J. Zhang, The Distribution of Li Ions in the Oxide Film Formed on Zircaloy-4 Corroded in Lithiated Water at 633 K, Materials 13 (2020) 873. https://doi.org/10.3390/ma13040873.
[176] Z. Yu, T. Kim, M. Bachhav, X. Liu, L. He, A. Couet, Effect of proton pre-irradiation on corrosion of Zr-0.5Nb model alloys with different Nb distributions, Corros. Sci. 173 (2020) 108790. https://doi.org/10.1016/j.corsci.2020.108790.
[177] E.J. Kautz, B. Gwalani, S.V.M. Lambeets, L. Kovarik, D.K. Schreiber, D.E. Perea, D. Senor, Y.-S. Liu, A.K. Battu, K.-P. Tseng, S. Thevuthasan, A. Devaraj, Rapid assessment of structural and compositional changes during early stages of zirconium alloy oxidation, NPJ Mater. Degrad. 4 (2020) 29. https://doi.org/10.1038/s41529-020-00133-6.
[178] I. Mouton, Y. Chang, P. Chakraborty, S. Wang, L.T. Stephenson, T.B. Britton, B. Gault, Hydride growth mechanism in zircaloy-4: Investigation of the partitioning of alloying elements, Materialia 15 (2021) 101006. https://doi.org/10.1016/j.mtla.2021.101006.
[179] S.B. Adisa, J. Hu, M.J. Swenson, APT characterization and modeling of irradiation-induced Nb-rich nanoclustering in Zr-1.0%Nb alloys, Materialia 16 (2021) 101040. https://doi.org/10.1016/j.mtla.2021.101040.
[180] J. Eriksson, G. Sundell, P. Tejland, H.-O. Andrén, M. Thuvander, An atom probe tomography study of the chemistry of radiation-induced dislocation loops in Zircaloy-2 exposed to boiling water reactor operation, J. Nucl. Mater. 550 (2021) 152923. https://doi.org/10.1016/j.jnucmat.2021.152923.
[181] Z. Yu, M. Bachhav, F. Teng, L. He, A. Couet, Nanoscale redistribution of alloying elements in high-burnup AXIOM-2 (X2®) and their effects on in-reactor corrosion, Corros. Sci. 190 (2021) 109652. https://doi.org/10.1016/j.corsci.2021.109652.
[182] A. Callow, Atom Probe Tomography of Irradiated Zirconium Alloys, PhD thesis, University of Oxford, 2021.
[183] K. Clark, Using Advanced Correlative Microscopy Techniques to Investigate the Behaviour of Zirconium Alloys, PhD thesis, University of Bristol, 2021.
[184] J. Liu, G. He, A. Callow, K. Li, S. Lozano-Perez, A.J. Wilkinson, M. Moody, C.R.M. Grovenor, J. Hu, M. Kirk, M. Li, A.H. Mir, J. Hinks, S. Donnelly, J.M. Partezana, H.M. Nordin, Ex Situ and In Situ Studies of Radiation Damage Mechanisms in Zr-Nb Alloys, ASTM STP 1622 (2021) 408–434. https://doi.org/10.1520/stp162220190016.
[185] Z. Yu, M. Moorehead, L. Borrel, J. Hu, M. Bachhav, A. Couet, Fundamental Understanding of Nb Effect on Corrosion Mechanisms of Irradiated Zr-Nb Alloys, ASTM STP 1622 (2021) 669–695. https://doi.org/10.1520/stp162220190021.
[186] P. Wang, J. Bowman, M. Bachhav, B. Kammenzind, R. Smith, J. Carter, A. Motta, E. Lacroix, G. Was, Emulation of neutron damage with proton irradiation and its effects on microstructure and microchemistry of Zircaloy-4, J. Nucl. Mater. 557 (2021) 153281. https://doi.org/10.1016/j.jnucmat.2021.153281.
[187] M.E. Jones, A.J. London, A.J. Breen, P.D. Styman, S. Sikotra, M.P. Moody, D. Haley, Improving the Quantification of Deuterium in Zirconium Alloy Atom Probe Tomography Data Using Existing Analysis Methods, Microscopy and Microanalysis (2021) 1245–1254. https://doi.org/10.1017/S1431927621012848.
[188] B.M. Jenkins, J. Haley, M.P. Moody, J.M. Hyde, C.R.M. Grovenor, APT and TEM study of behaviour of alloying elements in neutron-irradiated zirconium-based alloys, Scr. Mater. 208 (2022) 114323. https://doi.org/10.1016/j.scriptamat.2021.114323.
[189] A. Fazi, K. Stiller, H.-O. Andrén, M. Thuvander, Cold sprayed Cr-coating on Optimized ZIRLO™ claddings: the Cr/Zr interface and its microstructural and chemical evolution after autoclave corrosion testing, J. Nucl. Mater. 560 (2022) 153505. https://doi.org/10.1016/j.jnucmat.2022.153505.
[190] J. Eriksson, G. Sundell, P. Tejland, H.-O. Andrén, M. Thuvander, Nanoscale chemistry of Zircaloy-2 exposed to three and nine annual cycles of boiling water reactor operation — an atom probe tomography study, J. Nucl. Mater. 561 (2022) 153537. https://doi.org/10.1016/j.jnucmat.2022.153537.
[191] J. Eriksson, D. Mayweg, G. Sundell, H.-O. Andrén, M. Thuvander, Solute Concentrations in the Matrix of Zirconium Alloys Studied by Atom Probe Tomography, Accepted for Publication in ASTM STP1645

(2022).
[192] P. Chakraborty, I. Mouton, B. Gault, A. Tehranchi, J. Neugebauer, T. Hickel, Effect of Sn on generalized stacking fault energy surfaces in zirconium and its hydrides, https://arxiv.org/pdf/2209.09147.pdf (2022).
[193] H.-O. Andrén, L. Mattsson, U. Rolander, Atom-Pobe Analysis of Zircaloy, Le J. Phys. Colloq. 47 (1986) C2-191–C2-196. https://doi.org/10.1051/jphyscol:1986228.
[194] B. Wadman, U. Rolander, H.-O. Andrén, Matrix Composition of Zircaloy-4, Le J. Phys. Colloq. C6. 48 (1987) C6-299–C6-304. https://doi.org/10.1051/jphyscol:1987649.
[195] B. Wadman, H.-O. Andrén, U. Rolander, Preferential Field Evaporation During Atom Probe Analysis of Zircaloy-4, Le J. Phys. Colloq. 49 (1988) C6-323–C6-327. https://doi.org/10.1051/jphyscol:1988656.
[196] B. Wadman, H.-O. Andrén, L.K.L. Falk, Atom Probe Analysis of Thin Oxide Layers on Zircaloy Needles, Le J. Phys. Colloq. 50 (1989) C8-303-C8-308. https://doi.org/10.1051/jphyscol:1989851.
[197] B. Wadman, H.-O. Andrén, Direct Measurement of Matrix Composition in Zircaloy-4 by Atom Probe Microanalysis, ASTM STP 1023 (1989) 423–434. https://doi.org/10.1520/stp18879s.
[198] B. Wadman, H.-O. Andrén, A.-L. Nyström, P. Rudling, H. Pettersson, Microstructural influence on uniform corrosion of Zircaloy nuclear fuel claddings, J. Nucl. Mater. 200 (1993) 207–217. https://doi.org/10.1016/0022-3115(93)90331-R.
[199] N. Sano, K. Takeda, Atom probe analysis of Sn in Zr-based alloys, J. Nucl. Mater. 252 (1998) 63–70. https://doi.org/10.1016/S0022-3115(97)00302-4.
[200] D.R. Kingham, The post-ionization of field evaporated ions: A theoretical explanation of multiple charge states, Surf. Sci. 116 (1982) 273–301. https://doi.org/10.1016/0039-6028(82)90434-4.
[201] J. Orloff, M. Utlaut, L. Swanson, High Resolution Focused Ion Beams: FIB and its Applications, Springer, 2003.
[202] K. Thompson, D. Lawrence, D.J. Larson, J.D. Olson, T.F. Kelly, B. Gorman, In situ site-specific specimen preparation for atom probe tomography, Ultramicroscopy 107 (2007) 131–139. https://doi.org/10.1016/j.ultramic.2006.06.008.
[203] T. Andersson, T. Thorvaldsson, A. Wilson, A.M. Wardle, Influence of thermal processing and microstructure on the corrosion behaviour of Zircaloy-4 tubing, in: Improvements of Water Reactor Fuel Technology and Utilization, IAEA-SM-288/59, IAEA, Vienna, Austria, 1987: pp. 435–449.
[204] P. Tägtström, M. Limbäck, M. Dahlbäck, T. Andersson, H. Pettersson, Effects of Hydrogen Pickup and Second-Phase Particle Dissolution on the In-Reactor Corrosion Performance of BWR Claddings, ASTM STP 1423 (2002) 96–118. https://doi.org/10.1520/stp11385s.
[205] G. Ledergerber, W. Kaufmann, A. Ritter, D. Greiner, Y. Parmar, R. Jacot-Guillarmod, J. Krouthén, Burnup increase and Power Uprate - Operation history of KKL, in Proceedings of International LWR Fuel Performance Meeting, San Francisco, California, Sept. 30–Oct. 3, 2007, Paper 1036.
[206] G. Ledergerber, S. Abolhassani, M. Limbäck, R.J. Lundmark, K.-Å. Magnusson, Characterization of High Burnup Fuel for Safety Related Fuel Testing, J. Nucl. Sci. Technol. 43 (2006) 1006–1014. https://doi.org/10.1080/18811248.2006.9711189.
[207] G. Kuri, C. Degueldre, J. Bertsch, S. Abolhassani, Micro-focussed XAFS spectroscopy to study Ni-bearing precipitates in the metal of corroded Zircaloy-2, Appl. Phys. A Mater. Sci. Process. 98 (2010) 625–633. https://doi.org/10.1007/s00339-009-5456-z.
[208] G. Ledergerber, S. Valizadeh, J. Wright, M. Limbäck, L. Hallstadius, D. Gavillet, S. Abolhassani, F. Nagase, T. Sugiyama, W. Wiesenack, T. Tverberg, Fuel performance beyond design – Exploring the limits, in: Proceedings of LWR Fuel Performance Meeting/TopFuel/WRFPM, Orlando, Florida, USA, 2010, pp. 513–524.
[209] S. Abolhassani, G. Bart, J. Bertsch, M. Grosse, L. Hallstadius, A. Hermann, G. Kuri, G. Ledergerber, C. Lemaignan, M. Martin, S. Portier, C. Proff, R. Restani, S. Valance, S. Valizadeh, H. Wiese, Corrosion and Hydrogen Uptake in Zirconium Claddings Irradiated in Light Water Reactors, ASTM STP 1543 (2015) 540–573. https://doi.org/10.1520/STP154320130007.
[210] A. Harte, T. Seymour, E.M. Francis, P. Frankel, S.P. Thompson, D. Jädernäs, J. Romero, L. Hallstadius, M. Preuss, Advances in synchrotron x-ray diffraction and transmission electron microscopy techniques for the investigation of microstructure evolution in proton- and neutron-irradiated zirconium alloys, J. Mater. Res. 30 (2015) 1349–1365. https://doi.org/10.1557/jmr.2015.65.
[211] V. Brankov, G. Khvostov, K. Mikityuk, A. Pautz, R. Restani, S. Abolhassani, G. Ledergerber, W. Wiesenack, Analysis of effects of pellet-cladding bonding on trapping of the released fission gases in high burnup KKL BWR fuels, Nucl. Eng. Des. 305 (2016) 559–568. https://doi.org/10.1016/j.nucengdes.2016.06.021.

[212] T. Seymour, P. Frankel, L. Balogh, T. Ungár, S.P. Thompson, D. Jädernäs, J. Romero, L. Hallstadius, M.R. Daymond, G. Ribárik, M. Preuss, Evolution of dislocation structure in neutron irradiated Zircaloy-2 studied by synchrotron x-ray diffraction peak profile analysis, Acta Mater. 126 (2017) 102–113. https://doi.org/10.1016/j.actamat.2016.12.031.
[213] G. Kuri, H. Ramanantoanina, J. Bertsch, M. Martin, I. Panas, Chemical state and atomic scale environment of nickel in the corrosion layer of irradiated Zircaloy-2 at a burn-up around 45 MWd/kg, Corros. Sci. 143 (2018) 200–211. https://doi.org/10.1016/j.corsci.2018.08.032.
[214] M. Chollet, S. Valance, S. Abolhassani, G. Stein, D. Grolimund, M. Martin, J. Bertsch, Synchrotron X-ray diffraction investigations on strains in the oxide layer of an irradiated Zircaloy fuel cladding, J. Nucl. Mater. 488 (2017) 181–190. https://doi.org/10.1016/j.jnucmat.2017.03.010.
[215] P. Magnusson, A.-M. Alvarez-Holston, K. Ammon, G. Ledergerber, M. Nilsson, D. Schrire, K. Nissen, J. Wright, Effects of Zr-hydride distribution of irradiated Zircaloy-2 cladding in RIA-simulating pellet-clad mechanical interaction testing, Nucl. Eng. Technol. 50 (2018) 246–252. https://doi.org/10.1016/j.net.2017.12.013.
[216] A.W. Colldeweih, A. Baris, P. Spätig, S. Abolhassani, Evaluation of mechanical properties of irradiated zirconium alloys in the vicinity of the metal-oxide interface, Mater. Sci. Eng. A 742 (2019) 842–850. https://doi.org/10.1016/j.msea.2018.09.107.
[217] A. Baris, Increased hydrogen uptake of zirconium based claddings at high burnup, PhD thesis, University of Birmingham, 2019.
[218] J. Hawes, A. Baris, Y.-L. Chiu, S. Abolhassani, Characterization of the conductivity of metal-oxide interface of zirconium based fuel cladding at low and high burnups, J. Nucl. Mater. 534 (2020) 152133. https://doi.org/10.1016/j.jnucmat.2020.152133.
[219] T. Ungár, P. Frankel, G. Ribárik, C.P. Race, M. Preuss, Size-distribution of irradiation-induced dislocation-loops in materials used in the nuclear industry, J. Nucl. Mater. 550 (2021) 152945. https://doi.org/10.1016/j.jnucmat.2021.152945.
[220] T. Ungár, G. Ribárik, M. Topping, R.M.A. Jones, X.D. Xu, R. Hulse, A. Harte, G. Tichy, C.P. Race, P. Frankel, M. Preuss, Characterizing dislocation loops in irradiated polycrystalline Zr alloys by X-ray line profile analysis of powder diffraction patterns with satellites, J. Appl. Crystallogr. 54 (2021) 803–821. https://doi.org/10.1107/s1600576721002673.
[221] C. Janzon, PIE of two rods irradiated in Oskarshamn 3, one with cladding with enhanced Fe and one with standard LK3 cladding, Studsvik Report, 2016.
[222] C. Dai, L. Balogh, Z. Yao, M.R. Daymond, The habit plane of 〈a〉-type dislocation loops in α-zirconium: an atomistic study, Philos. Mag. 97 (2017) 944–956. https://doi.org/10.1080/14786435.2017.1287441.
[223] C. Dai, F. Long, P. Saidi, L.K. Béland, Z. Yao, M.R. Daymond, Primary damage production in the presence of extended defects and growth of vacancy-type dislocation loops in hcp zirconium, Phys. Rev. Mater. 3 (2019) 043602. https://doi.org/10.1103/PhysRevMaterials.3.043602.
[224] C. Dai, P. Saidi, Z. Yao, M.R. Daymond, Atomistic simulations of Ni segregation to irradiation induced dislocation loops in Zr-Ni alloys, Acta Mater. 140 (2017) 56–66. https://doi.org/10.1016/j.actamat.2017.08.016.
[225] F. Garzarolli, B. Cox, P. Rudling, Optimization of Zry-2 for High Burnups, ASTM STP 1529 (2011) 711–728. https://doi.org/10.1520/JAI102955.
[226] D.W. Saxey, Correlated ion analysis and the interpretation of atom probe mass spectra, Ultramicroscopy 111 (2011) 473–479. https://doi.org/10.1016/j.ultramic.2010.11.021.
[227] Y. Chang, W. Lu, J. Guénolé, L.T. Stephenson, A. Szczpaniak, P. Kontis, A.K. Ackerman, F.F. Dear, I. Mouton, X. Zhong, S. Zhang, D. Dye, C.H. Liebscher, D. Ponge, S. Korte-Kerzel, D. Raabe, B. Gault, Ti and its alloys as examples of cryogenic focused ion beam milling of environmentally-sensitive materials, Nat. Commun. 10 (2019) 942. https://doi.org/10.1038/s41467-019-08752-7.
[228] S.-M. Liu, I.J. Beyerlein, W.-Z. Han, Two-dimensional vacancy platelets as precursors for basal dislocation loops in hexagonal zirconium, Nat. Commun. 11 (2020) 5766. https://doi.org/10.1038/s41467-020-19629-5.